Doctoral Dissertation

博士論文

Structural and functional analysis of the light-gated cation channel, channelrhodopsin

(光駆動型カチオンチャネルであるチャネルロドプシンの構造機能解析)

A Dissertation Submitted for the Degree of Doctor of Philosophy

December 2020

令和 2 年 12 月博士　(理学)　申請

Department of Biological Sciences, Graduate School of Science,

The University of Tokyo

東京大学大学院理学系研究科

生物科学専攻

Kazumasa Oda

小田　和正

Abstract

Channelrhodopsins (ChRs) are microbial light-gated cation channels that function as sensory photoreceptors in green algae. ChRs are consist of seven transmembrane helices and a retinal chromophore covalently attached to a conserved lysine residue at TM7 via a Schiff base linkage. Light absorption causes retinal chromophore isomerization and subsequent protein conformational changes visualized as optically distinguished intermediates, coupled to channel opening and closing. When ChRs are expressed in neuron cells, their neural activity could be manually controlled by light illumination. This technique is called optogenetics and it is widely used in various fields such as neurology or medical science. However, there are some problems in using ChRs as an optogenetic tool. Currently available ChRs absorption peak is around 450 – 550 nm and such blue-green wavelengths have limited penetration depths into biological tissue. Therefore, a red-light activated ChR is urged. In such a situation, ChR from *Chlamydomonas noctigama* (Chrimson) was identified as the variant with the most red-shifted absorption peak at 590 nm and Chrimson represents one of the most promising ChRs as an optogenetics tool.

While many applied studies of ChRs have been performed, some basic molecular mechanisms of ChRs are still not fully understood. To understand the molecular mechanisms, structural information of ChR is extremely important, but the only two kinds of ChR structures, ChR chimera C1C2 and *Cr*ChR2, have been reported. This structural information provided an ion selectivity filter or cation-conducting pathway, but there remain some important questions. Especially, (1) the main factor controlling the absorption wavelength of ChRs (2) the detailed molecular events underlying channel gating after light illumination is quite important questions.

In this thesis, I report the crystal structure and functional analysis of Chrimson. The structure revealed that Chrimson resembles prokaryotic proton pumps in the retinal binding pocket while sharing similarity with other channelrhodopsins in the ion-conducting pore. Concomitant mutation analysis identified the structural features that are responsible for Chrimson's red light sensitivity; namely, the protonation of the counterion for the retinal Schiff base, and the polar residue distribution and rigidity of the retinal binding pocket. Based on these mechanistic insights, I engineered ChrimsonSA, a mutant with a maximum activation wavelength red-shifted beyond 605 nm and accelerated closing kinetics.

I also report the conformational changes of ChR following light illumination revealed by time-resolved serial-femtosecond crystallographic analyses. The isomerized

retinal adopts a twisted conformation and shifts toward the putative internal proton donor residues, consequently inducing the outward shift of TM3, as well as local deformation in TM7. These early conformational changes in the pore-forming helices should be the triggers that lead to the ion pore opening.

Contents

Table of amino acid abbreviations

1 letter	3 letter	Full name	1 letter	3 letter	Full name
A	Ala	Alanine	M	Met	Methionine
C	Cys	Cyctein	N	Asn	Aspargine
D	Asp	Aspartic acid	P	Pro	Proline
E	Glu	Glutamic acid	Q	Gln	Glutamine
F	Phe	Phenylalanine	R	Arg	Arginine
G	Gly	Glycine	S	Ser	Serine
H	His	Histidine	T	Thr	Threonine
I	Ile	Isoleusine	V	Val	Valine
K	Lys	Lysine	W	Trp	Tryptophan
L	Leu	leucine	Y	Tyr	Tyrosine

Chapter 1: General introduction

1-1 Rhodopsin family

1-1-1 Basic information of rhodopsin family

For most organisms, light is one of the most important stimuli and organisms use photoreceptor proteins to receive light. Photoreceptor proteins can bind a chromophore molecule, which can absorb a visible wavelength of light. One of the largest photoreceptor protein groups is the rhodopsin superfamily which employees a retinal as a chromophore molecule[1,2]. Therefore, rhodopsin protein is also called a retinal protein. Retinal is a vitamin A aldehyde and it absorbs near UV light (380 nm)[3]. When a retinal is bound to a rhodopsin protein region (called an "opsin"), absorption red-shift (400 ~ 600 nm) of retinal happens caused by an interaction between retinal and opsin. This opsin-induced absorption red-shift is called "opsin-shift" and rhodopsin can absorb a wide visible wavelength range of light[4] (Fig. 1-1). The visible light absorption of rhodopsin induces isomerization of retinal, which triggers sequential conformational changes of protein and rhodopsins function as photo-sensing or ion transport proteins[1,5,6].

1-1-2 Rhodopsin family classification

Generally, rhodopsins are categorized into two types, namely microbial rhodopsins (type-I) and animal rhodopsins (type-II)[7]. Microbial rhodopsins are widely distributed through all three biological kingdoms, bacteria, archaea, and eukarya[8], and they function as ion transporters or photosensors[9,10]. On the other hand, animal rhodopsins are only distributed in animals and they function as G-protein-coupled receptors (GPCRs)[11] (Fig. 1-2). Recently, a new type of rhodopsin family is identified using functional metagenomics. It is termed heliorhodopsin and many studies have been performed to elucidate the function of heliorhodopsin[12,13].

1-2 Microbial rhodopsin

1-2-1 Basic information of microbial rhodopsin

In 1971, the first microbial rhodopsin was isolated from the archaeon *Halobacterium salinarum* and it was termed bacteriorhodopsin (BR or *Hs*BR) as a light-driven outward H^+ pump[14]. Because of the high stability and high expression level of protein, BR has been well studied as a model of both membrane proteins and light-activated molecules. After the discovery of BR, various microbial rhodopsins have been

identified and studied, such as an inward chloride pump halorhodopsin (HR)[15], an outward sodium pump (NaR)[16], light-gated cation channel (ChR)[17,18], and light-gated anion channel (ACR)[19].

1-2-2 Architecture of microbial rhodopsin protein

BR was also the first membrane protein and microbial rhodopsin protein that was found to consist of seven transmembrane helices by electron microscopy in 1975[20]. After that, many high-resolution crystal structures of microbial rhodopsin have been reported [21–27]. In spite of the various functional or low sequential identity, the structural information revealed that they share a common architecture within their primary and tertiary structures.

Rhodopsin proteins are consist of seven transmembrane α-helices with the N-terminus facing outside of the cell and C-terminus facing inside of the cell. All-*trans* retinal is covalently attached to the ε-amino group of a highly conserved lysine residue in the middle of TM7 and formes a protonated Schiff base linkage (Fig. 1-3). The retinal binding pocket is the most structurally conserved region in microbial rhodopsins[1]. As the Schiff base is usually protonated[28], it requires negative charges for electrostatic stabilization. These amino acid residues or negative ions around the retinal Schiff base are termed "counter-ion"[29] and they are strongly conserved around microbial rhodopsins (Fig. 1-4). Upon illumination, all-*trans* retinal isomerizes to 13-*cis* and the protonation of retinal Shiff base is changed, initiating the biological functions such as signaling or transport activity of rhodopsins[2].

1-2-3 Photochemical reaction of microbial rhodopsin

In microbial rhodopsin, the isomerization of retinal from all-*trans* form to 13-*cis* form triggers a cyclic photochemical reaction and it is called "photocycle"[1,9,30]. Figure 1-5 shows the simple photocycle of BR. In the initial state, the retinal is all-*trans* state and BR absorbs around 580 nm wavelength light. Upon light illumination, the retinal isomerizes to 13-*cis,* followed by red shift of absorption maximum. This red shift of absorption maximum is caused by the change of retinal isomeric configuration. In the next step, the retinal Schiff base protonation state is changed and the absorption blue shift of absorption maximum is caused. When the protonation state of the retinal Schiff base is changed, the proton is transferred to counter-ions[1,9,31] and rhodopsin shifts its absorption peak. In parallel, the stored energy of the excited retinal induces conformational changes of protein from inward-facing to outward-facing. Then, the proton located on the counter-ion is released to the extracellular side and it triggers the

absorption red-shift. This photo intermediate serves as the last step in resetting the initial state.

1-3 Channelrhodopsin

1-3-1 Function of channelrhodopsin

As an ion channel of microbial rhodopsin, two light-gated cation channels were firstly identified from the eukaryotic green algae in 2002 and 2003 and named Channelrhodopsin-1 (ChR1) and Channelrhodopsin-2 (ChR2)[17,18]. In these algae, ChRs are located at the surface of a specialized cellular compartment called an "eyespot", and serve as a sensory photoreceptors[32]. Upon light illumination, ChRs allow fast proton and cation flux across cell membranes, resulting in plasma membrane depolatization[33].

1-3-2 Optogenetics

After the identification of ChRs, it was confirmed that ChRs show light-triggered large passive cation conductance and cell membrane depolarization in HEK293 and BHK cells[34,35]. Therefore, when ChRs are expressed in neural cells, their neural activity can be controlled by light illuminaiton[36,37]. This technique is called optogenetics[36,38,39] and it is used to study the neural basis of behavioral responses in different organisms such as *Caenorhabditis elegans*[40] or zebrafish[41]. The remarkable feature of optogenetics is high cell specificity[42] (Fig. 1-6). In general, electrical stimulation with extracellular electrodes cannot target specific classes of neurons in a heterogeneously populated tissue. In contrast, the stimulation induced by light illumination can target specific classes of neurons in heterogeneously populated tissue because it is possible to selectively target and express a microbial opsin gene with high specificity. As a famous example, optogenetics can control the sleep/wake behavior of adult mice through light-induced stimulation of hypocretin/orexin neurons in the hypothalamus[43]. As a result, optogenetics has been widely used in many research fields, such as neurology or medical science.

However, there are some problematic features of the optogenetics technique. *Cr*ChR2 is now used as a main tool of optogenetics and its absorption peak wavelength is around 480 nm. The transmission of such a short-wavelength light is low and it is hard to stimulate neural cells in the depth of tissues by external light illumination. To illuminate such cells, optical fiber insertion is used[43], but the invasiveness of inserting optical fiber is a problematic feature. Therefore, red-shifted ChR variants are particularly required, as longer-wavelength light allows deeper tissue penetration (Fig. 1-7).

1-3-3 Photocycle of channelrhodopsin

While many applied studies of ChRs have been performed, the basic molecular mechanisms of ChRs also have been revealed. Since the identification of ChR, many studies about the photocycle of ChRs have been reported[44–47] but the precise model has been still under consideration. In this section, a single non branched photocycle model of ChR2 is featured to explain the results of spectroscopic studies about ChR photocycle (Fig. 1-8). After blue-light excitation (λ = 470 nm), retinal isomerizes from all-*trans* to 13-*cis*, resulting in the red-shifted photo intermediate (λ= 500 – 520 nm, P_1^{520}). Then, proton transfer from protonated retinal Schiff base leads to blue-shifted photo intermediate (λ = 390 nm, P_2^{390}). After the reprotonation of retinal Schiff base, P_2^{390} transforms to red-shifted photo intermediate (λ = 500 – 520 nm, P_3^{520}). Considering the results of electrophysiological experiments, it has been suggested that the channel opening coincides with the P_2^{390} forming. After the P_2^{390} formation, it has also been suggested that the channel fully opens at P_3^{520} and starts closing at the end of P3. Finally, a nonconducting photo intermediate (λ = 480, P_4^{480}) appears after channel closing, and return to the dark state.

1-3-4 Structural feature of channelrhodopsin

To understand the molecular mechanisms of ChRs, structural information would be highly beneficial. However, ChR structures had not been reported immediately after the identification of ChR. It was because eukaryotic membrane proteins, including ChRs, are more difficult to express, purify or crystallize, as compared to water-soluble proteins or prokaryotic membrane proteins. Eukaryotic membrane proteins are generally unstabilized proteins and tend to aggregate or dissociate in the presence of detergents commonly used for previous structural studies. However, recent improvements of biochemical or biophysical strategies including expression systems or purification materials have successfully increased the number of reports for eukaryotic membrane protein structure[48–50]. Against this background, the first structural insights into ChRs were provided by the crystal structure of a ChR chimera, C1C2 (TM1–5 from Chlamydomonas reinhardtii ChR1 (*Cr*ChR1) and TM6–7 from *Cr*ChR2) in 2012[51]. C1C2 structure revealed a dimeric protein architecture with the putative ion permeation pathway located in each protomer and the ion-selectivity filter consisted of negatively charged amino acid residues located at the extracellular region of the transmembrane domain. In 2018, the structure of *Cr*ChR2 was also reported and provided further structural information about the ChR family[52].

1-4 Figures associated with Chapter 1

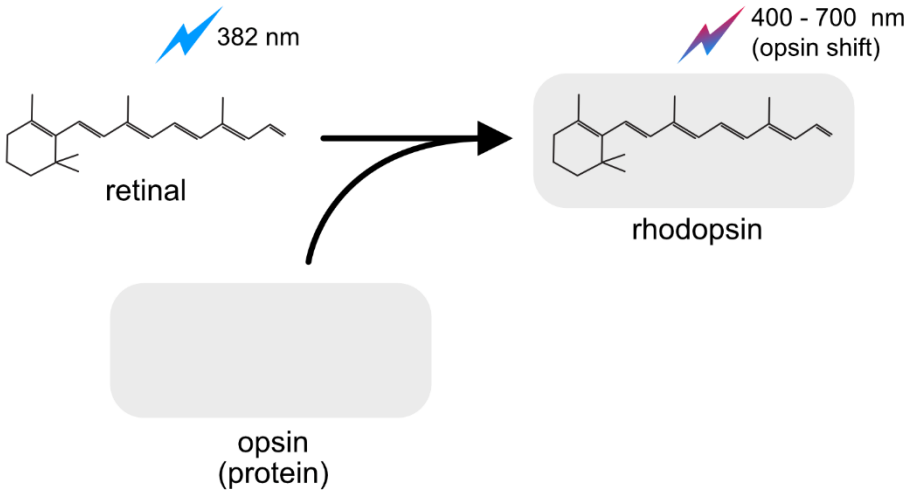

Fig. 1-1 Rhodopsin protein

Rhodopsin proteins are one of the largest photoreceptor proteins that consist of opsin and retinal as a chromophore. When a retinal is bound to opsin, it caused absorbance red-shift and rhodopsin can absorb visible light at various wavelengths.

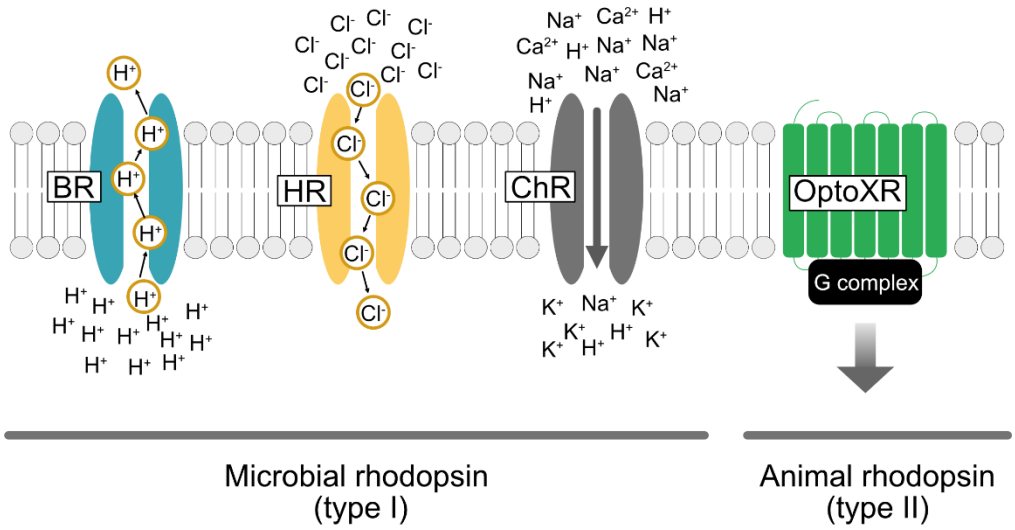

Fig. 1-2 Rhodopsin family classification

Rhodopsin family are classified into two types, microbial rhodopsins (type-I) and animal rhodopsins (type-II). While microbial rhodopsins function as an ion transporter, ion channel, or photosensor, animal rhodopsins function as a G-protein coupled receptor[53].

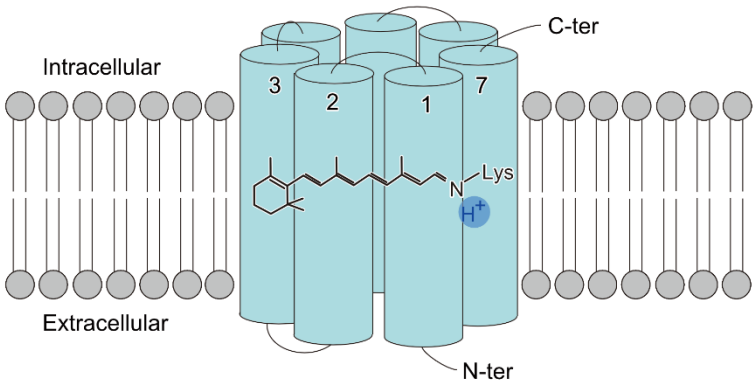

Fig. 1-3 Architecture of microbial rhodopsin protein

Microbial rhodopsins are consist of seven transmembrane proteins and all-*trans* retinal is covalently attached to the strongly conserved lysine residue in the middle of TM7.

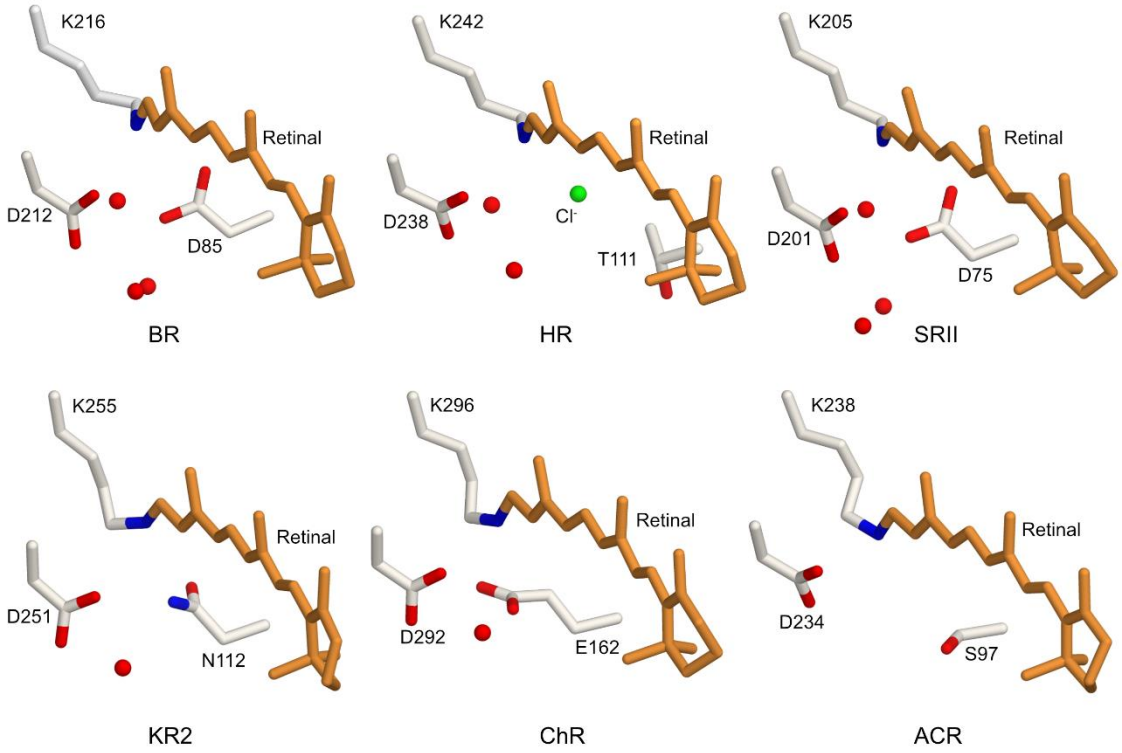

Fig. 1-4 X-ray crystallographic structures of the RSB region for six representative microbial rhodopsins

BR functions as a proton pump and HR functions as a chloride pump. SRII is a phototaxis sensor but pumps protons in the absence of its transmembrane transducer. KR2 functions as a sodium pump, ChR functions as a cation channel, and ACR functions as an anion channel.

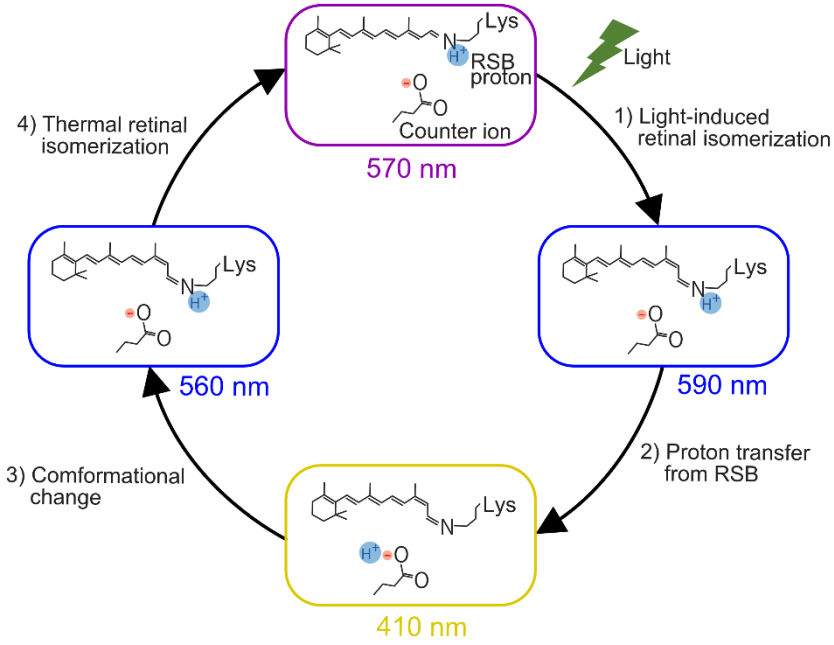

Fig. 1-5 Typical photocycle of microbial rhodopsin

After the light illumination, all-*trans* retinal isomerizes to 13-*cis* retinal, and the protonation state of retinal Schiff base changes. The interaction around the retinal effects on the rhodopsin absorption wavelength.

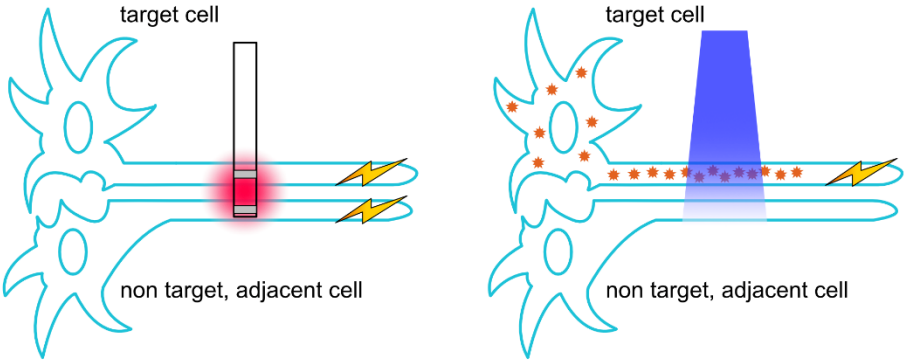

Fig. 1-6 Principle of optogenetics

In general, electrical stimulation with extracellular electrodes can not target specific classes of neurons in heterogeneously populated tissue. In contrast, the stimulation induced by light illumination can target specific classes of neurons in heterogeneously populated tissue.

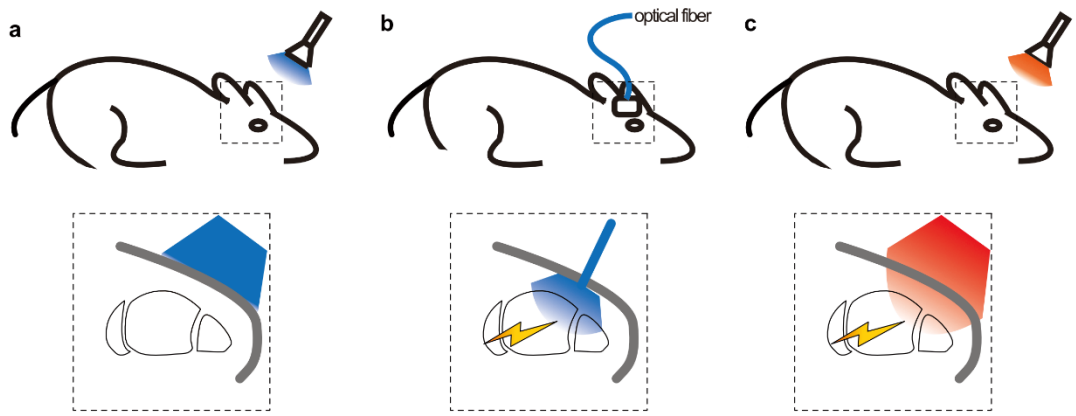

Fig. 1-7 Schematic model of *in vivo* optogenetics application

a, Short-wavelength light could not illuminate neural cells in the depth of organic cells because of the low light transmission. **b**, Through optical fiber, short-wavelength light can illuminate neural cells. **c**, As long-wavelength light allows deeper tissue penetration, neural cells could be illuminated without optical fiber.

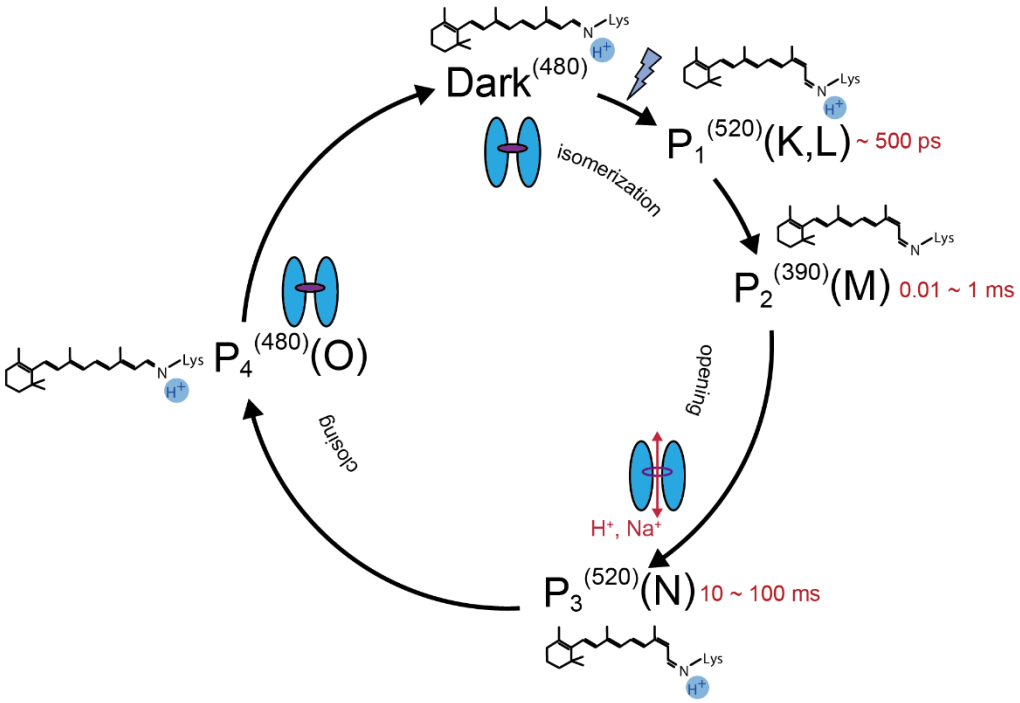

Fig. 1-8 Typical non-branched photocycle of channelrhodopsin

Schematic model of the ChR photocycle. Superscript of each reaction intermediate ($P_1^{(520)}$, $P_2^{(390)}$, $P_3^{(520)}$, $P_4^{(480)}$) indicates the wavelength of maximum absorption. Open/close states of the channel pore and the proposed model of the retinal and protonation of the Schiff

base are indicated. The time range in which the P_1-P_3 intermediates were observed in the spectroscopic studies in solution is shown.

Chapter2: Structural analysis of the red light-activated channelrhodopsin Chrimson

2-1 Introduction

2-1-1 Basic color-tuning mechanism of rhodopsin

A light illumination initiates functions of rhodopsins, and the absorption peak wavelength of rhodopsin determines the illuminated light color[1]. Therefore, what determines the illuminated light color, simply color-tuning, is an important question and several factors have been identified to be responsible for it[54,55]. Generally, the absorption peak depends on the length of the π-conjugated polyene chain in the retinal and the reciprocal of the energy level gap between the ground state and the excited state[1,55].

The most major factor affecting the absorption peak shift is the electrical interactions of retinal Schiff base proton with the counter-ion complex (Fig. 2-1 a). In the dark state, the retinal Schiff base is protonated and forms a stable interaction with counter ion(s) and this interaction contributes to lower the energy level of the ground state. Other factors are given by retinal-protein interactions (Fig. 2-1 b). One of them is the interaction between the retinal β-ion ring and amino acid residues around it. Upon light absorption, ultrafast charge translocation is caused in the retinal and the positive charge is displaced toward the retinal β-ion ring[56]. Thus, negatively charged amino acid residues around the β-ion ring stabilize the excited state energetically and lead to absorption red-shift. Besides, amino acid residues around the retinal could enforce the torsion of the retinal C-C bond and shrink the π-conjugated polyene chain, consequently produce absorption blue-shift[57] (Fig. 2-1 c).

2-1-2 Identification of color-tuned channelrhodopsin variants

Various naturally occurring ChRs have been identified thus far and show broad absorption peaks over the entire range of visible light[33,58,59]. In addition, many ChR variants designed by inducing mutation or creating chimera constructs have also been reported and show absorption peak shift. For example, a blue-shifted ChR that has non-polar residues around a retinal β-ion ring or a red-shifted activated ChR that consists of three kinds of ChRs were designed[60,61]. Moreover, molecular conformational design at atomic resolution based on the ChR structural information succeeded in creating a rational design of blue-shifted ChR[57]. In this study, two amino acid residues around the retinal β-ion ring were mutated and these mutated amino acids induced the retinal twist, following

the absorption blue-shift. Thus, structural information as well as sequence alignment is required for rational design.

2-1-3 Identification of most red-shifted channelrhodopsin, Chrimson

Given that the low transmission of visible light in organic tissue is one of the major obstacles in optogenetics, red-shifted ChR variants are particularly required, as longer-wavelength light allows deeper tissue penetration. *Volvox carteri* ChR1 (VChR1), with peak absorption at 530 nm, was the first identified[61], and several engineered VChR1 constructs, such as C1V1 and ReaChR, were further developed[60,62,63]. More recently, a ChR from Chlamydomonas noctigama (Chrimson) was identified as the variant with the most red-shifted absorption peak at 590 nm[59], which is more than 40 nm further red-shifted than all other ChRs. Chrimson allowed efficient red-light excitation beyond the operational range of native photoreceptors in adult flies and also enabled independent dual-color experiments in combination with blue-light-activated ChRs. Therefore, Chrimson represents one of the most promising ChRs for both basic neuroscientific research and medical applications. Meanwhile, the remaining blue-light sensitivity of Chrimson demands careful adjustment of light intensities to achieve purposeful combination with blue-light-activated tools, but the low sequence similarity to the structurally-resolved ChRs, such as C1C2 and *Cr*ChR2, has hampered further molecular engineering of Chrimson.

2-1-4 Study purpose

To understand the molecular mechanism of ChR absorption red-shift, the structural comparison of ChRs that have different absorption peak has long been required. In this study, the crystal structure of Chrimson was determined. Through the comparison with the C1C2 structure, the Chrimson structure reveals (i) the presence of an outer gate occluding the retinal Schiff base from the extracellular solvent, (ii) the unique protonation state of the counterion residue destabilizing the protonated retinal Schiff base in the ground state, (iii) highly biased polar residue distribution toward the β-ionone ring, and (iv) tight association with the retinal chromophore to improve the retinal planarity, which appears essential for fast photocycle kinetics.

2-2 Materials and methods for structural analysis of Chrimson

2-2-1 Plasmid construction and expression check

The wild-type Chrimson (wtChrimson) from *Chlamydomonas noctigama* was

cloned into a modified pFastBac expression vector (Invitrogen), which includes a C-terminal FLAG tag, a GFP-tag and a tobacco etch virus (TEV) protease cleavage site. The modified wtChrimson construct was expressed in Sf9 cells, using the Bac-to-Bac baculovirus expression system (Invitrogen). The expression check of wtChrimson constructs was performed by fluorescence-detection size-exclusion chromatography (FSEC). The result of FSEC indicated that the expression level and the stability of wtChrimson is very low. Therefore, two Chrimson variants were tested in which the extracellular N-terminal sequence (1-76) was replaced by either the corresponding sequence of the *Chloromonas subdivisa* channelrhodopsin (CsChrimson) or the N-terminal sequence (1-76) of *Cr*ChR1 (C1Chrimson) (Fig. 2-2, 2-3).

These constructs showed improved expression and excellent stability in detergent and the photocurrent properties of these constructs were also checked to investigate the effect of N-terminus replacing. Based on the results, it was shown that the photocurrent properties of Chrimson were minimally affected by the different N-terminus, and red light activation, high proton selectivity, and fast pH-dependent photocurrent kinetics were preserved in all constructs (Fig. 2-4). The plasmid construction and expression check was performed by Satomi Oishi. The photocurrent and channel kinetics were measured by Johannes Vierock.

2-2-2 Expression and Purification

Baculovirus-infected Sf9 cells were cultured in Sf900II (Invitrogen) at 27 °C for 24 h, and 50 mM all-*trans* retinal (SIGMA-ALDRICH) was added after 24 h post-infection at the final concentration of 20 μM. Cells were harvested 48 h after infection by centrifugation at 6000× g for 10 min. The pellets were disrupted by sonication and resuspended in a buffer containing 150 mM NaCl, 50 mM HEPES, pH 7.0, 5% glycerol, and 0.1 mM phenylmethylsulfonyl fluoride (PMSF). The cell debris was cleared by centrifugation at 10,000× g for 30 min, and the crude membrane fraction was collected by ultracentrifugation (Ti45 rotor, 215,000× g, 1 h). This fraction was solubilized in buffer containing 150 mM NaCl, 50 mM HEPES, pH 7.0, 5% glycerol, 0.1 mM PMSF, 2.5% n-dodecyl-β-D-maltoside (DDM), and 0.5% cholesteryl hemisuccinate (CHS). The insoluble material was removed by ultracentrifugation (Ti70 rotor, 208,000× g, 30 min), and the supernatant was mixed with ANTI-FLAG M2 Agarose Affinity Gel(SIGMA-ALDRICH). After binding for 1.5 h, the flow-through was discarded. Following the cleavage of EGFP–FLAG by TEV protease (homemade), the flow-through containing Chrimson was collected, concentrated, and further purified by size-exclusion chromatography in 150 mM NaCl, 50 mM HEPES, pH 7.0, 5% glycerol, 0.05% DDM,

and 0.01% CHS. Peak fractions were pooled and concentrated to 7.0 mg/ml for crystallization.

2-2-3 Crystallization

The purified CsChrimson or C1Chrimson protein was mixed with monoolein (SIGMA- ALDRICH) in a 2:3 protein to lipid ratio (w/w), forming a lipidic cubic phase (LCP). Aliquots (50 nl) of the protein-LCP mixture were spotted on a 96-well sitting-drop plate and overlaid with 800 µl of a precipitant solution by the crystallization robot, Crystal Gryphon (Art Robbins Instruments). The purified CsChrimson protein yielded only poorly diffracting crystals with low reproducibility, but C1Chrimson yielded well-diffracted crystals with high reproducibility. Crystals were obtained in 28–33% (w/v) PEG500DME, 100 mM Na citrate, pH 5.0, 100 mM Na malonate, pH 7.0, and 10 – 40 mM sarcosine. All crystals were incubated for 4 weeks in the dark. The crystals were harvested using micromounts (MiTeGen) and flash-cooled in liquid nitrogen without any additional cryoprotectant.

2-2-4 Structural determination

X-ray diffraction datasets were collected at the SPring-8 BL32XU beamline. Data processing and merging of multiple crystals were performed using the program KAMO (https://github.com/keitaroyam/yamtbx/blob/master/doc/kamo-en.md)[64]. Each dataset was indexed and integrated using XDS[65]. Since the crystals were anisotropic, with varied lattice parameters, datasets with a c-axis less than 173 Å and a b-axis less than 82 Å were selected. Finally, a group of outlier-rejected datasets was scaled and merged using XSCALE. The structure was solved by the molecular replacement method implemented in Phenix Phaser-MR[66], using the model of C1C2 (PDB: 3UG9). The structure was manually modified to fit into the electron density maps, using the program Coot[67], and then refined with the programs Phenix[66] and Refmac5 in the CCP4 suite[68]. Figures were prepared with Cuemol (http://www.cuemol.org). Protein internal cavities are analyzed by the program hollow[69].

2-3 Materials and methods for functional analysis of Chrimson

2-3-1 Ultraviolet/visible spectroscopy

C1Chrimson was fused with the C-terminal FLAG-tag sequence, and expression and purification were performed as described above. The peak fraction of the size-exclusion chromatography was collected and concentrated for the measurement. The pH

was adjusted by the addition of 20 µl 1M buffer (pH5:Na-acetate, pH6:Na-citrate, pH7:HEPES-NaOH, pH8:Tricine- NaOH, pH9:Tris-HCl) to 100 µl of the protein solution. Ultraviolet/visible absorption spectra were recorded with an Ultrospec 3300 Pro ultraviolet/visible spectrophotometer (Amersham Biosciences), using 1-cm quartz cuvettes.

2-3-2 HEK-cell electrophysiology

These experiments were performed by Johannes Vierock. The coding sequences of Chrimson (KF992060.1), CsChrimson (KJ995863.2), and C1Chrimson were cloned into the pmCerulean-C1 vector (using the NheI and AgeI restriction sites for Chrimson and CsChrimson or the Nhe1 and Kpn2I restriction sites for C1Chrimson) and expressed under the control of the CMV-promotor. Site-directed mutagenesis was performed using a QuickChange Site-Directed Mutagenesis Kit (Agilent Technologies, Santa Clara, CA), according to the manufacturer's instructions. As the Chrimson photocurrents were nearly unaffected by the targeting strategy (Fig. 2-3), CsChrimson was employed as the backbone for the electrophysiological mutant analysis.

HEK cell preparation and whole-cell patch-clamp experiments were performed as previously described[70,71]. HEK293 (human embryonic kidney) cells (85120602, Sigma-Aldrich) were cultured in Dulbecco's Modified Medium (DMEM) with stable glutamine (Biochrom, Berlin, Germany) supplemented with 10% (v/v) fetal bovine serum (FBS Superior; Biochrom, Berlin, Germany), 1 µM all-*trans* retinal and 100 µg/ml penicillin/streptomycin (Biochrom, Berlin, Germany). The cells were seeded on coverslips at a concentration of 0.75×10^5 cells/ml and transiently transfected using the FuGENE® HD Transfection Reagent (Promega, Madison, WI) 28–48 h before measurement.

Patch pipettes were prepared from borosilicate glass capillaries (G150F-3; Warner Instruments, Hamden, CT) using a P-1000 micropipette puller (Sutter Instruments, Novato, CA) and were subsequently fire polished. The pipette resistance was between 1.8 and 3.0MΩ. Single fluorescent cells were identified using an Axiovert 100 inverted microscope (Carl Zeiss, Jena, Germany). Monochromatic light (±7 nm) was provided by a Polychrome V monochromator (TILL Photonics, Planegg, Germany), attenuated by a motorized neutral density filter wheel (Newport, Irvine, CA) for equal photon fluxes at different excitation wavelengths, and temporally controlled by a VS25 and VCM-D1 shutter system (Vincent Associates, Rochester, NY). Recorded signals were filtered at 2 kHz using an AxoPatch 200B amplifier (Molecular Devices, Sunnyvale, CA) and digitized using a DigiData 1440 A digitizer (Molecular Devices, Sunnyvale, CA) at a

sampling rate of 5–10 kHz. The reference bath electrode was connected to the bath solution via a 140 mM NaCl agar bridge. The extracellular buffer exchange was performed manually by adding at least 5ml of the respective buffer to the recording chamber (500 µl chamber volume) while a Ringer Bath Handler MPCU (Lorenz Messgerätebau, Katlenburg-Lindau, Germany) maintained a constant bath level. Standard bath solutions contained 110 mM NaCl, 1 mM KCl, 1 mM CsCl, 2 mM $CaCl_2$, 2 mM $MgCl_2$, and 10 mM HEPES at pH_e 7.2 (with glucose added up to 310 mOsm). Standard pipette solution contained 110 mM NaCl, 1 mM KCl, 1 mM CsCl, 2 mM $CaCl_2$, 2 mM $MgCl_2$, 10 mM EGTA, and 10 mM HEPES at pH_i 7.2 (glucose added up to 290 mOsm). For ion selectivity measurements, NaCl was replaced by either 110mM GuanidiniumCl or 110 mM NMDGCl with 1 mM NaCl remaining, and HEPES was substituted with citric acid or TRIS for pH 5 or pH 9 respectively. For the measurement of ultra slow closing kinetics (empty columns Fig. 5f) cells were clamped at 0mV and channel conductance was probed by short 20 ms voltage pulses to −60 mV at the slow frequency of 0.2 or 0.5 Hz (for M201T or M201N, respectively) in order to reduce kinetic artifacts imposed by intracellular acidification due to continuous proton influx as previously reported[70]. The light intensities were measured after passing through all of the optics using a P9710 optometer (Gigahertz-Optik, Türkenfeld, Germany) and normalized to the water Plan-Apochromat 40 × /1.0 differential interference contrast (DIC) objective illuminated field (0.066 mm^2). The maximum light intensity was 2.28 $mW \times mm^{-2}$ at 580 nm and 2.47 $mW \times mm^{-2}$ at 530 nm. All electrical recordings were controlled by the pCLAMP™ software (Molecular Devices, Sunnyvale, CA). The whole-cell recordings had a minimum membrane resistance of 500 MΩ (usual > 1 GΩ) and an access resistance below 10 MΩ.

Electrical recordings were analyzed using the Clampfit 10.7 software (Molecular Devices, Sunnyvale, CA), Microsoft Excel and Origin 2017® (OriginLab, Northampton, MA). Photocurrent traces were baseline corrected, filtered, and reduced in size for display purposes. Photocurrents were normalized to peak photocurrents at −60 mV under standard conditions of symmetric 110mM NaCl $pH_{e/i}$ 7.2. Action spectra were fitted using a parametric Weibull function (y = y0 + A*((w2–1)/w2)^((1-w2)/w2)*S^(w2–1)*exp(-s^w2 + (w2–1)/w2) with S = (x-xc)/ w1 + ((w2–1)/w2)^(1/w2) and the estimated parameters A, y0, w1, w2, and xc). The photocurrent kinetics were estimated by biexponential fits and simplified by an apparent time constant (τapparent) calculated as (A1*τ1 + A2*τ2)/(A1 + A2). The exact number of biological replicates for each measurement is provided in the figure legend. To compare the data, two-sample t-tests were performed with Welch's correction in Origin 2017®. The significance thresholds

were set at $p < 0.05$ (*), $p < 0.01$ (**), $p < 0.001$ (***), and $p < 0.0001$ (****).

2-3-3 Neuronal recordings in hippocampal slice cultures

These experiments were performed by Silvia Rodriguez-Rozada. Chrimson wild type and the ChrimsonSA mutant were subcloned into neuron-specific expression vectors (pAAV backbone, human synapsin promoter). Organotypic slice cultures of rat hippocampus were prepared as described[72] and transfected by single-cell electroporation[73] after 14 days in vitro (DIV). Animal procedures were in accordance with the guidelines of local authorities and Directive 2010/63/EU. Plasmids were each diluted to 1 ng/µl in K-gluconate–based solution consisting of (in mM): 135 K-gluconate, 4 $MgCl_2$, 4 Na_2-ATP, 0.4 Na-GTP, 10 Na_2-phosphocreatine, 3 ascorbate, 0.02 Alexa Fluor 594, and 10 HEPES (pH 7.2). An Axoporator 800 A (Molecular Devices) was used to deliver 50 hyperpolarizing pulses (−12 mV, 0.5 ms) at 50 Hz. At DIV 18–20, targeted patch-clamp recordings of transfected neurons were performed under visual guidance using a BX-51WI microscope (Olympus, Hamburg, Germany) equipped with Dodt-gradient contrast and a Double IPA integrated patch amplifier controlled with SutterPatch software (Sutter Instrument, Novato, CA, USA). Patch pipettes with a tip resistance of 3–4MΩ were filled with (in mM): 135 K-gluconate, 4 $MgCl_2$, 4 Na_2-ATP, 0.4 Na-GTP, 10 Na_2-phosphocreatine, 3 ascorbate, 0.2 EGTA, and 10 HEPES (pH 7.2). Artificial cerebrospinal fluid (ACSF) consisted of (in mM): 135 NaCl, 2.5 KCl, 2 CaCl2, 1 MgCl2, 10 Na-HEPES, 12.5 D-glucose, 1.25 NaH2PO4 (pH 7.4). Synaptic currents were blocked with 10 µM CPPene, 10 µM NBQX, and 100 µM picrotoxin (Tocris, Bristol, UK). Measurements were not liquid junction potential (LJP) corrected. The LJP was -15.5 mV. A 16-channel pE-4000 LED light engine (CoolLED, Andover, UK) was used for epifluorescence excitation and delivery of light pulses (ranging from 365 to 660 nm). Light intensity was measured in the object plane with a 1918-R power meter equipped with a calibrated 818-ST2-UV/D detector (Newport, Irvine CA) and divided by the illuminated field (0.134mm^2) of the LUMPLFLN 60XW objective (Olympus).

2-3-4 Two-photon microscopy

These experiments were performed by Johannes Vierock and J. Simon Wiegert. The custom-built two-photon imaging setup was based on an Olympus BX-51WI upright microscope upgraded with a multiphoton imaging package (DF-Scope, Sutter Instrument, Novato, CA, USA and Rapp OptoElectronic, Wedel, Germany), and controlled by ScanImage (Vidrio Technologies, Ashburn, VA, USA). Fluorescence was detected through the objective (LUMPLFLN 60XW, Olympus, Hamburg, Germany) and the oil-

immersion condenser (1.4 NA) using GaAsP-PMTs (Hamamatsu Photonics, Hamamatsu, Japan). A tuneable Ti:Sapphire laser (Chameleon Vision-S, Coherent, Dieburg, Germany) was set to 810 nm to excite cerulean.

2-4 Results and discussion

2-4-1 overall structure of the C1Chrimson

C1Chrimson crystals that diffracted X-rays to the maximum resolution of 2.6 Å and the structure was determined by molecular replacement, using the C1C2 structure as the template (PDB: 3UG9) (Fig. 2-5 **a**). Although Chrimson is distantly related to the CrChRs (about 50% sequence identity over the transmembrane region), the overall structure of Chrimson superimposes well with those of C1C2 (Fig.2-5 **b**) (RMSD 1.11 Å). The two protomers in the asymmetric unit form a dimer, with each protomer composed of the extracellular N-terminal domain, 7TM helix bundle and the C-terminal β-hairpin loop region. The CrChR1-derived N-terminal residues mediate the crystal packing contacts between the layers in the lipidic cubic phase crystal and facilitate the dimeric interaction by forming the inter-protomeric β-sheet and three disulfide bonds (Fig. 2-6). While the outer membranous regions are partially disordered, the TM region is clearly visible in the electron density map, including the covalently attached all-trans retinal (Fig. 2-7). The structures of the two protomers (mol A and B) are essentially the same (RMSD = 0.66) (Fig. 2-6 c), but due to their different crystal packing contacts, mol A presents better electron density. Therefore, our discussion below is based on the mol A structure of Chrimson. In direct superposition of Chrimson with C1C2 and CrChR2, the author observed slight differences in the helix orientations, especially at TM2 and TM7, which deviate by about 2 Å on the extracellular side and 2.5 Å on the intracellular side, respectively (Fig. 2-5 b). As these helices are directly involved in the ion pore formation in ChRs, by mediating conformational changes during the photocycle[74], these variations might be partly responsible for the differences in ion permeation of Chrimson and CrChRs[70].

In Chrimson, the putative ion pathway, formed by TM2, 3, 6, and 7, is lined by five highly conserved negatively charged residues, Glu124 (E1), Glu125 (E2), Glu132 (E3), Glu139 (E4), and Glu143 (E5) (residue numbering is according to wild-type Chrimson[59]) (Fig. 2-8 a). In the current ground state structure of Chrimson, the ion-conducting pore is closed by three constriction sites that restrict ion permeation, on the intracellular side (inner gate), at the middle of the membrane (central gate), and on the extracellular side (outer gate) (Fig. 2-8 a). While the inner and central gates are also

observed in C1C2 and CrChR2[51,75], their constituents differ in several aspects (Fig. 2-8 and Fig. 2-9). The inner gates of C1C2 and CrChR2 are mainly formed by ionic interactions between the acidic residues (E1 and E2) and the basic residues (His173 and Arg307 in C1C2 and His134 and Arg268 in CrChR2) (Fig. 2b upper panels). In Chrimson, this histidine is substituted with lysine (Lys176), and both Glu124 (E1) and Glu125 (E2) are oriented toward the cytoplasmic solvent, with only E2 providing an ionic interaction with Arg310. The central gate is located adjacent to the retinal Schiff base (Fig. 2b middle panels), where three hydrophilic residues (Ser102, Glu129 (E3) and Asn297 in C1C2, and Ser63, Glu90 (E3) and Asn258 in CrChR2) occupy the pore and thereby hinder ion permeation. In Chrimson, two of the three residues are substituted, resulting in a rather loose packing. In addition, Ala105 (serine in C1C2 and CrChR2) is no longer involved in the gate formation, and instead, Glu300 forms a hydrogen bond with the backbone carbonyl of Ala101, which is one helical turn below the involved residues in C1C2 and CrChR2. Finally, the author observed remarkable structural diversity at the extracellular end of the ion-conducting pathway among all three ChR structures. In Chrimson, direct hydrogen bonding between Glu139, Tyr159, and Ser288 interconnects TM2, TM3, and TM7 and constitutes the outer gate constriction (Fig. 2-8). In contrast, C1C2 has an open tunnel that allows water access to the middle of the pathway, and CrChR2 has an extended water-filled cavity (EC2), which is interrupted at the extracellular end of TM2 by hydrogen bonds between Glu101, Gln117 and Thr246 (EG: Extracellular gate, Fig. 2-9). Mutations of the three pore-lining glutamates involved in the interhelical hydrogen bonds in Chrimson, namely, Glu125 (E2) in the inner gate, Glu300 in the central gate and Glu139 (E4) in the outer gate, caused dramatic decelerations in the photocurrent kinetics[70], whereas the homologous mutations of E2 and E4 in CrChR2 did not affect the channel kinetics[76]. Therefore, the observed variations in the gating interactions may account for the fast gating kinetics of Chrimson[70].

2-4-2 Unique counterion configuration in Chrimson

The electrostatic interaction between the protonated Schiff base (PSB) and the counterion is the major determinant for the absorption spectrum of the retinal chromophore[54,55,74]. In general, negative charges in close proximity to the PSB stabilize the ground state and lead to a higher energy gap between the ground and excited states, resulting in blue-shifted absorption, while neutralization or spatial separation of the counterion charge leads to a lower energy gap and red-shifted absorption. In C1C2, the positive charge of the PSB is stabilized by two anionic counterion residues, Ci1 and Ci2 (Glu162 and Asp292, respectively), which are highly conserved among ChRs, including

Chrimson (Glu165 and Asp295)[59,77] (Fig. 2-10). Recent studies have indicated that the highly red-shifted absorption of Chrimson is partly due to the protonation of the counterion residue Glu165[70,78], which weakens the stabilization effect for the PSB, thus causing red-shifted absorption similar to that of the acidic form of BR (BR_{605})[71]. Consistent with these studies, the purified Chrimson protein showed a large pH-dependent spectrum shift (Fig. 2-11). The crystals of Chrimson were obtained under low pH conditions (Methods), and the blue color of the crystals indicates that the current structure represents its red light-absorbing (protonated) state (Fig. 2-11 c, d). Regarding the two counterion residues, Glu165 is in 3.0 Å proximity to the PSB, while Asp295 is farther away, at 3.6 Å (Fig. 2-10 a). Glu165 resides just beside the PSB, a location corresponding to the hydrated water molecule in the bacteriorhodopsin (BR) dark state (Fig. 2-10 b), and the two counterion residues Glu165 and Asp295 are only 3.3 Å apart from each other (Fig. 2-10). Therefore, the Glu165 proton might be partly shared by both counterion residues, via hydrogen bond interactions. Most importantly, the counterion complex is shielded from the extracellular bulk solvent by the hydrophobic side chain of Phe135, which is essential to stabilize the protonated form of the carboxylate, as reported in the previous studies[70,78,79]. (Fig. 2-10 and 2-11). In contrast, in C1C2 and CrChR2, the phenylalanine is substituted with lysine (Lys132 in C1C2 and Lys93 in ChR2), and its positively charged side chain stabilizes the ionized (deprotonated) form of the Ci1 carboxylate (Glu162 in C1C2 and Glu123 in CrChR2) (Fig. 2-10 and 2-11).

2-4-3 Outer gate and ion pore of Chrimson

As the counterion configuration of Chrimson is essentially stabilized by the carboxylic acids of both Glu165 and Asp295, the mutation of either residue caused a blue-shift in the action and absorption peaks by 5–60 nm and abolished the pH dependence (Fig. 2-10 e, f and 2-12 c). This can be explained by the decreased pKa and consequent deprotonation of the remaining counterion residue (Asp295 for the Glu165 mutants and Glu165 for the Asp295 mutants), consistent with previous studies of Chrimson[70,78] and other channelrhodopsins[79]. The blue-shift was more prominent when Asp295 is mutated, whereas the mutation of Glu165 to Gln or Ala had a moderate effect. This is also consistent with the counterion configuration in the current structure. Since the PSB is closer to Glu165 than to Asp295, the neutralization of Asp295 should focus the negative charge exclusively on Glu165, which is much closer to the PSB, thus causing a larger blue-shift. Whereas blue-shift was equally pronounced for all Asp295 mutants, it varied largely for different mutants of Glu165 (Fig. 2-10 e, h and Fig. 2-12 d) as the introduced side chain might affect the position and pKa of the remaining counterion residue Asp295.

In addition to the counterion residues, mutations of the neighboring carboxylates, such as Glu132 (E3), Glu139 (E4), and Glu300, located within the extracellular cavity, also led to strong blue-shifts (Fig. 2-13 a, b and 2-14), although these residues are not in the proximity of the Schiff base. The effects of these mutants are more prominent, as compared to the counterion mutants (E165Q and D295N), although these mutants still retained the pH-dependency and showed small fractions of red-light sensitive components under the low pH conditions (Fig. 2-14 d–f). Therefore, the author concluded that both mutations predominantly affect the protonation of the counterion residues, via either the hydrogen-bonding network or long-range electrostatic interactions. In contrast, the mutation of Glu143, located outside the extracellular cavity, had minimal effects on the absorption spectrum and the pH-dependent shift ((Fig. 2-14 g). These results indicated that the cluster of carboxylate residues that are separated from the extracellular solvent by the outer gate might also contribute to the protonation of the counterion residues. Consistently, mutations that destabilize the outer gate hydrogen-bonding network, such as Tyr159 and Glu139 (E4), caused a largely blue-shifted activation spectrum[70]. Further investigation of the residues constituting the extracellular ion-conducting pathway was performed. At the exit of this pathway, Arg162 partly participates in the extracellular ion pore, together with Tyr159 and Phe135 (Fig. 2-13 a). Stabilized by a hydrogen bond with Asn287, Arg162 is slightly oriented toward the negatively charged residue Glu277, which is exposed to the solvent. The mutation of Arg162, as well as those of Asn287 and Glu277, caused a large blue-shift of the activation spectrum (Fig. 2-13 c), indicating that Arg162 electrically affects the PSB environment, and its precise arrangement is important for the protonation of Glu165. By analogy to its functional significance in other microbial rhodopsins[80], the author assumed that Arg162 is directly involved in channel opening and thus characterized its role in more detail. Whereas the R162A mutant is completely non-functional, as previously shown in C1C2 and CrChR2[51,81], mutations to positively charged residues preserved the channel function, although the mutants showed significantly reduced amplitudes and impaired kinetics (Fig. 2-12 and 2-13). Unexpectedly, a photocurrent analysis in HEK cells indicated that the ion-conducting pore of the R162H mutant is permeable to the large cation guanidinium, which is only poorly conducted by wild-type Chrimson (Fig. 2-13 e)[70]. Furthermore, the photocurrent amplitudes were significantly reduced by the N287E mutation, which may stabilize the Arg162 orientation in the current dark state structure, whereas the photocurrents were partly restored in pH 5, where this effect should be weakened (Fig. 2-13 d, g and 2-12 b and c). As previous studies have shown that two neighboring carboxylate residues, E4 (Glu139) and E5 (Glu143), located at the extracellular end of TM2, are responsible for

the proton selectivity in Chrimson[70], these results are in support of Arg162 being directly involved in the formation of the ion-conducting pore and possibly contributing to the ion-selective filter of Chrimson.

2-4-4 Retinal binding pocket

As described above, the outer gate and the consequential protonation of the counterion residues essentially contribute to the red-shifted absorption of Chrimson. However, even at high pH with a deprotonated counterion, Chrimson absorbs a longer wavelength (530 nm) than C1C2 (480 nm), implying an additional mechanism contributing to the large red-shifted absorption. Compared to C1C2, about half of the residues constituting the retinal binding pocket are substituted in Chrimson, and the structural comparison revealed that Chrimson resembles BR rather than C1C2, with respect to the residues surrounding the polyene chain and the β-ionone ring (Fig. 2-15 a–d). the author constructed Chrimson mutants with residues mutated to the corresponding residues of C1C2 and measured their action spectra (Fig. 2-15 e, f and 2-12). The spectra of M201T, S223G, Y231F, Y268F, and A298S were all blue-shifted by 10–30 nm as compared to the wild type, indicating that all five residues collectively contribute to the red-shifted activation of Chrimson. According to the general mechanism of color tuning in retinal proteins, negative polarity near the β-ionone ring stabilizes a light-excited intermediate that involves charge movement toward the β-ionone ring during retinal isomerization and thus leads to the red-shifted absorption, while negative polarity near the Schiff base leads to the blue-shifted absorption[55]. Consistently, polar residues such as Ser223 and Tyr231 are located near the β-ionone ring, while the non-polar residue Ala298 is located near the Schiff base (Fig. 2-15 a). All of these residues are conserved in other red-shifted variants such as VChR1 and ReaChR, but they are substituted with the non-polar residues Gly220 and Phe228, and the polar residue Ser295, respectively, in C1C2 (Fig. 2-15 b and 2-2). The contributions of these residues to the red-shifted absorption were further confirmed by measuring the absorption spectra of the above mutants (S223G, Y231F, and A298S) (Fig. 2-15 g), which though showed slightly larger blue-shifts as compared to the action spectra. Conversely, the introduction of these residues to C1C2 (G220S, F217Y, and S295A) caused a redshift of the absorption peak by about 10–30 nm (Fig. 2-15 h). These results show that the biased distribution of the polar residues throughout the retinal binding pocket contributes to the redshifted absorption of Chrimson and other red-shifted variants. Meanwhile, Tyr268 is the exception, as the non-polar substitution Y268F caused blue-shifted absorption by about 10 nm, although it is located near the Schiff base (Fig. 2-15 e). As Tyr268 is engaged in the hydrogen bond with the

counterion residue Asp295 (Figs. 2-10 a and 2-15 a), the mutation to phenylalanine probably allows Asp295 to approach toward the PSB and stabilizes its positive charge, thus causing the blue-shift.

Additional structural differences were found in TM4 and TM5, which flank the retinal binding pocket (Fig. 2-15 a–c right panels). Chrimson has several bulky residues on these helices. In particular, the bulky side chain of Met201 tightly packs against the polyene chain of retinal (Fig. 2-15 a). As previously shown for C1C2 and archaerhodopsin-3, the residue at this position is particularly important for the torsion angle at the C6 = C7 bond[57]. In agreement with this study, the mutation of Met201 to the smaller residue, threonine, caused a large blue-shift in the absorption peak by about 50–80 nm (Fig. 2-15 g and 2-14). In C1C2, the reverse mutation T198M caused a red-shifted absorption (Fig. 2-15 h). These observations suggest that tight packing against the polyene chain is important for the red-shifted absorption, probably by affecting the π-electron conjugation.

Remarkably, the M201T mutant further showed extremely slow-closing kinetics, and photocurrents were sustained for minutes (Fig. 2-15 f, i), indicating an additional important role of Met201 in channel gating kinetics. Also in bacteriorhodopsin, the alanine mutation of the corresponding methionine (Met118) or the adjacent methionine (Met145) leads to a slower photocycle and a consequent reduction in the proton pump activity, as well as a large blue-shift in the absorption[82,83]. These results indicate that the structural rigidity around the β-ionone ring is especially crucial for the proper photocycle process. Therefore, the slow kinetics of the M201T mutant is probably associated with the loose interaction at the retinal binding pocket, which decelerates conformational propagation from the isomerized retinal to the protein. The effect of the M201T mutation is reminiscent of the step function opsin (SFO) mutants of the CrChRs, in which the mutation of the DC-pair (Asp195 and Cys167 in C1C2 and Asp156 and Cys128 in CrChR2) caused extremely slow channel kinetics, by affecting proton exchange reaction at the Schiff base[84–86]. Although Met201 occupies a position close to the DCpair in CrChRs (Fig. 2-15 a and b), the Asp residue of DC-pair, which is the putative internal proton donor for the deprotonated Schiff base in CrChR2[87], is substituted with cysteine (C198), suggesting a completely different mechanism between the Chrimson M201T mutant and the *Cr*ChR SFO mutants. In Chrimson, mutation of the Cys128 homolog (C170A) had minimal impact on the photocurrent kinetics, and the reintroduction of the DC-pair (C198D) caused nearly complete loss of the photocurrent, albeit accelerated photocurrent kinetics (Fig. 2-15 f), further supporting a different gating mechanism of Chrimson compared to the previously proposed gating model for *Cr*ChRs. The

observation in Chrimson is more in agreement with the general importance of the retinal binding pocket stability for the overall photocycle[88], which is indeed different between Chrimson and *Cr*ChRs (Fig. 2-15 a, b). This notion is also consistent with the recent study showing that mutations near the β-ionone ring (TM6) affect the channel kinetics in Chrimson and other ChRs[89].

2-4-5 Rational design of a more red-shifted Chrimson

The current structure and concomitant extensive mutation analysis revealed three important factors underlying the large red-shift of Chrimson: the unique protonation state of the counterion residues, the highly biased distribution of the polar residues toward the β- ionone ring, and the structural rigidity of the retinal binding pocket. These notions allowed us to rationally design a more redshifted Chrimson variant. As two of the three factors, the electrostatic stabilization of the PSB and the tight association around the retinal pocket, are already highly optimized in Chrimson, the author engineered the polarity distribution around the retinal binding pocket and successfully obtained a red-shifted mutant by decreasing the polarity near the Schiff base (S169A) (Fig. 2-15 a). The absorption and action spectra peaks of this mutant are at 608 nm and 605 nm, respectively, which are red-shifted by about 20 nm as compared to wild-type Chrimson (Fig. 2-16 a, b and 2-17 a and b). Surprisingly, this mutant displayed 10-fold accelerated channel closing kinetics, as compared to wild-type Chrimson (Fig. 2-16 c), which is comparable to the recently reported engineered Chrimson variants with fast closing kinetics (f-Chrimson and vf-Chrimson)[89]. Due to the red-shift and the accelerated closing kinetics, the author named this new mutant ChrimsonSA (S169A, Super red-shifted and Accelerated). To validate its usefulness for optogenetic applications, ChrimsonSA was tested in hippocampal neurons (Fig. 2-16 e–l). Although the photocurrent density of the S169A mutant was reduced in HEK cells, as compared to wild-type Chrimson (12 ± 4 pA/pF for S169A versus 90 ± 60 pA/pF for WT) (Fig. 2-12), its photocurrent size is comparable to the *Cr*ChR2 stationary currents measured in HEK cells under the same conditions (15 ± 7 pA/pF)[70]. In neurons, photocurrents of ChrimsonSA were smaller than WT Chrimson but sufficient to trigger action potential firing with 635 nm light at intensities of 5 mW/mm^2 or less (Fig. 2-16 l), confirming its utility for optogenetic applications. Neurons expressing ChrimsonSA further showed significantly smaller blue-light evoked photocurrents, as compared to red light, than neurons expressing wild-type Chrimson, resulting in a higher red/blue light- activation ratio (Fig. 2-16 f–h). As a consequence, the action potentials were selectively evoked by red light, with a significantly decreased probability of blue-light-evoked action potential firing at similar intensities (Fig. 2-16 i–

l). Furthermore, due to the accelerated channel closing kinetics of this mutant, the recovery of the membrane potential after each spike was quicker as compared to neurons expressing wild-type Chrimson, leading to a more natural waveform of light-evoked action potentials (Fig. 2-17 c, d). Thus, ChrimsonSA is a useful optogenetic tool for neuronal spiking with far-red light and therefore of high value for dual-color optogenetic experiments.

2-5 Conclusion

Chrimson is widely used in optogenetic experiments since its red-shifted action spectrum allows deep tissue penetration of the excitation light, activation in a spectral range beyond the natural sensitivity of native photoreceptors in many animal species and combination with blue-light-activated tools for dual-color experiments. In the present study, the author has reported the crystal structure of Chrimson, which revealed substitutions and structural differences in the putative ion pore, as compared to the *Cr*ChRs, which contribute to the different gating kinetics and the elevated proton selectivity of Chrimson. While the putative ion pore shares similarity to other ChRs, the structural motifs of Chrimson around the retinal binding pocket are more similar to those of BR. Since ChRs presumably evolved from prokaryotic light-driven pumps[90], Chrimson might therefore reflect an early branching of ChRs during the molecular evolution from its prokaryotic ancestors. An extensive mutational analysis was performed, which revealed the structural features in the counterion region and retinal binding pocket that enable the red light absorption and fast channel gating transitions in Chrimson. Based on these findings, the author engineered ChrimsonSA, with further red-shifted peak absorption beyond 600 nm and strongly accelerated photocurrent closing kinetics. ChrimsonSA represents the most red-shifted microbial rhodopsin known to date that preserves protein function. Due to its reduced blue-light sensitivity, it is an excellent optogenetic actuator for dual-color applications.

2-6 Figures and table associated with Chapter 2

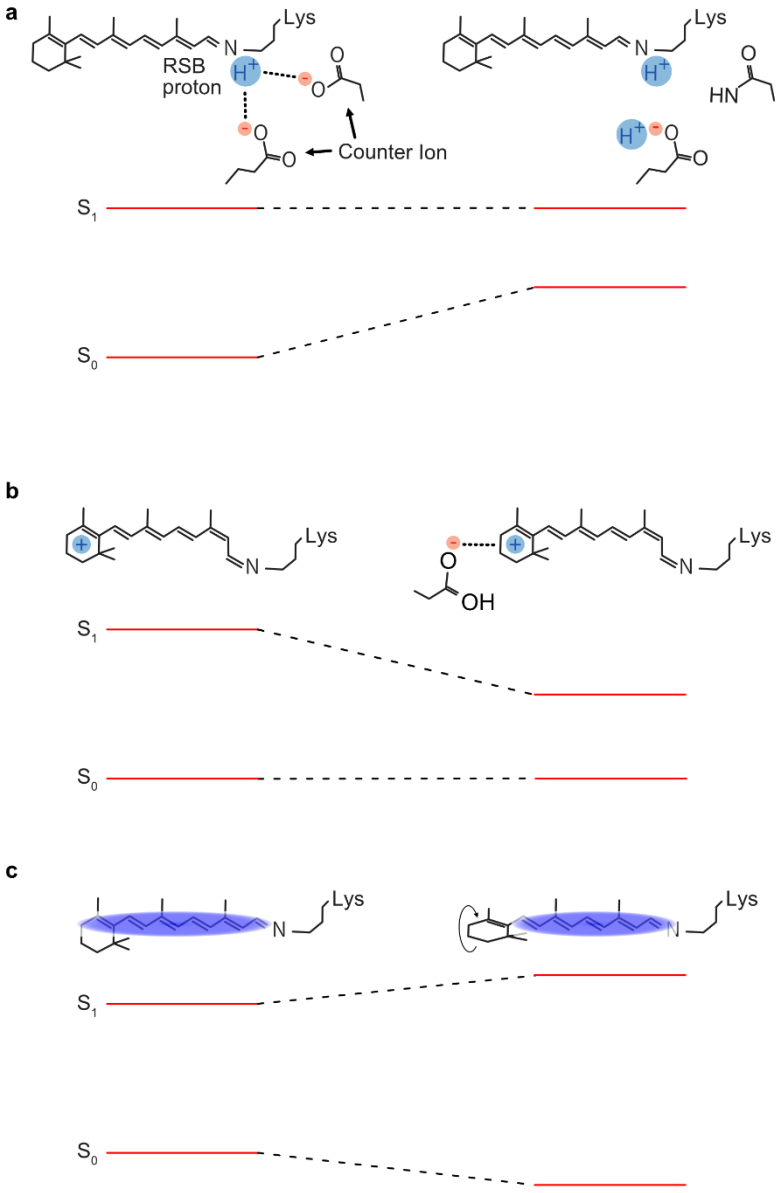

Fig. 2-1 Mechanism and schematic representation of rhodopsin absorption peak shift.

S_0 and S_1 represent the energy level of the ground state and excited state. The energy gap between S_0 and S_1 determines the rhodopsin absorption peak. **a**, The interaction between RSB proton and a negative charge of counter ion contributes to lower the S_0 level. **b**, The interaction between positive charges around the retinal β-ion ring and amino acid residues contributes to lower the S_1 level. **c**, The shrink of π-conjugated polyene chain contributes to absorption blue-shift.

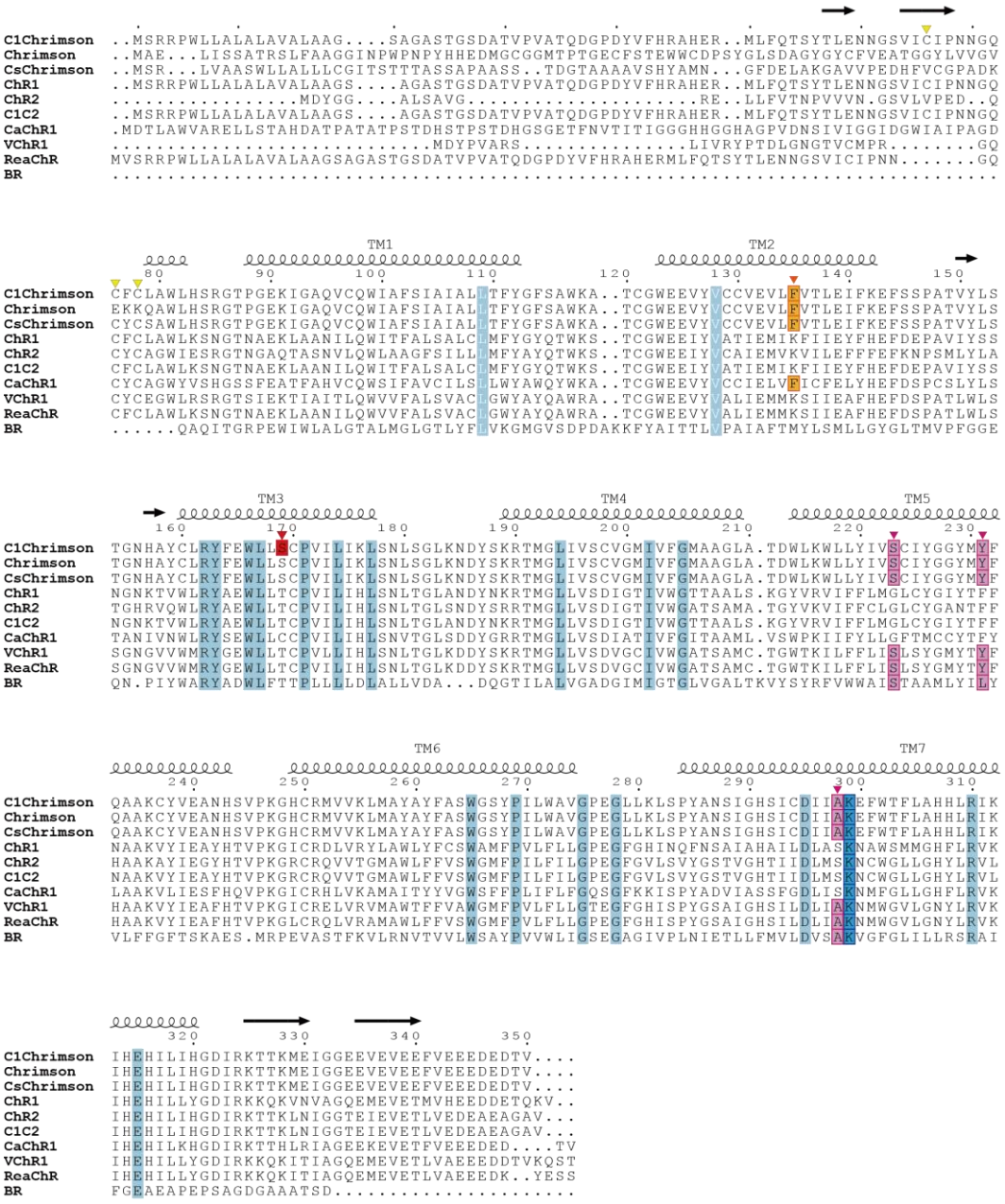

Fig. 2-2 Sequence alignment of C1Chrimson and ChR variants.

Amino acid sequences of C1Chrimson, Chrimson (CnChR1), CsChrimson, *Cr*ChR1, *Cr*ChR2, C1C2, CaChR1, VChR1, ReaChR, and BR are aligned. Secondary structures of C1Chrimson are indicated above the sequences. The N-terminal disulfide bond-forming cysteine residues are indicated by yellow arrowheads. The completely conserved sequences are highlighted in cyan, and the conserved lysine residues forming a linkage to the chromophore retinal are indicated in the blue panels. Residues important for the red-shift absorption are indicated by arrow heads, according to their contribution manners: counterion protonation (orange) and polarity of the retinal binding pocket (pink). The

position of the red-shift-causing point mutation (S169A) is indicated (red).

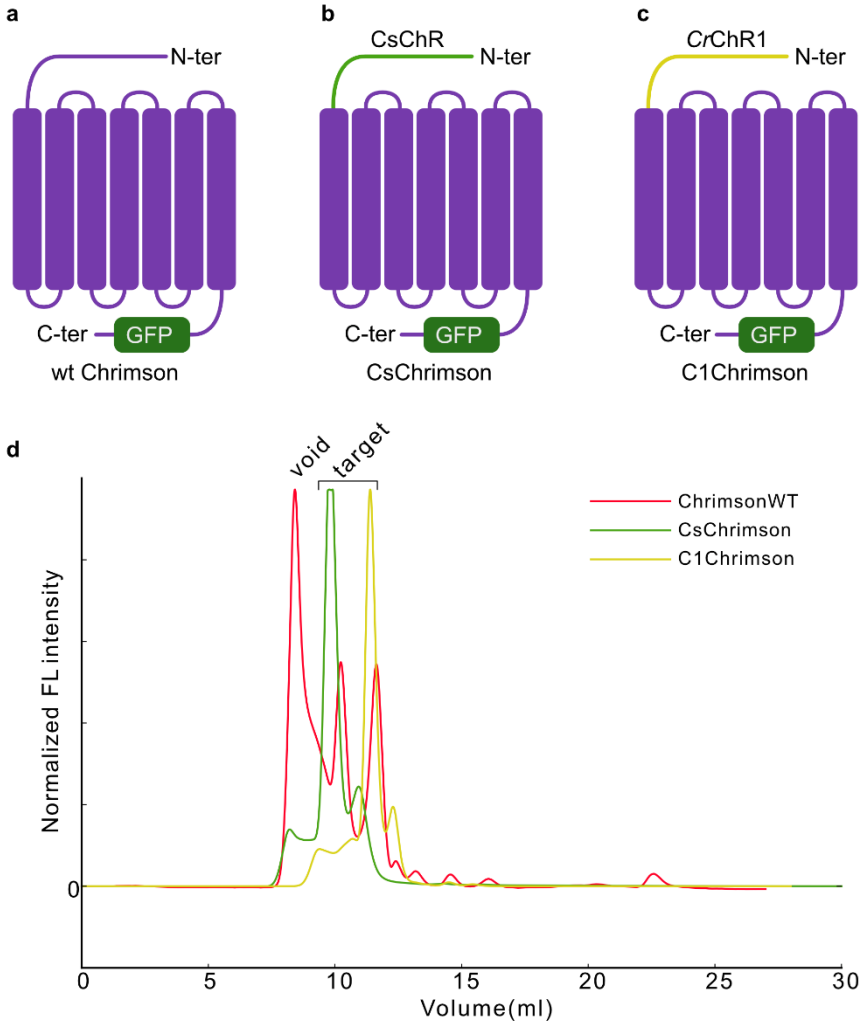

Fig. 2-3 Constructs and expression check of Chrimson.

a-c, Schematic model of Chrimson constructs. **d**, FSEC profile from **a-c** constructs. This experiment was performed by Satomi Oishi.

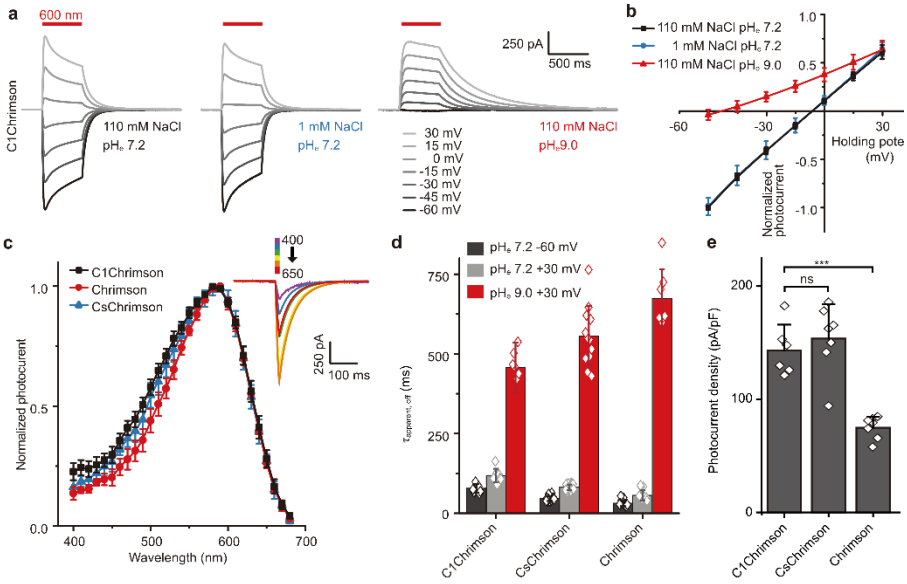

Fig. 2-4 Photocurrents of Chrimson variants.

Chrimson constructs were expressed in HEK cells and the photocurrents were measured. **a,** Representative photocurrents of C1Chrimson at different voltages with different extracellular solutions of 110 mM extracellular NaCl and pHe 7.2 (left), 1 mM NaCl and pHe 7.2 (middle) and 110 mM NaCl and pHe 9.0 (right) with intracellular 110 mM NaCl pHi 7.2. **b,** The current-voltage dependence of the normalized peak photocurrents of Chrimson under the ionic conditions described in (**a**) (Mean ± SD, n=5-16). **c,** Normalized peak photocurrents after 10 ms excitation at different wavelengths with equal photon count (Mean ± SD; n=6-10; Inlet: Representative photocurrents). **d,** Apparent off-kinetics (τapparent, off) at positive and negative voltages and pHe 7.2 and pHe 9.0 (Mean ± SD; n=7-16). **e,** Head-to-head comparison of photocurrent amplitudes of the Chrimson variants at -60 mV in symmetric 110 mM NaCl and pHe,i 7.2 (Mean ± SD, n=5-7). Significance was assessed by t-tests using Welch's correction in Origin 9.1®, with significance thresholds of $p < 0.05$ (*), $p < 0.01$ (**), $p < 0.001$ (***), and $p < 0.0001$ (****). p=0.5 for C1Chrimson and CsChrimson and p=0.0003 for C1Chrimson and Chrimson. These experiments and data analysis were performed by Johannes Vierock.

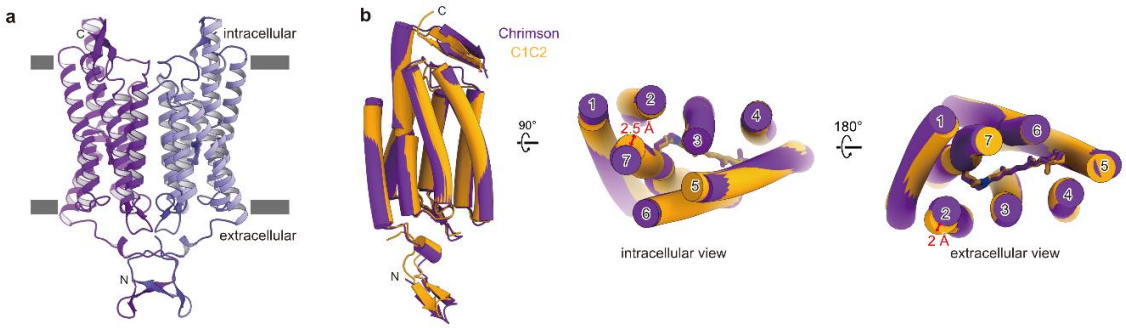

Fig. 2-5 Overall structure of Chrimson.

a, The dimeric structure of Chrimson is shown in ribbon models, with the two protomers in different colors. **b,** Chrimson (purple) and C1C2 (orange) are superimposed, viewed from within the membrane plane (left), the intracellular side (center) and the extracellular side (right). The TM numbering is indicated on each helix, and the deviation of the helix termini for TM2 and TM7 are indicated by red arrows.

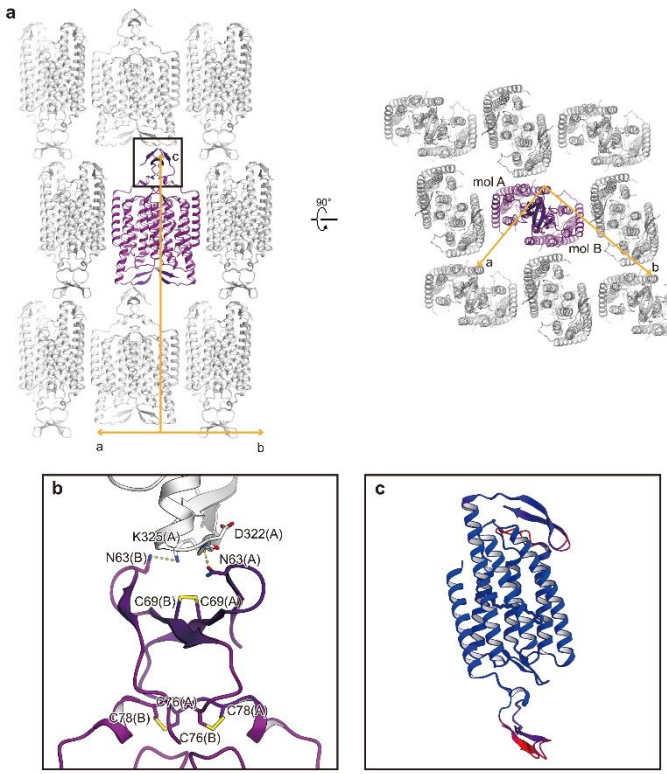

Fig. 2-6 Crystal packing of C1Chrimson.

a, The Chrimson proteins in the crystals are shown in ribbons, viewed from within the LCP crystal layer (left) and from the top (right). The a-, b- and c-axes are indicated by yellow arrows, and the two protomers (mol A and mol B) are shown. **b**, The N-terminal *Cr*ChR1-derived residues are involved in the crystal packing interactions between the

layers. Disulfide bond-forming cysteine and hydrogen bonding residues are shown as sticks, with the hydrogen bonding interactions indicated by yellow dotted lines. The letters in brackets indicate the respective molecules (A and B for mol A and mol B, respectively). **c**, Two protomers are superimposed and colored according to the distance of the Cα atoms between the protomers.

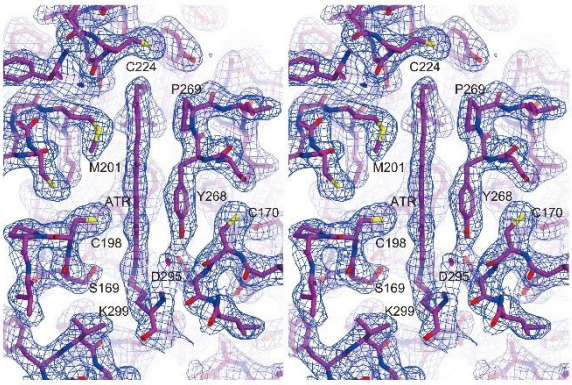

Fig. 2-7 Electron density of retinal.

A stereoview of the 2Fo-Fc electron density map for the retinal binding pocket is shown as a mesh representation, contoured at 1.1 σ. The all-*trans* retinal (ATR) and the surrounding residues are indicated by sticks.

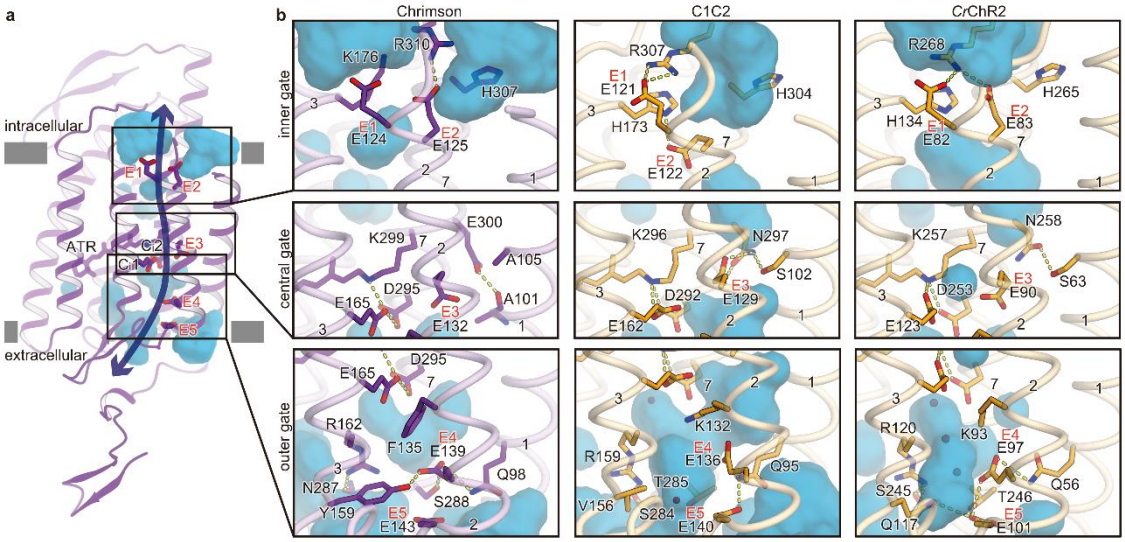

Fig. 2-8 Ion pores of Chrimson and ChRs.

a, Water accessible cavities are illustrated in the Chrimson structure, with the putative ion pathway indicated by an arrow. Five glutamic acid residues lining the ion pore (E1–5) and two counterion residues (Ci1 and Ci2) are indicated by sticks, and the three constriction sites for the inner, central and outer gates are indicated by boxes. Protein

internal cavities are shown as blue surface representations. **b,** Comparison of the constriction sites of Chrimson (left panels), C1C2 (center panels), and *Cr*ChR2 (right panels), for the inner (upper panels), central (middle panels), and outer (lower panels) gates. The constituent residues are shown as sticks, and the TM helix number is indicated on each helix. Protein internal cavities are shown as blue surface representations.

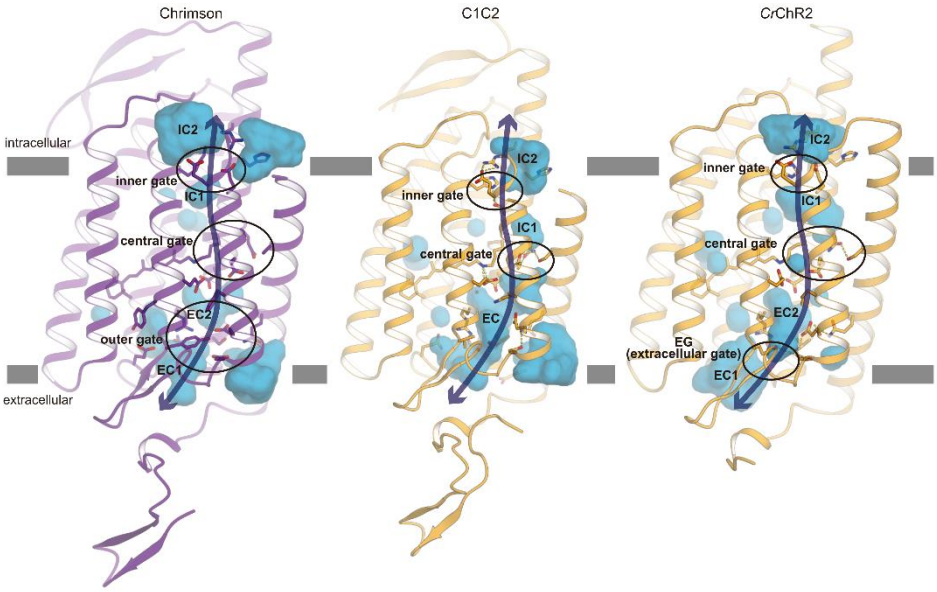

Fig 2-9 Comparison of the putative ion translocating pathway.

Protein internal cavities are shown as blue surface representations, for Chrimson (left), C1C2 (center) and *Cr*ChR2 (right). By observing discontinuities and locations, the author named these cavities according to the combination of the extracellular cavity (EC) or intracellular cavity (IC) and the sequential numbering from the extracellular to the intracellular side. The author observed three constrictions (inner, central and outer gates) and four cavities (EC1, EC2, IC1 and IC2) for Chrimson, two constrictions (inner and central gates) and three cavities (EC, IC1, and IC2) for C1C2, and three constrictions (inner, central and extracellular gates) and four cavities (EC1, EC2, IC1 and IC2) for *Cr*ChR2. Putative ion translocating pathways are indicated by navy arrows in each structure, and constriction sites are highlighted by circles.

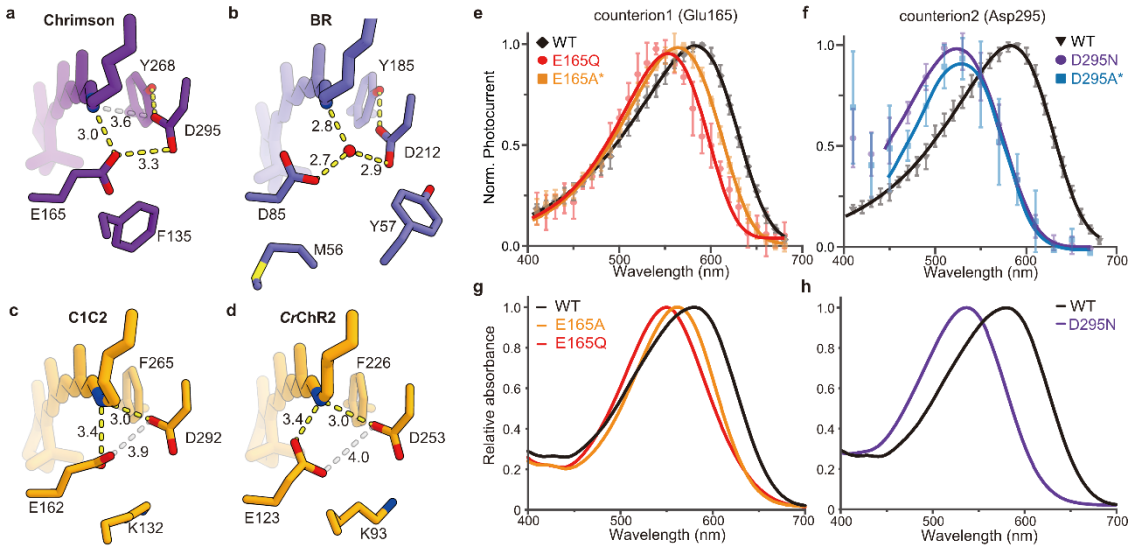

Fig. 2-10 Counterion configuration of Chrimson and adjacent residues.

a–d, Hydrogen-bonding interactions around the protonated Schiff base are shown for Chrimson (**a**), BR (**b**), C1C2 (**c**), and *Cr*ChR2 (**d**). Proposed hydrogen-bonding interactions are indicated by yellow dotted lines, and additional possible interactions with longer distances are indicated by gray lines, with the distance (Å) indicated beside each line. **e–h,** action (**e, f**) and absorption (**g, h**) spectra of the counterion residue mutants (Action spectra represent Mean ± SD; n = 5–7; symmetric 110mM NaCl, pHe,i 7.2 and −60 mV. Datasets indicated by asterisk are quoted from a previous study[70]. Same mutants are indicated by the same color codes. The fitted curves for the D295N and D295A action spectra were adjusted to the photocurrents activated by light of 440 nm or higher wavelength. The absorption spectrum of the D295A mutant could not be measured, due to its instability in the detergent solubilized form, and thus is not included in the panel (**h**). Action spectra (**e, f**) were measured by Johannes Vierock.

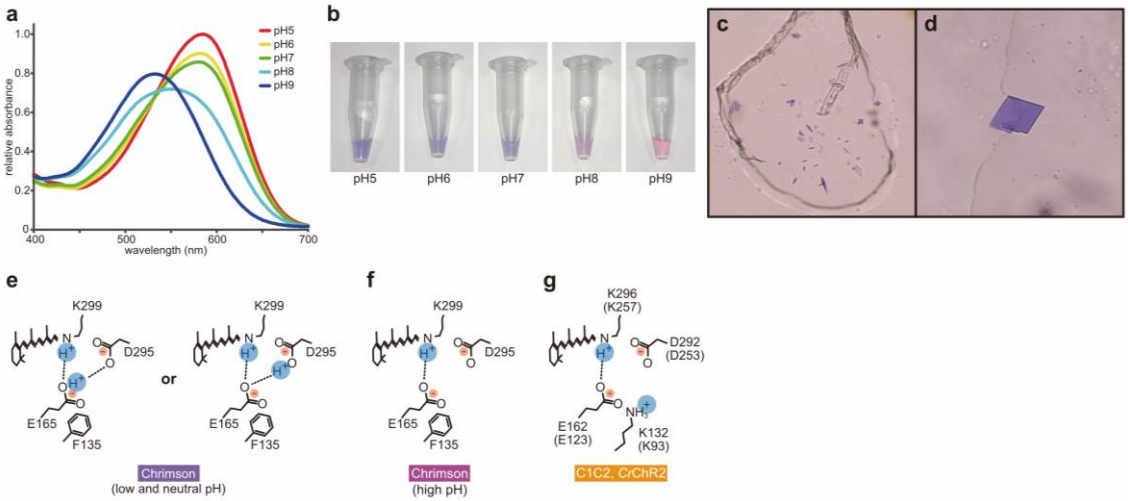

Fig. 2-11 pH-dependent peak shift and Schiff base environment.

a-b, Absorption spectra of the purified wild type Chrimson protein measured at the respective pH conditions (**a**). The color of the retinal chromophore is highly dependent on the solution pH. The Chrimson protein is blue at a lower pH, and red at higher pH. **c-d**, Crystals of Chrimson were obtained under low pH conditions, and accordingly the color of the crystal was blue. **e-g**, Proposed hydrogen bonding networks around the protonated Schiff base for Chrimson at low to neutral pH (**e**) and at high pH (**f**) and in C1C2 and *Cr*ChR2 (**g**).

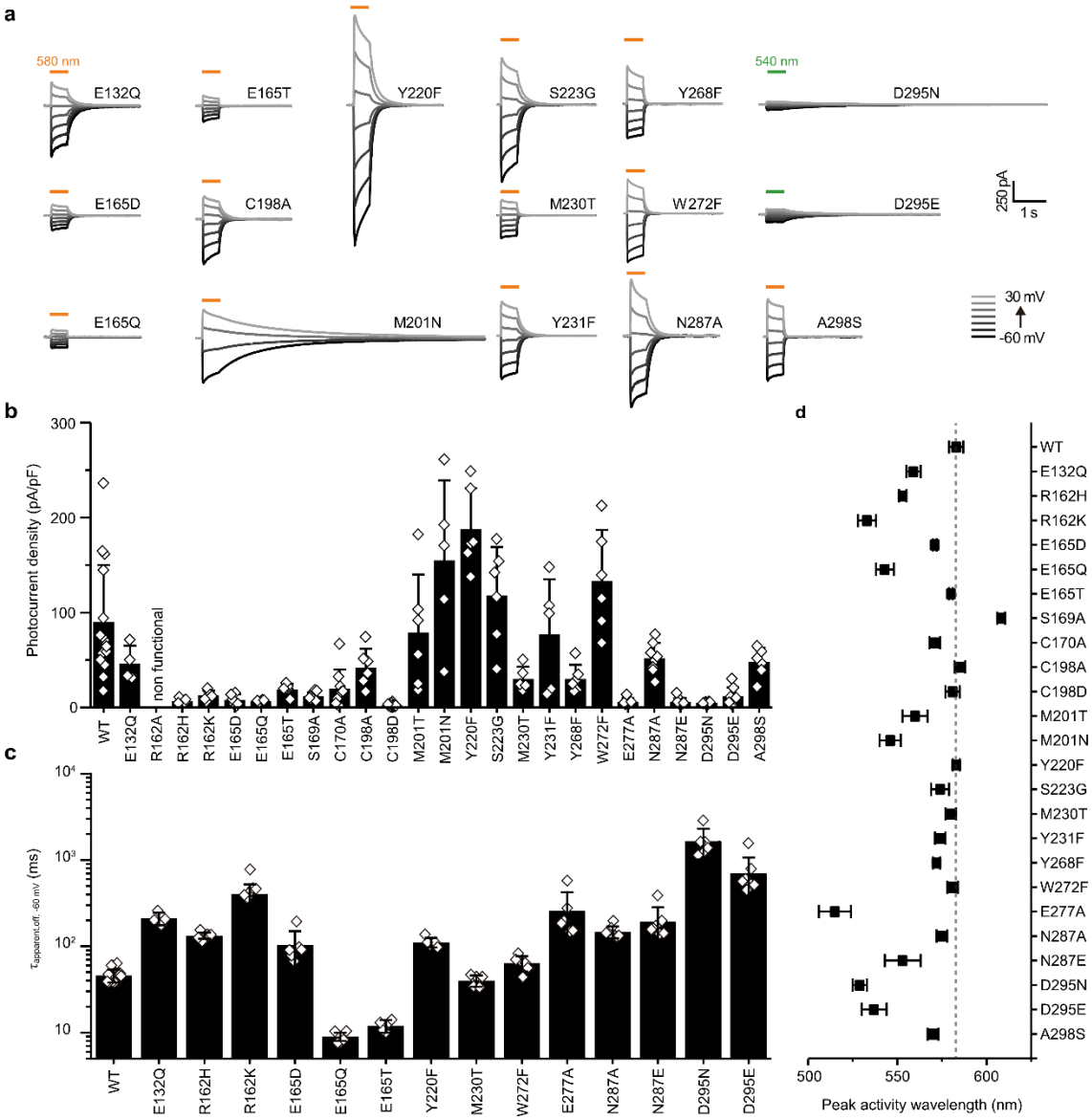

Fig. 2-12 Photocurrent traces and channel kinetics of mutant Chrimson.

a, Representative photocurrent traces of Chrimson mutants in symmetric 110 mM NaCl $pH_{i,e}$ 7.2 at different voltages, illuminated with either 540 nm light (green line) or 580 nm light (orange line), depending on the peak absorption. **b–d**, Characterization of Chrimson mutants. Photocurrent density (b), channel closing kinetics at -60 mV (c) and peak activity wavelength (Mean ± SD) (d) are shown. These experiments and data analysis were performed by Johannes Vierock.

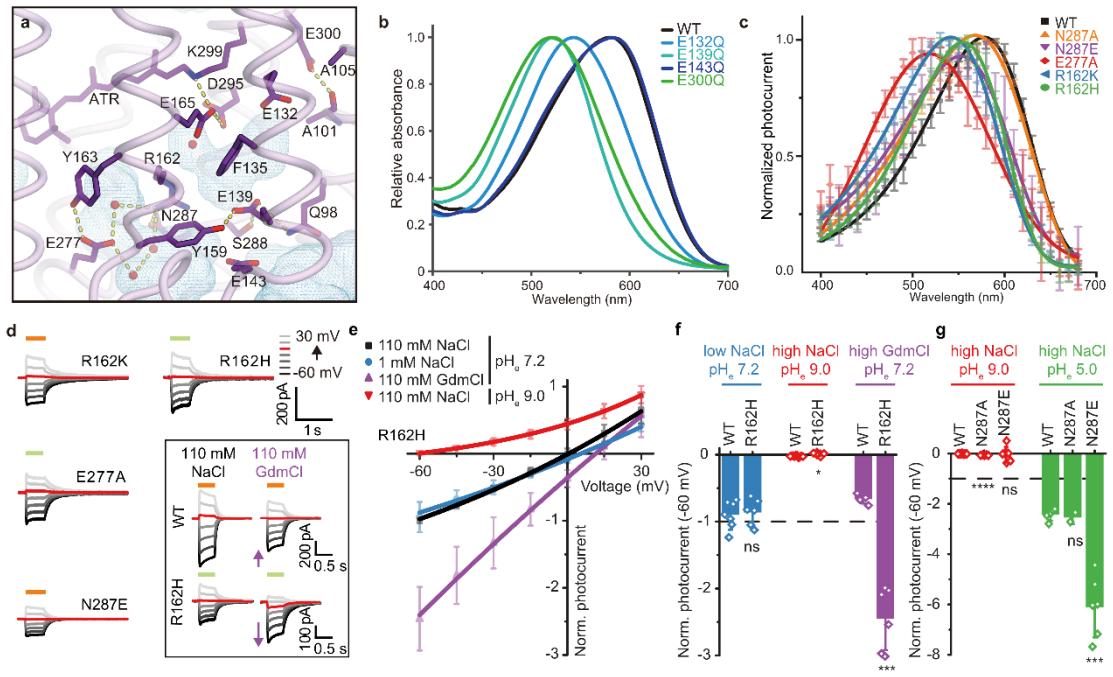

Fig. 2-13 Outer gate and the extracellular ion pore.

a, Residues around the outer gate are shown as sticks, with the interactions indicated by yellow lines. Water accessible cavities are indicated by blue meshes. **b,** Absorption spectra of the carboxylate mutants within the extracellular ion pore and the outer gate. **c,** Mutations in the extracellular ion pore caused blue-shifting of the action spectrum. Normalized peak photocurrents after 10 ms excitation at different wavelengths of equal photon count (Mean ± SD; n =5–7; symmetric 110mM NaCl, pHe,i 7.2 and −60 mV) are shown. **d,** Representative photocurrent traces of the Arg162 and Asn287 mutants at different voltages illuminated either with 550 nm light (green line) or with 580 nm light (orange line) depending on peak absorption. The inset shows representative photocurrent traces of wild type (upper) and R162H (bottom) upon replacement of Na+ with guanidinium. The purple arrows indicate the photocurrent increase or decrease upon cation exchange in the R162H mutant and Chrimson WT, respectively. **e,** Current-voltage dependence of normalized R162H photocurrents in extracellular solutions of different cation or proton composition (mean ± SD; n = 6–9; intracellular 110mM NaCl, pHi 7.2). R162H is still selective for protons, as the current-voltage dependence drastically shifts under the alkaline conditions (two-sample t-test with p = 0.025), while it is not affected by decreasing the Na+ ion concentration (p = 0.75). In contrast, the current-voltage dependence is drastically shifted when Na+ is replaced by guanidinium (p =0.0002), indicating that R162H is permeable to guanidinium. **f,** Normalized photocurrents at the ionic conditions of (**e**) and −60 mV compared to WT (Mean ± SD, n = 5–10; intracellular

110mM NaCl, pHi 7.2, junction potential corrected). **g,** Normalized photocurrent amplitudes of WT and N287 mutants at different extracellular pH (Mean ± SD; n = 2–10; intracellular 110mM NaCl, pHi 7.2; −60 mV). Photocurrents of both mutants and WT were equally reduced at low proton concentration indicating comparable high proton selectivity (two-sample t-test compared to WT with $p < 0.0001$ for N287A and $p = 0.9$ for N287E). At extracellular pH 5.0 photocurrent increase of the N287E mutant was significantly higher than for WT or the N287A mutant ($p = 0.5$ for N287A and $p = 0.0005$ for N287E). The action spectrum, photocurrent and current-voltage dependency were measured by Johannes Vierock.

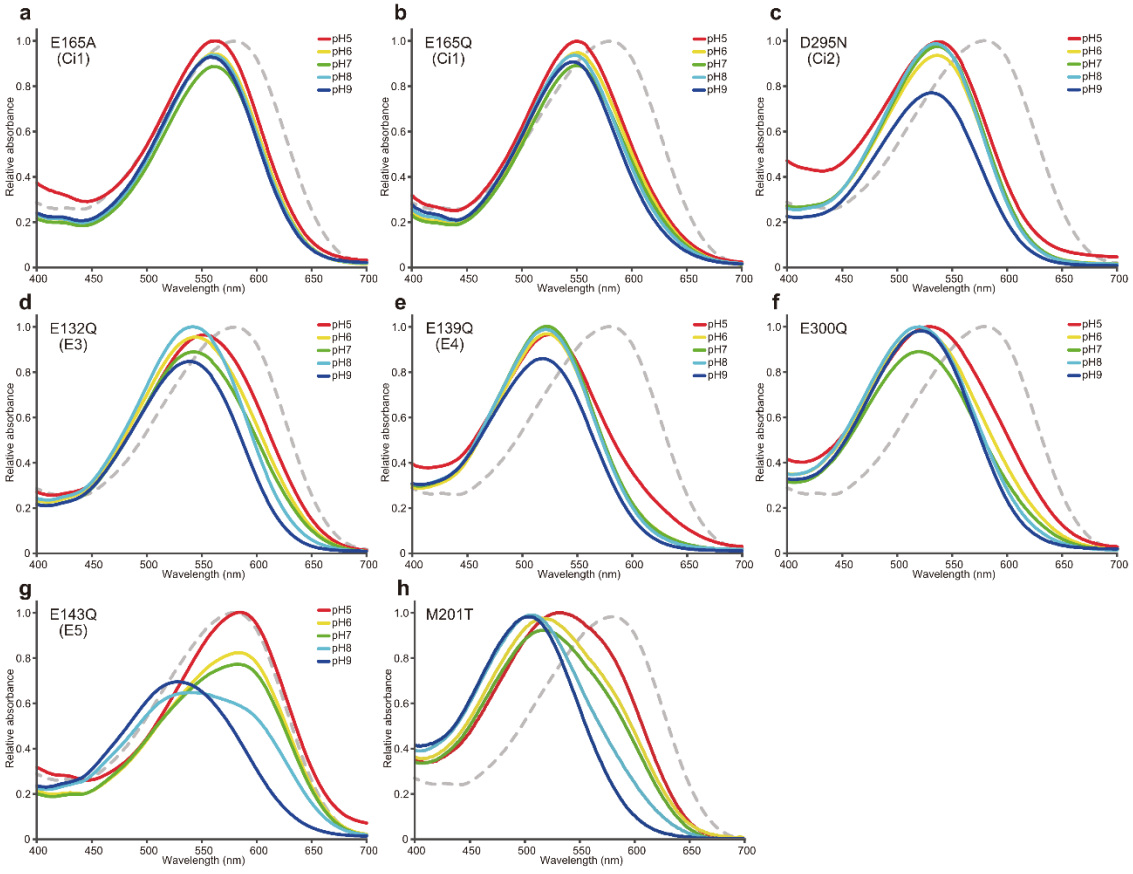

Fig. 2-14 Absorption spectra of Chrimson mutants.

a-h, Absorption spectra of Chrimson mutants measured at different pH conditions are shown. Gray dotted lines indicate the absorption spectrum of wild type Chrimson at pH 7. The mutations of E165, E132, E139 and E300 all caused large blue-shifted absorption, while the mutation of E143 did not affect either the absorption spectrum or pH-dependency. The M201T mutant showed the largest blue-shift among the tested mutants.

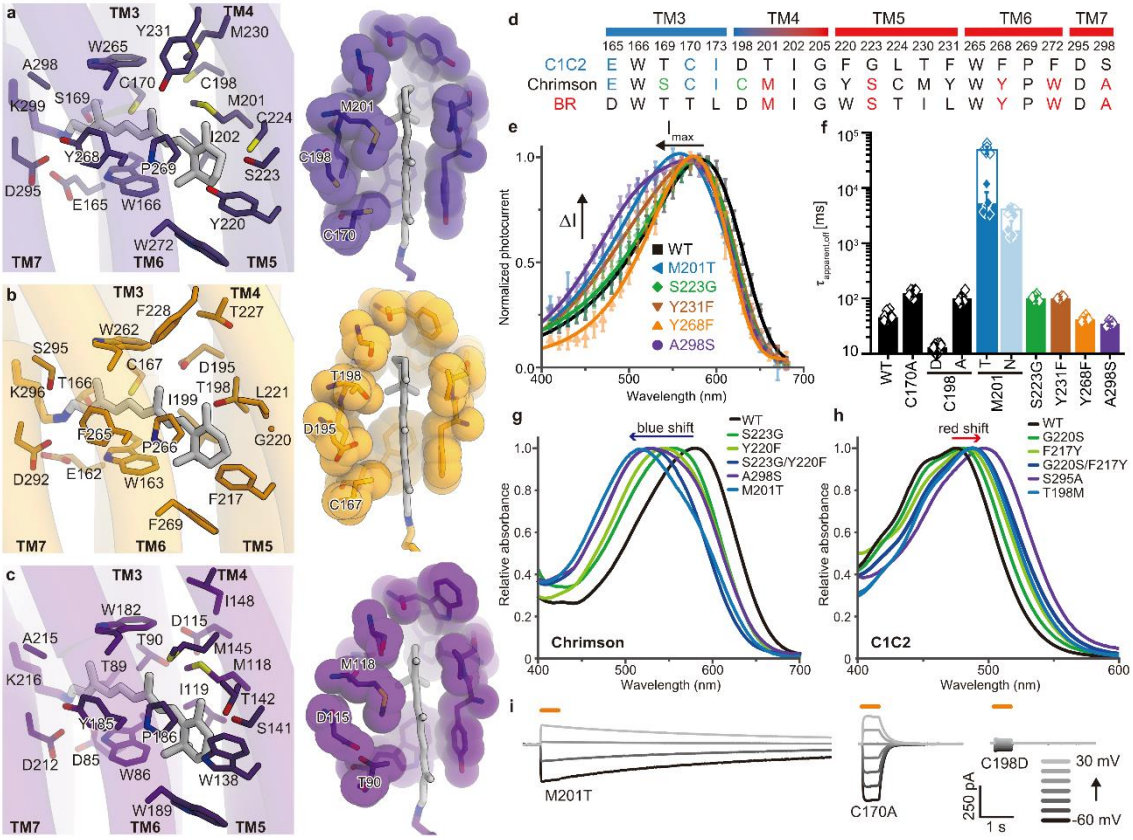

Fig. 2-15 Retinal binding pocket.

a–c, Structural comparisons of the retinal binding pockets of Chrimson (**a**), C1C2 (**b**), and BR (**c**). As the retinal pockets of C1C2 and *Cr*ChR2 are quite similar, C1C2 is shown as the representative structure of the *Cr*ChRs. Residues constituting retinal binding pocket are shown in sticks (left panels). CPK model representations show different associations in the retinal binding pocket (right panels). **d,** Sequence comparison of Chrimson with C1C2 and BR. The residue numbering of Chrimson is indicated above the sequence. Chrimson resembles BR in TM5–7, surrounding the polyene chain and β-ionone ring, while it resembles C1C2 (or *Cr*ChRs) in TM3, located near the ion-conducting pore. Residues common to BR and C1C2 are depicted in cyan and red, respectively. **e,** Mutations that affect action spectrum. Normalized peak photocurrents after 10 ms excitation at different wavelengths of equal photon count (Mean ± SD; n = 5–8; symmetric 110mM NaCl, pHe,i 7.2 and −60 mV) are shown. **f,** Apparent photocurrent off-kinetics of retinal binding pocket mutants (τapparent off; Mean ± SD; n =5–11; symmetric 110mM NaCl, pHe,i 7.2 and −60 mV). Empty columns for M201T and M201N represent conductance measurements by short 20 ms voltage pulses to −60 mV at 0.2 and 0.5 Hz, respectively, and at a holding potential of 0mV in order to reduce kinetic artifacts imposed by intracellular acidification due to continuous proton influx as

previously reported[70] (Mean ± SD; n = 5–6). **g, h** Absorption spectra of wild type and mutant Chrimson (**g**) and C1C2 (**h**). Mutations at the same positions are indicated by the same color codes. Peak shifts caused by mutation is indicated by a blue or red arrow. **i** Representative photocurrent traces of the M201T, C170A, and C198D mutants, measured at different voltages in symmetric 110mM NaCl, pHe,i 7.2 and illuminated with 580 nm light (orange line). The action spectrum and photocurrent were measured by Johannes Vierock.

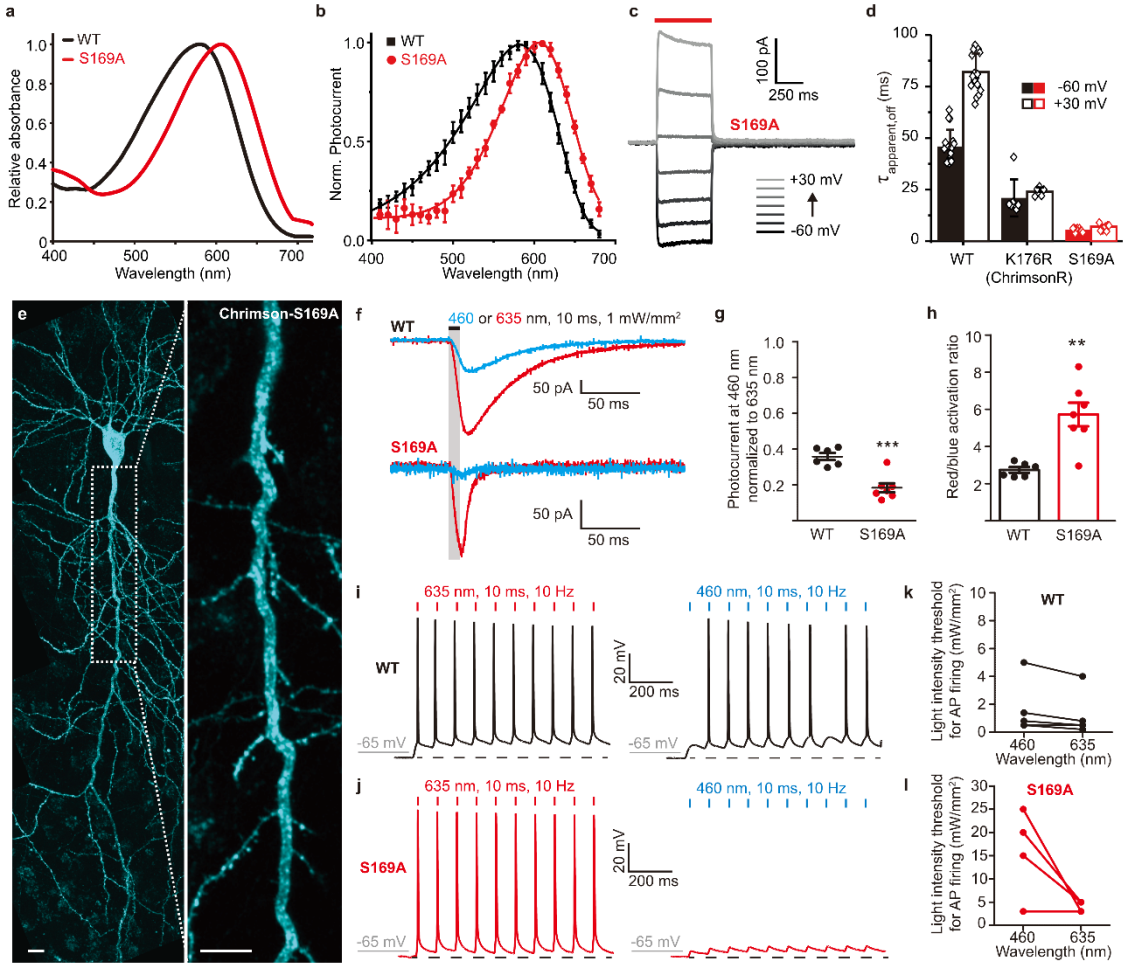

Fig. 2-16 Chrimson-S169A in rat CA1 pyramidal cells.

a-b, Red-shifted absorption spectrum (**a**) and action spectrum (**b**) of Chrimson S169A (ChrimsonSA) (Mean ± SD; n=7; 10 ms illumination of equal photon counts, symmetric 110mM NaCl, pHe,i 7.2 and −60mV). **c-d,** Photocurrents of ChrimsonSA in HEK cells. Representative photocurrent traces (**c**) and channel closing kinetics (**d**) at the same ionic conditions as in (**b**) are shown. **e,** CA1 pyramidal neuron heterogeneously expressing

ChrimsonSA-mCerulean, 5 days after electroporation (stitched maximum intensity projections of two-photon images). The inset shows a magnified view of the apical dendrite. The scale bars indicate 10 μm. **f,** Representative photocurrent traces of Chrimson-WT (top) and ChrimsonSA (bottom) expressing CA1 pyramidal cells evoked with either 635 nm (red trace) or 460 nm (blue trace, 1mW/mm2) light. The ChrimsonSA traces were scaled to WT Chrimson **g,** Relative photocurrent responses of WT Chrimson and ChrimsonSA to blue light (460 nm, 10ms, 1mW/mm2). Values were normalized to the response to red light (635 nm, 10 ms, 1mW/mm2). Dots represent single cells. Lines show mean ± SEM (nWT=6; nS169A=7). **h,** Quantification of the red/blue activation ratio. Bar plots show mean ± SEM. **i-j,** Action potentials triggered by red light pulses at a frequency of 10 Hz in cells expressing WT Chrimson (**i**) and ChrimsonSA (**j**) at threshold light intensities of 0.5 and 5mW/mm2, respectively. Using the same light intensities, the action potentials were triggered by blue light in WT, but not in the ChrimsonSA. Dashed lines represent the membrane resting potential. **k-l,** The light intensities at 460 nm and 635 nm required to reach the action potential threshold in neurons expressing WT Chrimson (**k**) or ChrimsonSA (**l**). The action spectrum and photocurrent were measured by Johannes Vierock. The assay using CA1 cells was performed by Silvia Rodriguez-Rozada.

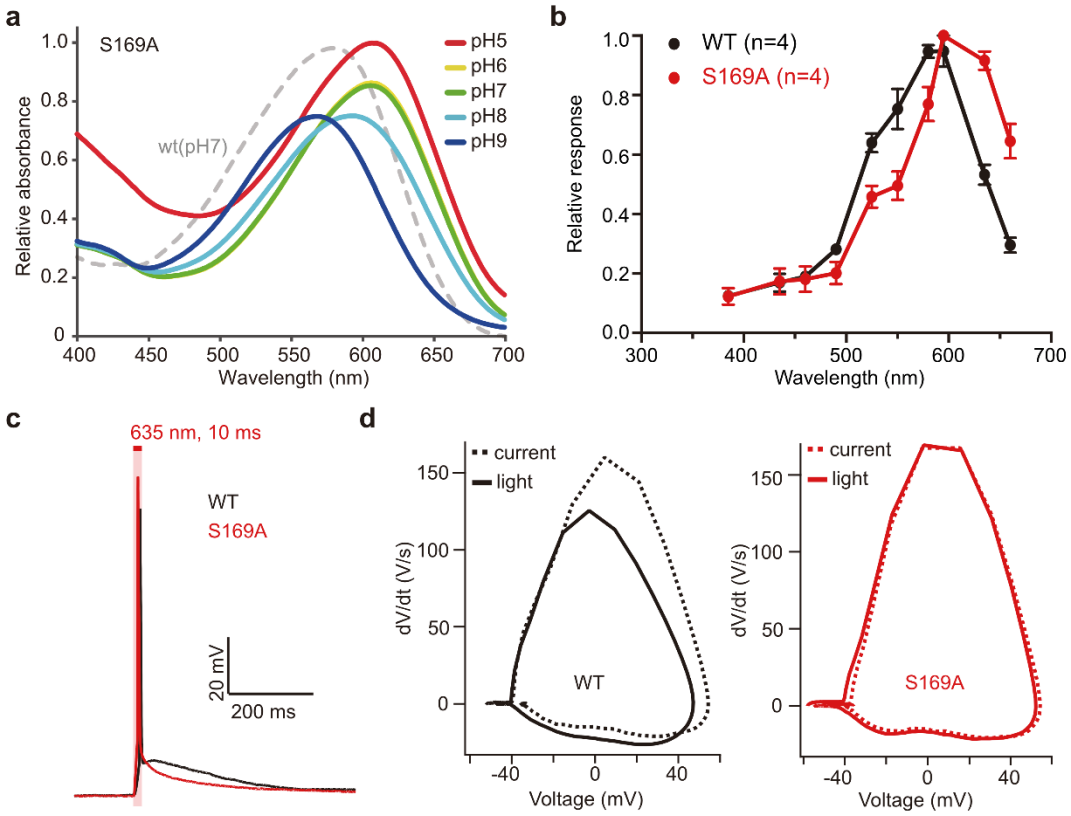

Fig. 2-17 pH-dependency and neuronal characterization of ChrimsonSA.

a, Absorption spectra of ChrimsonSA, measured under different pH conditions. Gray dotted lines indicate the absorption spectrum of wild type Chrimson at pH 7. **b**, Peak-normalized photocurrents in neurons expressing either WT Chrimson (black) or Chrimson-S169A (red, Mean ± SEM). **c**, Single action potentials in neurons expressing either WT Chrimson (black) or ChrimsonSA (red). **d**, Phase plots of action potentials evoked with 300 pA current injections (dashed lines) or with 8-ms red light pulses (solid lines) in neurons expressing either WT Chrimson (black) or ChrimsonSA. Neuronal characterization of ChrimsonSA was performed by Silvia Rodriguez-Rozada.

Table 1. Data collection and refinement statistics

	Chrimson
Data collection	
Beamline	SPring-8 BL32XU
Space group	$P2_12_12_1$
Number of crystals	13
Cell dimensions	
a, b, c (Å)	60.99,81.44, 170.14
α, β, γ (°)	90.0, 90.0, 90.0
Wavelength	1.0000
Resolution (Å)	50-2.60 (2.69-2.60)
R_{meas}	0.144 (0.591)
$CC_{1/2}$	0.980 (0.595)
I / σI	13.8 (1.7)
Completeness (%)	100.0 (100.0)
Redundancy	9.3 (9.2)
Refinement	
Resolution (Å)	50-2.60 (2.69-2.60)
No. reflections	26744 (2618)
R_{work}/R_{free}	0.229/0.277 (0.313/0.358)
No. atoms	
Protein	4410
Water/Ion/Lipid	411
B-factors	
Protein	85.6
Water/Ion/Lipid	80.8
R.m.s. deviations	
Bond lengths (Å)	0.005
Bond angles (°)	0.96
Ramachandran plot	
Favored (%)	95.6
Allowed (%)	4.4
Disallowed (%)	0

Chapter3: Time-resolved serial femtosecond crystallography analysis of channelrhodopsin

3-1 Introduction

3-1-1 Channel kinetic of Channelrhodopsin

In addition to the studies about absorption peak shift of ChRs, many studies about channel kinetics of ChRs have also been reported[59,84,91–93]. Especially, amino acid residues that consist of retinal binding pocket tend to be conserved in ChRs and these residues could be a potential candidate not only for color-tuning but also for altering kinetics and accumulation of the conducting state[84,94]. Through mutation analysis of these amino acid residues, different phenotypes of photocycle have been identified. As fast photocycle kinetics, *Cr*ChR2 mutants involving E123 are designed and termed "ChETA" variants (E123A and E123T)[92,93] (Fig. 3-1 a). On the other hand, *Cr*ChR2 mutants involving C128 and D156 showed slowed the open/close kinetics of the channel, resulting in the step function opsin (SFO) mutants, with currents that can be switched by different wavelengths of light[84]. These residues are highly conserved among most ChRs and interacted with each other. Therefore, these residues are considered as critical residues for channel gating and termed D-Cpair[63,84] (Fig. 3-1 b). FTIR and structural studies have suggested that D156 functions as the internal proton donor for the deprotonated Schiff base, via an internally hydrated water molecule and C128[85,95,96]. A previous FTIR study showed an increase of the S-H stretching frequency of the C128 side chain upon light illumination[97].

However, these residues are not associated with ion pore formation (Fig. 3-1 c) and the detailed mechanism of ion pore formation is still under debate. Recent studies have suggested that the ion-conducting pore is formed during the late P_2^{390} intermediate, involving the rearrangement of the pore-forming TM helices[98], and the two-dimensional crystal study indeed revealed low-resolution projection maps of the light-induced helix movement in ChR[99,100]. A detailed mechanism for how retinal isomerization causes conformational changes and how these changes induce ion pore opening has remained elusive.

3-1-2 Time-resolved serial femtosecond crystallography

The recent development of the X-ray free electron laser (XFEL) technology has enabled high-resolution visualization of the time-resolved molecular conformational

changes in crystals, thus profoundly advancing our understanding of biological reactions[101–104]. This technique is called “time-resolved serial femtosecond crystallography” (TR-SFX). In the TR-SFX experiment, microcrystals are continuously delivered to an XFEL focal point using a sample injector at room temperature and a reaction in microcrystals is initiated with stimulation such as light illumination. The progress of the reaction is probed after a time delay by the XFEL[105,106].

3-1-3 Study purpose

To understand the ChR channel kinetics or ion pore formation, high-resolution structures or open form structure of different states have been urgently needed. In this study, the author performed TR-SFX analysis of ChR, which revealed the critical conformational changes occurring early in the photocycle that probably induces the cation permeation in the later stages.

3-2 Materials and method

3-2-1 Plasmid construction, expression and purification

The author used a chimeric construct between *Chlamydomonas reinhardtii* ChR1 (*Cr*ChR1) and ChR2 (*Cr*ChR2) for the TR-SFX experiments (hereafter referred to as C1C2)[51,107,108] (Fig. 3-2), which has normal photocycle properties[107] (Fig. 3-3 a, b). That is because C1C2 crystal has only minimal interactions at the extra-membrane region and it is suggested that the effect of crystal packing is smaller than that of *Cr*ChR2 crystal. C1C2 Chimeras was cloned into a modified pFastBac expression vector (Invitrogen), which includes a C-terminal His8 tag, a GFP-tag and a tobacco etch virus (TEV) protease cleavage site[51]. The modified C1C2 construct was expressed in Sf9 cells, using the Bac-to-Bac baculovirus expression system (Invitrogen). Baculovirus-infected Sf9 cells were cultured in Sf900II (Invitrogen) at 27 °C for 24 h, and all-trans retinal (SIGMA-ALDRICH) was added after 24 h post-infection at the final concentration of 20 μM. Cells were harvested 48 h after infection by centrifugation at 6000× g for 10 min. The pellets were disrupted by sonication and resuspended in a buffer containing 150 mM NaCl, 50 mM Tris-HCl, pH 8.0, 5% glycerol and 0.1 mM phenylmethylsulfonyl fluoride (PMSF). The cell debris was cleared by centrifugation at 10,000× g for 30 min, and the crude membrane fraction was collected by ultracentrifugation (Ti45 rotor, 215,000× g, 1 h). This fraction was solubilized in buffer containing 150 mM NaCl, 50 mM Tris-HCl, pH 8.0, 5% glycerol, 0.1 mM PMSF, 2.5% n-dodecyl-β-D-maltoside (DDM), and 0.5% cholesteryl hemisuccinate (CHS). The insoluble material was removed by

ultracentrifugation (Ti70 rotor, 208,000× g, 30 min), and the supernatant was mixed with Ni-NTA resin (QIAGEN). After binding for 1.5 h, the flow-through was discarded. Following the cleavage of EGFP–His8 by TEV protease (homemade), the flow-through containing C1C2 was collected, concentrated, and further purified by size-exclusion chromatography in 150 mM NaCl, 50 mM Tris-HCl, pH 8.0, 5% glycerol, 0.05% DDM, and 0.01% CHS. Peak fractions were pooled and concentrated to ~15 mg/ml for crystallization.

3-2-2 Laser flash photolysis experiment

These experiments were perfomed by Keiichi Inoue. The time-evolution of the transient absorption changes of photo-excited C1C2 was measured as previously described[109,110]. The purified protein sample was solubilized in buffer containing 150 mM NaCl, 50 mM Tris-HCl (pH 8.0), 0.05% DDM, 5% glycerol, and 0.01% CHS. For the measurement of C1C2 in liposomes, the purified C1C2 protein was mixed with a lipid mixture of palmitoyloleoyl phosphatidylethanolamine (POPE) and palmitoyloleoyl phosphatidylglycerol (POPG) (molar ratio = 3: 1) at a protein-to-lipid molar ratio of 1: 50 (the final concentrations of C1C2 and lipids were adjusted to 5 μM and 250 μM, respectively), and the DDM was removed by BioBeads (SM-2, Bio-Rad). The sample solution was placed in a quartz cuvette with a 1-cm optical path length and illuminated with a 480-nm beam generated by an optical parametric oscillator (OPO) system, pumped by the third harmonics generation of a nanosecond Nd^{+}: YAG laser (LT-2214, LOTIS TII, Minsk, Republic of Belarus). The intensities of the transmitted probe light from a Xe arc lamp (L8004, Hamamatsu Photonics, Japan) were measured before and after laser excitation with an ICCD linear array detector (C8808-01, Hamamatsu, Japan) at 24°C, and transient absorption spectra were obtained by calculating the ratios between them. Ninety spectra were averaged to improve the signal-to-noise (S/N) ratio. To obtain the detailed time evolution of the transient absorption change after photoexcitation, the change in the intensity of the monochromated output of a Xe arc lamp (L9289-01, Hamamatsu Photonics, Japan), passed through the sample at 24°C, was observed by a photomultiplier tube (R10699, Hamamatsu Photonics, Japan) at 375, 445, and 520 nm. The signal from the photomultiplier tube was averaged to improve the S/N ratio and stored in a digital-storage-oscilloscope (DPO7104, Tektronix, Japan). The obtained kinetics data were fitted with a multi-exponential function. Dark adaptation kinetics of C1C2 was measured for the 0.05% DDM-solubilized sample at 24°C, as previously described[110]. The dark-adapted sample was illuminated for 1 min by using the output from a 1-kW tungsten–halogen projector lamp (Master HILUX-HR, Rikagaku, Japan), through

an interference filter at 460 nm. After turning off the light, the spectra or the absorption at a specific wavelength were measured by a UV-visible spectrometer (V-730, JASCO).

3-2-3 Flash photo-activation current measurement

These experiments were performed by Johannes Vierock. HEK293 cells were cultured in Dulbecco's Modified Medium (Biochrom), supplemented with 10% (v/v) fetal bovine serum (FBS Superior; Biochrom), 1 µM all-*trans* retinal, and 100 µg/ml penicillin/streptomycin (Biochrom, Berlin, Germany). Cells were seeded on poly-lysine coated glass coverslips at a concentration of 1 x 10^5 cells/ml and transiently transfected using the FuGENE® HD Transfection Reagent (Promega) 28–48 h before measurement. C1C2 was fused to an mCherry-fluorophor and expressed under the control of the CMV-promotor.

Patch pipettes were prepared from borosilicate glass capillaries (G150F-3; Warner Instruments) using a P-1000 micropipette puller (Sutter Instruments), and fire polished with a final pipette resistance of 1.5 to 3.0 MΩ. Fluorescent cells were identified using an Axiovert 100 inverted microscope (Carl Zeiss). Single ns laser pulses were generated by an Opolette Nd:YAG laser/OPO system (OPOTEK), selected by an LS6ZM2 shutter system (Vincent Associates), and delivered to the cells through the optics of the microscope and a 90/10 beamsplitter (Chroma). The laser intensity was set to 5% using the built-in motorized variable attenuator, resulting in a pulse energy of 100 ± 20 µJ/mm. Photocurrents were recorded with an AxoPatch 200B amplifier (Molecular Devices) at a maximal bandwidth of 100 kHz, and digitized using a DigiData 1440A digitizer (Molecular Devices) at a sampling rate of 250 kHz. Membrane resistance was typically > 1 GΩ, while access resistance was below 10 MΩ. Pipette capacity, series resistance, and cell capacity compensations were applied. A 140 mM NaCl agar bridge was employed for the reference bath electrode. Intracellular pipette and extracellular bath solutions contained 110 mM NaCl, 1 mM KCl, 1 mM CsCl, 2 mM $CaCl_2$, and 2 mM $MgCl_2$, and were buffered to pH 6.0, 7.2, or 8.0 by 10 mM MES, HEPES, or TRIS (with glucose added to 290 mOsm for intracellular and 310 mOsm for extracellular solutions). Measurements were controlled by the pCLAMP™ software (Molecular Devices). Post measurement photocurrent recordings were the first baseline corrected and time-shifted to align with the rising edges of the Q-switch signals of the laser pulse, using the Clampfit 10.4 software (Molecular Devices). They were then binned to 50 logarithmically spaced data points per temporal decade, normalized to peak photocurrents at -60 mV, and averaged for up to ten individual repetitions for each cell and voltage condition with a custom-written Matlab script (MathWorks). Kinetic analysis was performed in Origin

9.1® (OriginLab). Passive photocurrents were calculated by subtracting the photocurrents at 0 mV, which were recorded in the absence of an electrochemical gradient and represent the inner protein charge transfer reactions. For sufficient statistical significance, each measurement was repeated multiple times on different biological replicates, in at least three independent experiments. The exact number of biological replicates for each measurement is provided in the figure legend.

3-2-4 Time-resolved visible absorption spectroscopy

These experiments were performed by Takashi Nomura and Minoru Kubo. The photocycle reaction was induced by a 6-ns, 470-nm pump pulse from an OPO (NT230, EKSPLA), and the spectral changes during the reaction were measured by using a fiber-coupled spectrometer (Flame-S, Ocean Optics), with a microsecond white-light probe pulse from a Xe-flash lamp (L11316-11-11, Hamamatsu Photonics). A portion of the probe light (5%) was used to correct the pulse-to-pulse fluctuation of the probe light intensity. The pump pulse and the probe light were focused on the sample point, with beam diameters of 300 μm and 40 μm, respectively. The pump energy was reduced to 15 μJ (0.21 nJ/μm), to avoid sample damage by the repetitive pump illuminations during the data accumulation. The pump pulse, the probe light source, and the spectrometer were synchronized by pulse generators (DG645, Stanford Research Systems), and the pump-probe delay time was adjusted with a timing jitter of ± 20 ns. The repetition rates of the pump and the probe were 0.5 Hz and 1 Hz, respectively. In the solution measurement, the sample was packed in a spinning quartz cell with an optical path length of 1 mm and spun at 50 rpm during the measurement. The sample concentration was ~10 mg/ml, dissolved in 50 mM Tris-HCl, pH 8.0, containing 150 mM NaCl and 5% glycerol. In the microcrystal measurement, the author used the C1C2 crystals obtained under similar conditions as in the TR-SFX (below). Specifically, a pillar of 30 μl protein-laden LCP, approximately 2 cm in length, was extruded from the syringe and soaked in 900 μl of the crystallization buffer, containing 100 mM HEPES, pH 7.0, 280 mM KH_2PO_4, and 30% PEG500DM, and incubated for 1 week in the dark at 20°C, which yielded crystals in a liquid sponge phase floating on the buffer solution. The sponge phase layers were transferred by pipetting and packed in two quartz windows with a 50 μm-thick spacer. Only a few absorption signals from the non-crystallized area were observed, and the transmitted light intensity from the non-crystallized area was used as the reference to calculate the absorption spectra of C1C2. The sample temperature was kept at 20ºC for both the solution and microcrystal measurements. To decrease the noise level of the time-resolved spectra, singular value decomposition (SVD)[111] was used with Igor Pro (Wave

Matrix). In the SVD, matrix A comprising the intensity changes at each wavelength and time (column and row, respectively) was decomposed according to $A = USV^{T}$, where S represents a diagonal matrix with the singular values in decreasing order. This allows an evaluation of the number of significant orthonormal basis vectors for the wavelength (columns of U) and the time (columns of V). By reconstructing the matrix A' from only the most significant components, random noise was eliminated from the raw spectra. The time-resolved spectra for the microcrystal and solution samples were well reconstructed by two and three components, respectively. Based on the SVD, global fitting was then performed for the time-resolved reconstructed spectra with Igor Pro (Wave Matrix). In the global fitting, the spectra were fitted with a sum of exponentials with apparent time constants τ_i as global parameters, where i is the number of components used for the spectral reconstruction in the SVD analysis.

3-2-5 Crystallization of C1C2

This experiment was performed by Nureki laboratory membrane group members, including me. C1C2 was mixed with monoolein (Sigma) in a 2:3 protein to lipid ratio (w/w), using a 100 μl volume Gastight syringe (Hamilton). A pillar of 30 μl protein-laden LCP, approximately 2 cm in length, was extruded from the syringe and soaked in 900 μl of the crystallization buffer, containing 100 mM MES, pH 6.9, 100 mM Na formate, and 30% PEG500DM, and incubated for 2-3 weeks in the dark at 20℃. Crystals were observed with a Hirox KH8700 digital microscope.

3-2-6 Sample preparation for LCP-SFX

This experiment was performed by Nureki laboratory membrane group members, including me. 100 μl of LCP pillars with grown C1C2 microcrystals were collected and loaded into a Hamilton syringe and mixed with an equivalent volume of buffer-containing LCP (2:3 ratio of the buffer containing 150 mM NaCl and 50 mM Tris-HCl, pH 8.0, to monoolein). A 10 μl aliquot of liquid paraffin (Wako) was further added to the LCP material and homogenously mixed, to enable smooth flow in the SFX experiment. All of these procedures were performed in the dark under red LED lights (over 600 nm wavelength).

3-2-7 Diffraction experiment at SACLA-FEL

This experiment was performed by Nureki laboratory membrane group members, especially Takanori Nakane. Single-shot XFEL data collection was performed, using

femtosecond X-ray pulses from the SACLA at BL3. The pulse parameters of SACLA were as follows: pulse duration, <10 fs; X-ray energy, 7 keV; energy bandwidth, 33.5013 eV (full width at half-maximum, FWHM); pulse flux, 2.0 x 10^{11} photon/pulse; beam size 1.5 μm (H) × 1.5 μm (W); repetition rate, 30 Hz. The C1C2 crystals were mixed with protein-less LCP and paraffin oil, loaded into an injector with a 75 μm inner diameter nozzle, and set in a diffraction chamber filled with helium gas, in a setup called Diverse Application Platform for Hard X-ray Diffraction in SACLA (DAPHNIS). The flow rate was set to 2.5 μl/min (9.4 mm/s). The diffraction patterns were recorded on a multiport CCD detector with an eight sensor module[112]. The excitation laser pulses were provided at 15 Hz, and the XFEL pulses had a repetition rate of 30 Hz. Each "pump-on" image was followed by "pump-off" images, which were recorded separately. The pump-on images were used to analyze the structural differences, whereas the diffraction data for the dark-state were collected in a separate run, to avoid light contamination.

3-2-8 Pump laser setup

This experiment was performed by Takashi Nomura and Minoru Kubo. To advance the C1C2 samples to the excited state, a 6 ns visible light pump pulse with a wavelength of 470 nm was provided to the samples at Δt = 1 μs, 50 μs, 250 μs, 1 ms, and 4 ms, from an optical parametric oscillator (OPO) (NT230, EKSPLA), which was Q-switched at 15 Hz using a pulse generator (DG645, Stanford Research Systems). The pulse generator was also used to synchronize the pump pulse with the XFEL pulse and control the delay time (Δt) with a timing jitter of < 1 ns. Samples were thus irradiated from both sides of the LCP microjet, a geometry that was chosen to optimize the crystal excitation efficiency. The pump focal size was set to 40 μm (FWHM) and the pump energy was 20 μJ (10 μJ from each direction) at the sample point. The pump beam center was aligned 6 μm upstream from the XFEL spot. The pump light was scattered, as the LCP microjet is semi-transparent. To avoid the interference from the pump scattering, the sample flow rate (9.4 mm/s) was set to be the same as that in the TR-SFX analysis of BR[102], in which each pump-illuminated crystal for the pump-on XFEL images was separated by 630 μm. A portion of the pump beam (5%) was isolated with a beam sampler, and its photodiode-detected signal was used to monitor the laser status and to tag the diffraction image with "pump-on". Since the repetition rate of the pump laser was half of that of the XFEL, the "pump-on" data and the "pump-off" data were collected alternately.

3-2-9 Data processing and structural analysis

This data analysis was performed by Takanori Nakane. Data collection was monitored by a real-time data processing pipeline[113], based on Cheetah[114]. Diffraction images with more than 20 spots were considered as hits and processed in CrystFEL, version 0.6.3[115], with the parameters of hitfinderAlgorithm=6, hitfinderADC=40, hitfinderMinSNR=5. Diffraction spots for indexing were detected by the built-in spot finding algorithms "zaef"[116] or "peakfinder8"[114] in CrystFEL, and indexing was performed with DirAx[117]. Intensities were merged by Monte Carlo integration with the process_hkl command in the CrystFEL suite, with the per-image resolution cutoff (--push-res 1.2). Data collection statistics are summarized in table S1. Difference Fourier electron density maps ($|F_{obs}|^{light}-|F_{obs}|^{dark})\cdot\exp[i\Phi_{calc}]$ were calculated by FFT[118] in the CCP4 suite[119], with phases calculated from the refined dark state model.

3-2-10 Structural refinement

The structure was solved by the molecular replacement method implemented in Phenix Phaser-MR, using the model of C1C2 (PDB: 3UG9). The structure was manually modified to fit into the electron density maps, using the program Coot[67], and then refined with the programs Phenix[66] and Refmac5 in the CCP4 suite[68]. The model structures of the respective delayed time points were generated by real-space refinement against the difference-Fourier maps by COOT, with the restraints of protein geometry and retinal planarity between C_5 to C_{13}. Figures were prepared with Cuemol (http://www.cuemol.org).

3-3 Results and discussion

3-3-1 Time-resolved spectroscopy of C1C2

C1C2 yielded high-density microcrystals that diffracted XFEL to about 2.3 Å at SACLA (Fig. 3-4 a, b). The dark state structure of C1C2 determined at SACLA is almost the same as the previous structure solved by the synchrotron analysis, including the chromophore retinal, the interhelical interactions of the inner and central gates, and the extracellular water access channel in the dark state (Fig. 3-4 c, d, and 3-5)[51]. The C1C2 photocycle was reported in detail recently[108], revealing the different accumulations of the P1 and P2 photo-intermediates, as compared to *Cr*ChR2. Preceding the TR-SFX experiment, the photocycle and ion pore formation processes of C1C2 were investigated. In the flash-photolysis experiments, C1C2 showed similar photo-intermediates as observed in the previous study[108], in detergent micelles or reconstituted lipid membranes (Fig. 3-3 a, b and Fig. 3-6). The results indicate a rapid rise of the 520 nm absorption after photo-excitation, occurring before 10 μsec, which correspond to the formation of the P1

intermediate with isomerized retinal[108,120], and the subsequent increases at 390 nm and 530 nm shows the formation of the P2 and P3 intermediates with a deprotonated and reprotonated retinal Schiff base, respectively (Fig. 3-3 a). The absorption spectra of P1 and P3 resemble each other and cannot be distinguished in C1C2, but the delayed rise of the 530 nm absorption after 360 μsec shows the formation of the P3 intermediate at the later time points. To investigate the correlation between the photocycle and the ion pore formation, the C1C2 photocurrents evoked by flashlight illumination was measured (Fig. 3-3 c and Fig. 3-7). The C1C2 photocurrents are initiated by a fast, inward-directed charge transfer that likely coincides with the retinal Schiff base deprotonation (P1 formation), which has not been fully time-resolved in the whole-cell patch-clamp recordings. Afterward, passive photocurrents rise with a time constant of 70–140 μs (rather faster at acidic pH) and change direction depending on the membrane voltage. The photocurrent remains after reprotonation of the retinal Schiff base and declines in a biexponential manner, with two voltage-dependent time constants of 8 – 40 ms and 60 – 130 ms and a kinetic amplitude ratio that depends on the pH, which is not in accordance with the formation of either the P2 or P3 intermediate. The absorption spectrum of ChR is mainly dependent on the microenvironment of the chromophore retinal, especially on the Schiff base environment[121], and the ion pore structure is not exactly reflected in the absorption spectrum change. As recently shown for *Cr*ChR2[98], C1C2 channel opening also takes place only after deprotonation of the retinal Schiff base, during the P2 intermediate.

To determine the time points for the TR-SFX study, the photocycle of C1C2 in the Lipidic Cubic Phase (LCP) crystals was measured. The flashlight illumination induced a rapid elevation at 530 nm, confirming retinal isomerization (P1 formation) (Fig. 3-3 d and Fig. 3-8 a, c). The elevation of the 390 nm absorption, which is most prominent in 2.1 to 21 ms, represented the P2 formation, but the subsequent increase at the 530 nm absorption was not observed in the crystal (Fig. 3-3 d and 3-6 and 3-8 a, c). From these results, it is suggested that the transition from P2 to P3 is hindered in the crystal, although the C1C2 crystal has minimal interactions at the extra-membrane region (Fig. 3-9). Nonetheless, the accumulation of the P2 intermediate is more prominent in the crystals, as the spectral increase at 390 nm is relatively higher, as compared to the similar increase detected in micelles and reconstituted membranes (Fig. 3-3 a, d and Fig. 3-6, 3-8 b, d). In addition, the flash photo-activation experiment using HEK cells showed that the photocurrent increased up to about 100 - 1000 μsec, regardless of pH, which corresponds to the late P2 intermediate (Fig. 3-3 c and Fig. 3-7), in a good agreement with the previous studies in ChR2[98,122]. Therefore, the author selected the time points corresponding to the P1 to P2 transition in the crystals for the TR-SFX study, to understand the detailed

mechanism of the light-dependent channel pore opening in ChR.

3-3-2 Structural changes in LCP

The LCP matrix containing C1C2 microcrystals was introduced to the XFEL chamber in a continuous flow. Since the crystallized sample was swollen and almost in the liquid sponge phase, the author added paraffin and solid LCP matrix to enable stable and constant sample flow to the FEL beam (detailed in Methods). The diffraction images were collected at 30 Hz, with the 470 nm pump-pulse laser at 15 Hz and the delayed time points at 1 μs, 50 μs, 250 μs, 1 ms, and 4 ms (Fig. 3-10 a, b and Table 1). The absence of light contamination was checked by the second dark dataset, obtained with a 10 Hz pump laser pulse (Fig. 3-10 c, d). The difference-Fourier maps were calculated at 2.5 Å for each delayed time point, with the dark state SFX structure as the reference, and they clearly revealed the structural changes in the protein core region of C1C2 (Figs. 3-11, 3-12). Due to the low quantum efficiency of the retinal isomerization, which is estimated as only about 30% in C1C2[108], the author manually built a model onto the observed peaks in the difference maps. Since the retinal isomerization reaction is generally completed within a few picoseconds[108,123,124], the observed changes correspond to the events following retinal isomerization.

Isomerization of the retinal induces conformational changes of the retinal-attached residue, K296, and TM7 (Fig. 3-13 left panels). The positive densities along K296 suggest its downward shift (toward the extracellular side), which is detected from 1 μs and becomes most prominent at 4 msec (Fig. 3-13 right panels). In accordance with this shift, positive and negative difference densities are observed around the proximal residues in TM7, such as W299, indicating an overall downward shift of the middle portion of TM7. The similar downward shift of TM7 (Helix G) was the most distinct feature in the L-like intermediate of bacteriorhodopsin, observed in both the cold-trapped synchrotron structure[125] and the recent TR-SFX study[102]. In the TR-SFX experiment of BR, the primary retinal isomerization reaction induced local distortion around the C13-C14 double bond of the retinal, which was subsequently propagated as conformational changes in other protein regions, including the downward shift of TM7. Therefore, the retinal-attached residue in C1C2 probably undergoes similar conformational changes, although the primary retinal isomerization was not visualized, due to the limited resolution of the current TR-SFX experiment. Notably, at 50 μsec the author observed positive and negative difference densities at the putative internal proton acceptor residue, D292 (Fig. 3-13, left panels), indicating a slight downward shift of this residue, which might be associated with the proton accepting reaction.

3-3-3 Retinal kins and outward shift of TM3

The most prominent change occurs in TM3 (Fig. 3-13, right panels). A strong negative density appears at C167, accompanied by a complementary positive density at the distal site from the retinal, suggesting an outward shift of C167. In addition, a strong positive density appears near P168 on the outside of the TM3 segment, which indicates an outward shift of the cytoplasmic segment of TM3, originating at the helix kink at the P168 residue. Along with these changes, negative and positive densities appear at the C13 methyl group and on the lateral side of the polyene chain of the retinal, respectively. This kink and lateral shift of the retinal allow lateral movement of TM6 as well as TM3 (Fig. 3-13, right panels). The current difference Fourier map is in excellent agreement with the recent MD simulation combined with QM/MM calculations[126], in which the retinal conformation around the C13-C14 double bond alters upon the deprotonation of the Schiff base, probably due to the destabilized resonance structure of the polyene chain, and adopts a kinked conformation toward TM3 (Fig. 3-14). Together, the sequential changes in the difference-Fourier maps suggest that the retinal kink occurs, followed by the consequent outward shift of TM3. Consistently, the positive/negative peaks at the retinal appear slightly earlier, whereas the change in TM3 becomes slower and reaches the maximum at the later time points of 1 ms and 4 ms (Fig. 3-14).

3-3-4 Channel pore gating in ChR

The current TR-SFX experiment revealed two critical conformational changes occurring early in the photocycle process: the outward shift of TM3 and the downward shift of TM7, both of which constitute the gate constriction sites along the ion permeation pathway in the dark state (Fig. 3-4 c, d). TM7 constitutes the “central gate”, in which N297 forms hydrogen bond interactions with S102 (TM2) and E129 (TM3). Therefore, the TM7 shift, as well as the outward shift of D292 upon proton acceptance, should lead to the rearrangement of the central gate residues. While the similar TM7 shift was also observed in other microbial rhodopsins including BR, the retinal kink and the consequent outward shift of TM3 are unique features only observed in the channelrhodopsin. The intracellular end of TM3 constitutes the “inner-gate”, in which H173 forms ionic interactions with R307 in TM7 and E121 and E122 in TM2. The recent MD simulation showed a similar retinal kink and subsequent water influx from the intracellular side (Fig. 3-14)[126]. Therefore, the conformational change in the middle of TM3 might propagate to the intracellular segment and induce the opening of the inner gate. Previous 2D crystallographic studies of the *Cr*ChR2 C128T mutant (corresponding to C167 in C1C2

(Fig. 3-2) suggested the rearrangements of TM2, 6, and 7 in the open conformation, induced by the stationary light illumination[99,100]. These conformational changes are partly consistent with the current TR-SFX analysis. However, the TM3 shift is only observed in the current study, indicating the critical role of the Cys residue in the TM3 shift. The movement of TM7, on the other hand, is similarly observed in both experiments, although to different degrees. Therefore, the author proposed that the conformational changes in TM7 and TM3 are the two important triggers that cooperatively induce channel opening by eliciting sequential conformational changes in the surrounding helices, such as TM2 and TM6 (Fig. 3-15), as observed in the "open" conformation of the SFO mutant of *Cr*ChRs[100]. This model is also in good agreement with the results of the vibrational spectroscopic study showing the two-phase helix hydration occurring during the early and late stages of the P2 intermediate, in which the latter leads to the fully-open channel pore[127]. Furthermore, site-directed labeling with infrared sensitive, unnatural amino acids subsequently showed that more specific hydration changes in the intracellular gate are correlated with channel opening[128].

3-4 Conclusion

In summary, the TR-SFX experiment has revealed two critical conformational changes in TM7 and TM3 that occur during the early part of the photocycle, and these triggers would induce water and proton influx and subsequent pore dilation, although only slight structural perturbations in the gate constrictions were observed in the current study, as they were probably affected by the crystal packing interactions (Fig. 3-16).

The current results also highlighted the functional coupling of the DC-pair and the TM3 shift. A recent MD simulation demonstrated the hydrogen bonding interactions between the deprotonated Schiff base and the hydroxyl group of Thr166, located beside the C167 residue[126], which are likely to affect the retinal conformation. The same threonine is highly conserved among microbial rhodopsins, and in *Cr*ChR2 it was also proposed to couple the protonation changes in the counterion region to the hydrogen bonding changes in the DC-pair and the conformational changes of TM3[129]. Together, the hydrogen-bonding network beside the retinal, involving the DC-pair, may affect the retinal conformation after isomerization, in good agreement with the experimental evidence that the residues lining the retinal pocket affect the channel kinetics[130]. These results would pave the way for the development of novel optogenetic tools with different kinetics.

3-5 Figures and table associated with Chapter 3

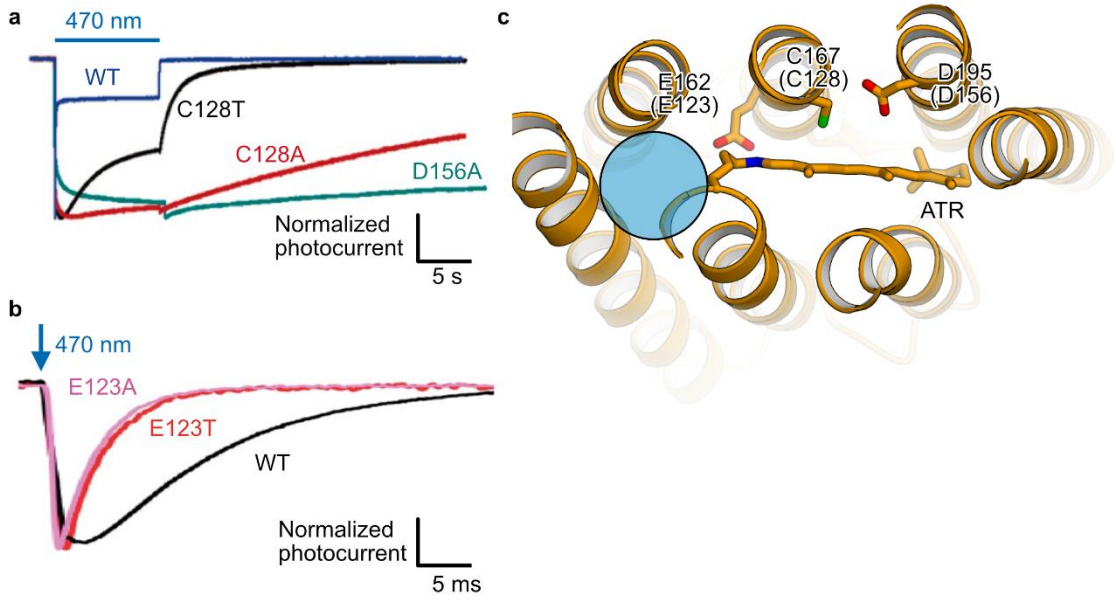

Fig. 3-1 Kinetics mutants and an ion pore of channelrhodopsin

a, ChR mutants that show a slow channel kinetics[84,92,131]. **b**, ChR mutants that show a fast channel kinetics. **c**, ChR structure that represents the location of mutants and ion-pore (blue circle.)

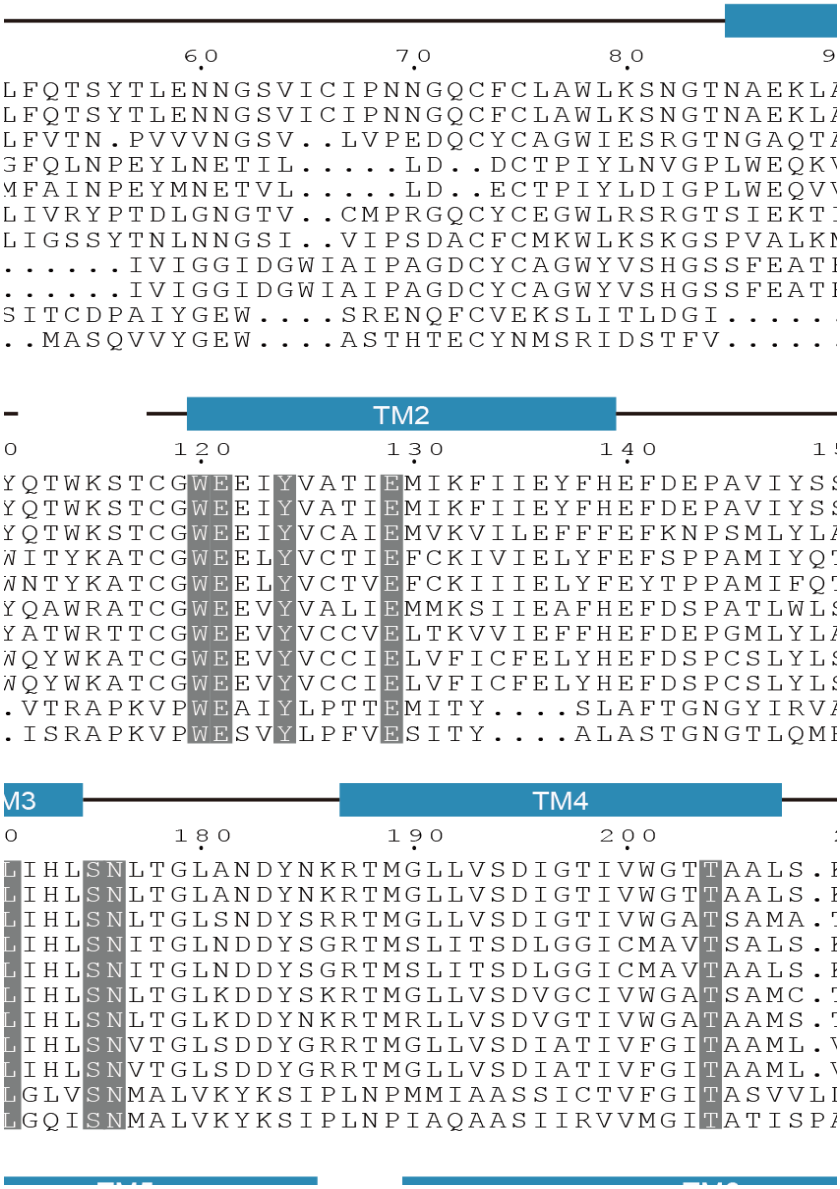

Fig. 3-2 Sequence alignment of channelrhodopsin variants.

Amino acid sequences of major variants of channelrhodopsins are shown. Conserved residues are highlighted in gray and red. The residues in red indicate important residues for the initial trigger revealed by the current study.

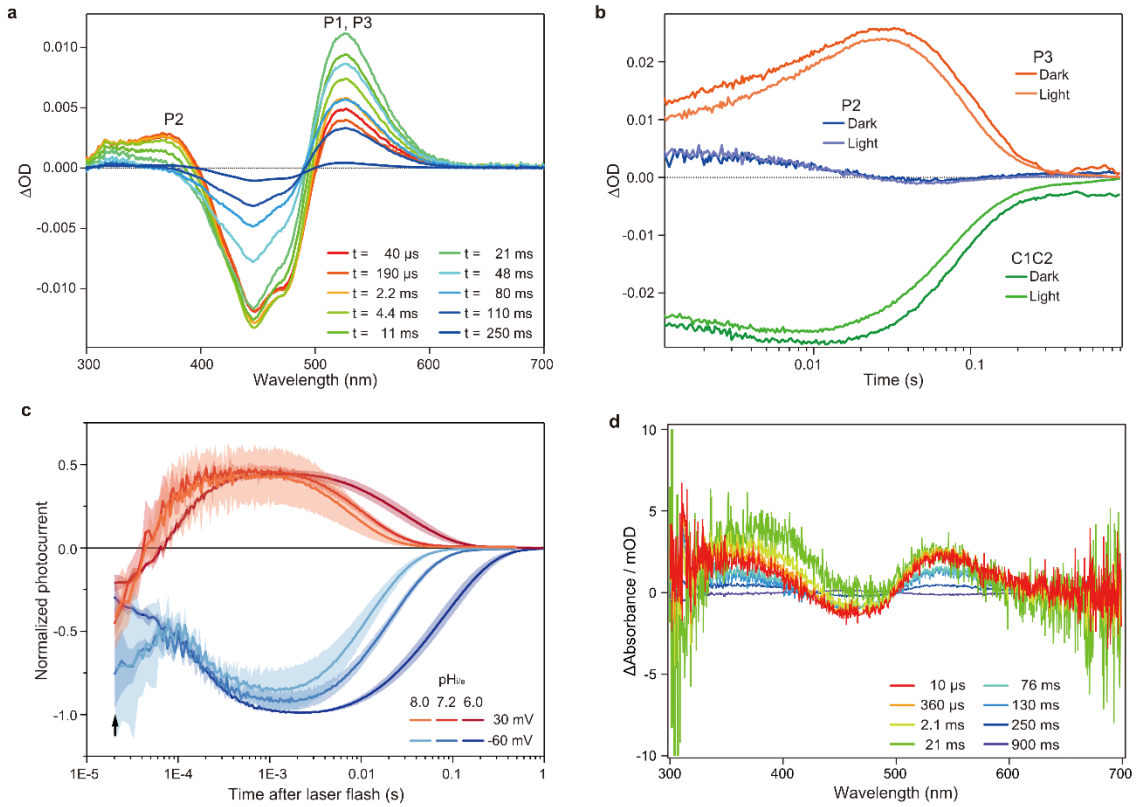

Fig. 3-3 Flash photolysis and flash photo activation measurement of C1C2.

a, Transient absorption spectra of C1C2 reconstituted in POPE/POPG (protein/lipid molar ratio=1/50), 150 mM NaCl, 50 mM Tris-HCl (pH 8.0), 5% glycerol, and 0.01% CHS. This experiment was performed by Keiichi Inoue. **b**, Time trace of absorption changes of C1C2 reconstituted in POPE/POPG, at 445 (green), 375 (blue), and 520 nm (red) probe wavelengths. This experiment was performed by Keiichi Inoue. **c**, Normalized, log-binned, and averaged photocurrents of the C1C2 protein (mean ± SEM, n = 3 5). The black arrow indicates the inward-directed current caused by retinal Schiff base deprotonation. These results were obtained from C1C2 that was expressed in HEK cells. This experiment was performed by Johannes Vierock. **d,** Transient difference absorption spectra recorded from the multiple C1C2 crystals. Each time-resolved spectrum was averaged over 21 crystal data sets. The time evolution is indicated from red to purple. This experiment was performed by Takashi Nomura and Minoru Kubo.

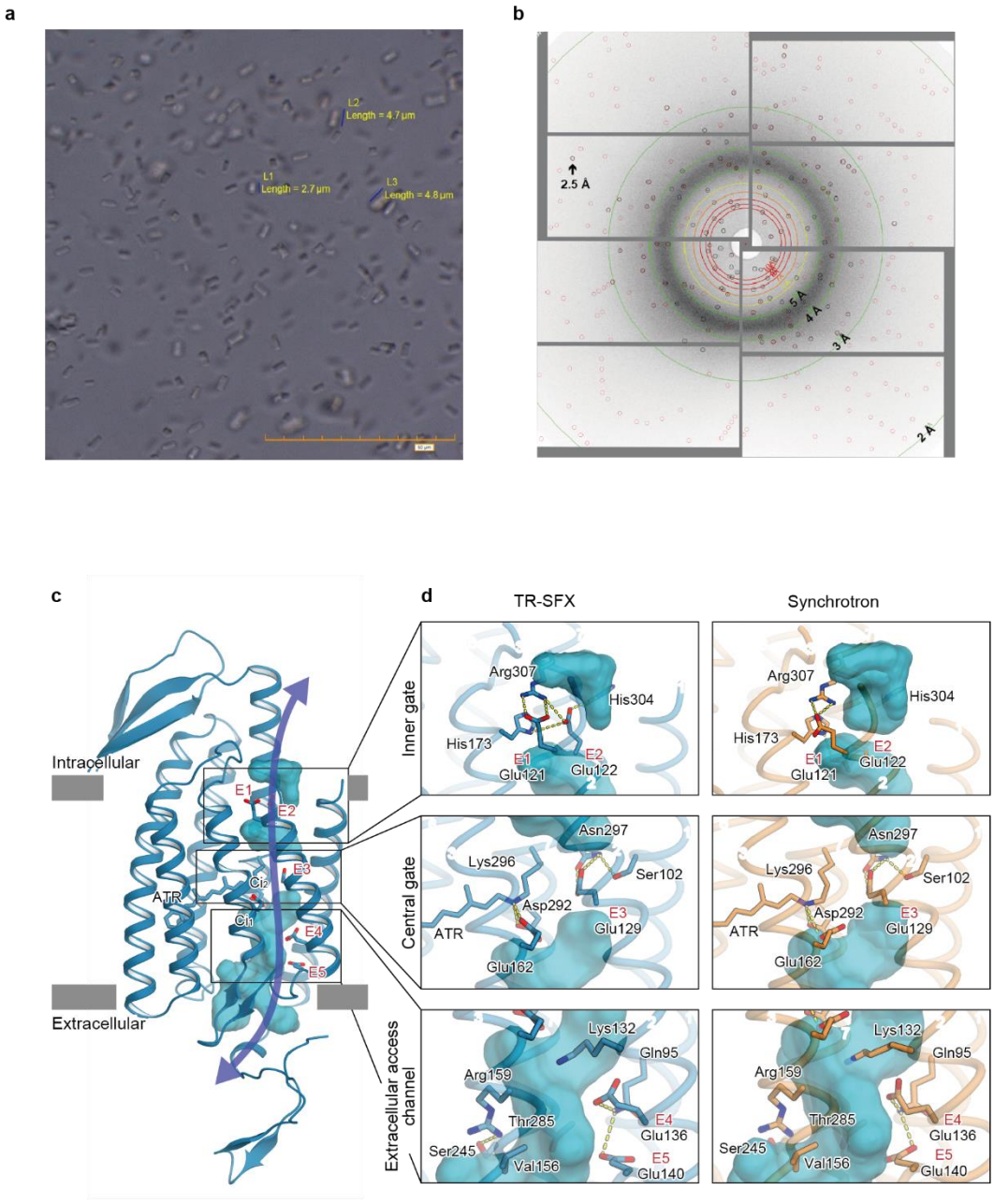

Fig. 3-4 Microcrystals for SFX experiment.

a, LCP crystals of C1C2 optimized for the TR-SFX experiments. The orange scale bar on the lower left indicates 50 µm, with 5 µm sub-scaling lines. The size of the crystals ranged from 2–5 µm. **b**, A diffraction image from a C1C2 crystal, obtained with a single SACLA-XFEL pulse. **c**, The structure of dark state C1C2 is determined by serial femtosecond crystallography. A water accessible cavity is illustrated, with the putative ion pathway indicated by an arrow. The five glutamic acid residues lining the ion pore (E1–5) and the two counterion residues (C_{i1} and C_{i2}) are indicated by sticks, and the three constriction

sites, the inner, central, and outer gates are enclosed in boxes. **d**, Comparisons of the constriction sites of the TR-SFX structure (left panels) and the synchrotron structure (right panels; PDB code 3UG9) of C1C2, for the inner (upper panels), central (middle panels), and outer (lower panels) gates. The constituent residues are shown as sticks, and the TM helix number is indicated on each helix.

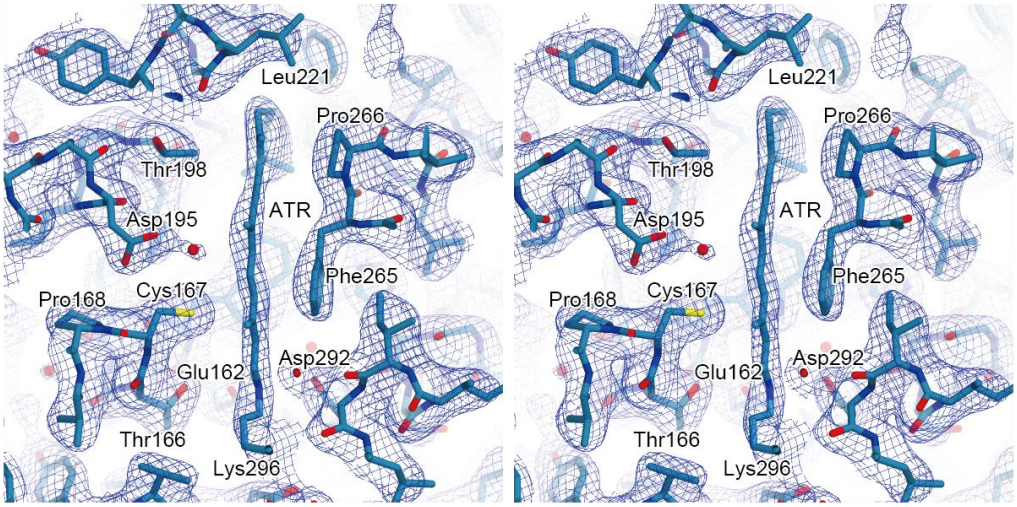

Fig. 3-5 Electron density of retinal.

A stereoview of the $2F_o$-F_c electron density map for the retinal binding pocket, shown as a mesh representation contoured at 0.9σ. The all-*trans* retinal (ATR) and the surrounding residues are indicated by sticks. The red spheres indicate water molecules.

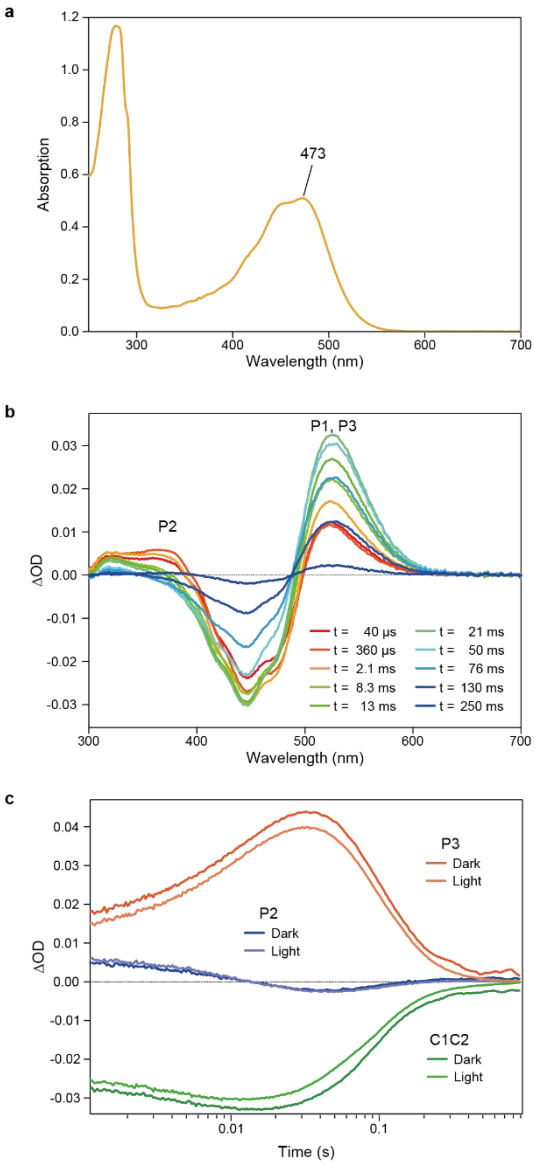

Fig. 3-6 Flash photolysis measurements of C1C2 solution in DDM.

a, Absorption spectra of purified C1C2 solubilized in DDM detergent. **b**, Transient absorption spectra of C1C2 in DDM. **c**, Time traces of absorption changes of C1C2 in DDM at 445 (green), 375 (blue), and 520 nm (red) probe wavelengths. These experiments were performed by Keiichi Inoue.

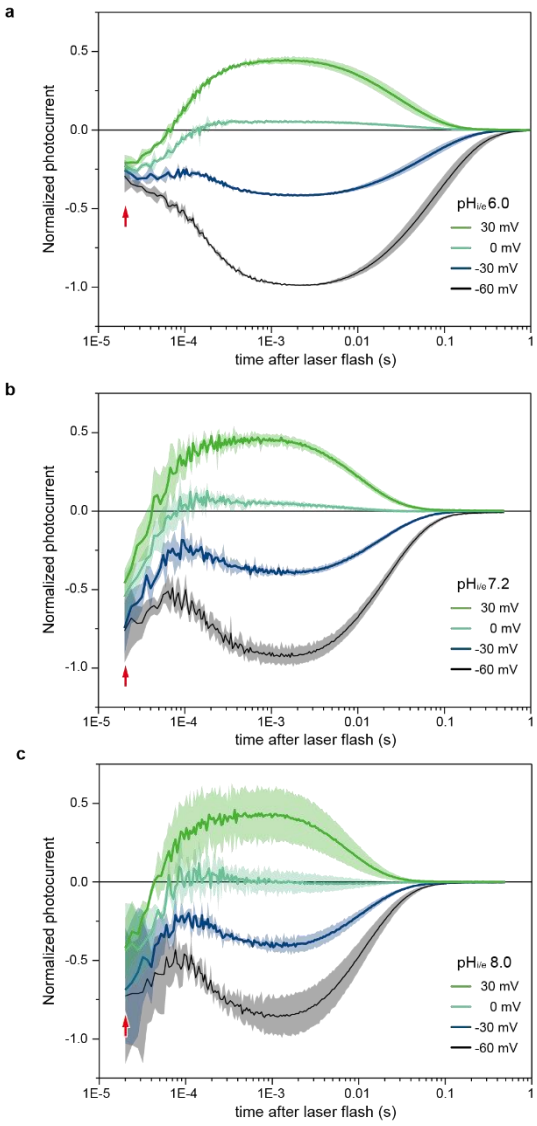

Fig. 3-7 Voltage-clamp recordings in HEK293 cells of photocurrents from C1C2. Normalized, log-binned, and averaged photocurrents of the C1C2 protein (mean ± SEM, n = 3 5) with $pH_{i/e}$ 6.0 (a), 7.2 (b), and 8.0 (c). Red arrows indicate the inward-directed current caused by retinal Schiff base deprotonation. These experiments were performed by Johannes Vierock.

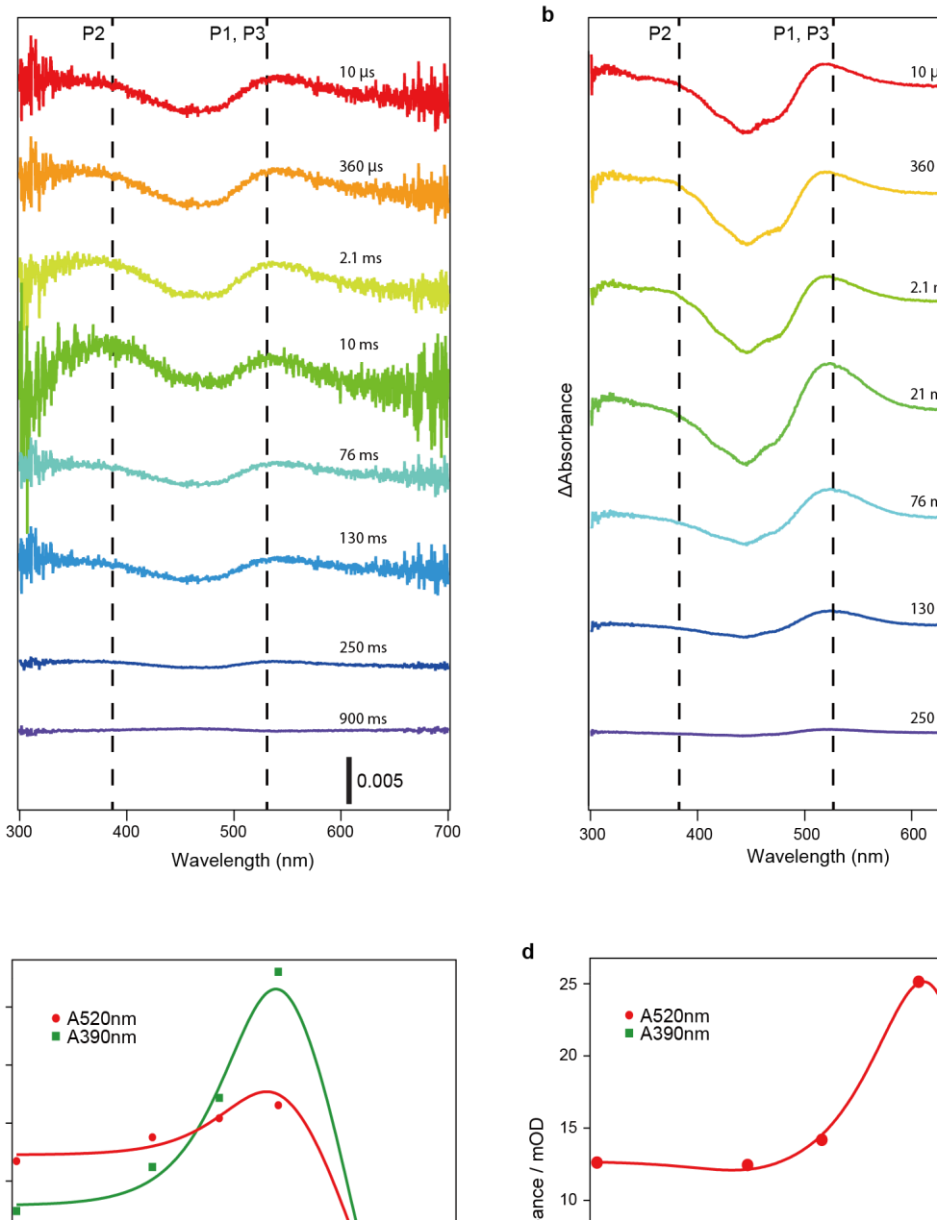

Fig. 3-8 Flash photolysis measurements of C1C2 crystals and C1C2 solution in DDM.

a-b, Transient difference absorption spectra were recorded from the C1C2 crystals (a) and C1C2 solution in DDM (b). **c-d**, The time evolution is indicated from red to blue. Dashed lines indicate the wavelengths of maximum absorption of the reaction intermediates. These experiments and data analysis were performed by Takashi Nomura and Minoru Kubo.

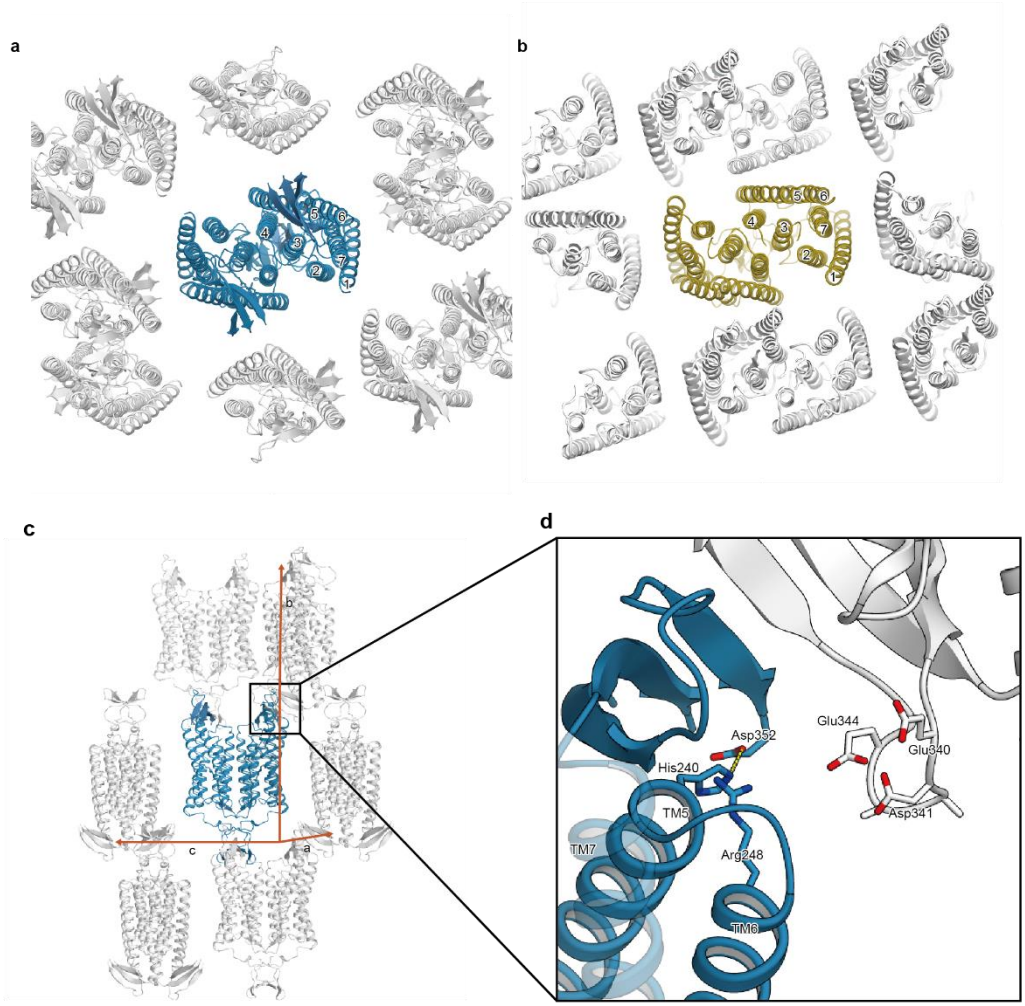

Fig. 3-9 Comparison of the crystal packing between C1C2 and *Cr*ChR2.
a-b, Comparison of the crystal packing between C1C2 (PDB: 3UG9) (a) and *Cr*ChR2 (PDB: 6EID) (b). The crystal packing of C1C2 shows minimal packing interactions, as compared to the *Cr*ChR2 crystal packing. **c**, The C1C2 molecules in the crystals are shown in ribbons, viewed from within the LCP crystal layer. **d**, The residues involved in the crystal packing interactions are shown in sticks.

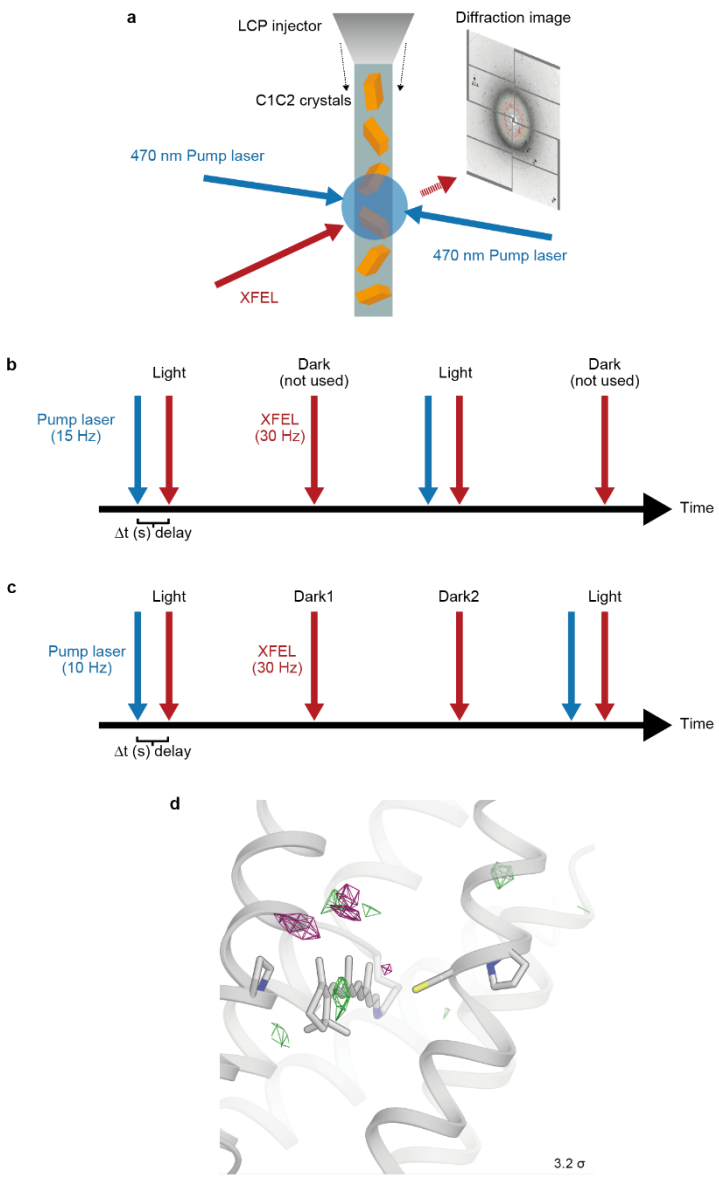

Fig. 3-10 Schematic model of the time-resolved serial femtosecond crystallography setup.

a, The lipidic cubic phase (LCP) microjet continuously transports microcrystals across the focused XFEL beam. X-ray diffraction is recorded on a detector for each XFEL exposure. A blue ns laser is used to photo-activate C1C2 microcrystals prior to the arrival of an XFEL pulse. **b-c,** Data collection sequence illustrating how X-ray diffraction data were collected at 30 Hz from photoactivated (blue laser flash, 15 Hz (b) and 10 Hz (c), respectively) and resting (no laser flash) phases in an interleaved fashion. Part of the TR-SFX was recorded with a 10 Hz laser flash to check for light-contamination. The Δt represents the time delay of XFEL at 1 μs, 50 μs, 250 μs, 1 ms,

and 4 ms. **d**, Fourier difference map of dark2 from the “dark” dataset, which was separately collected (Methods).

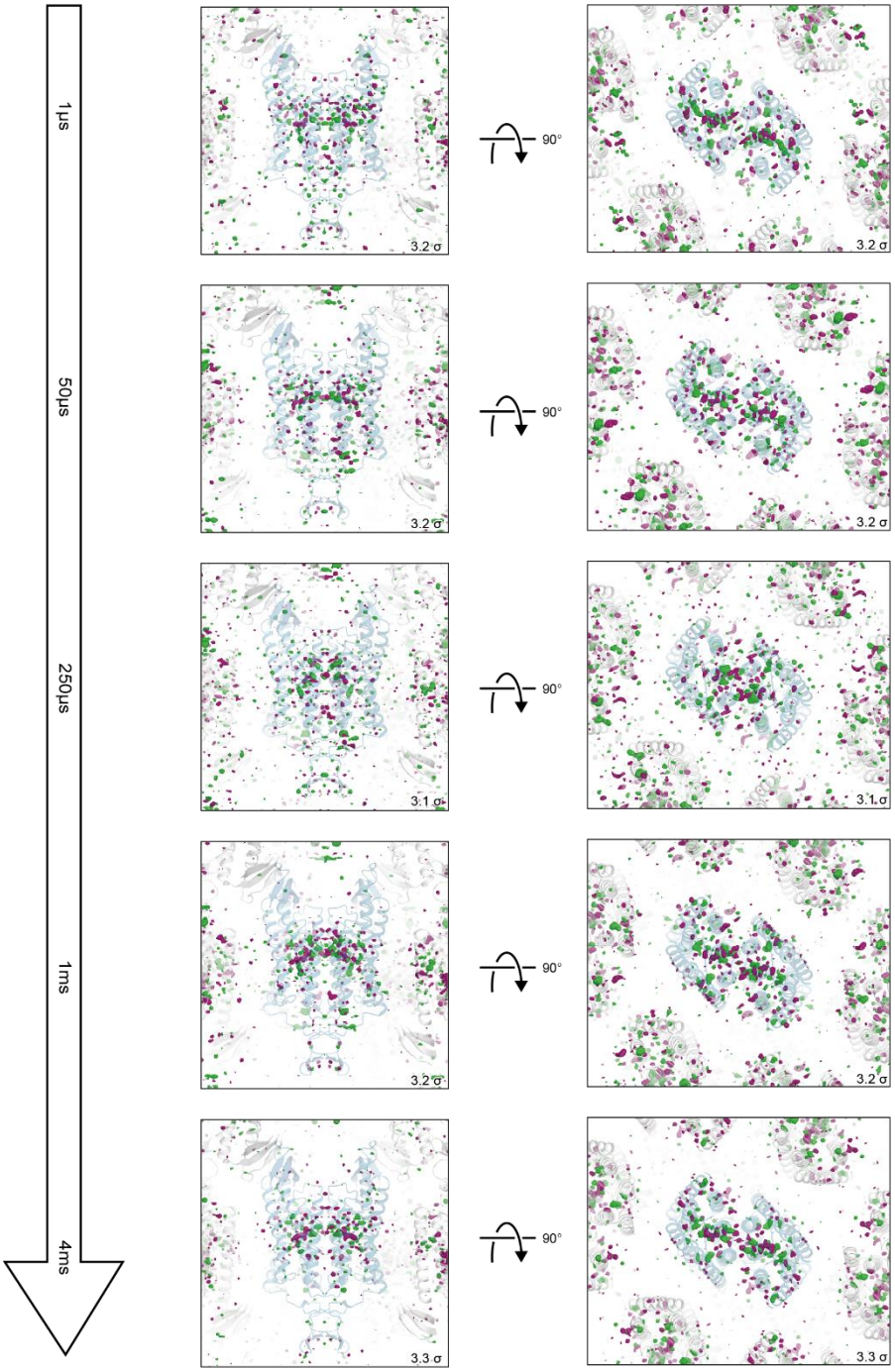

Fig. 3-11 Overview of the $|F_{obs}|^{light}$ - $|F_{obs}|^{dark}$ difference Fourier electron density maps for five time-points.

Green represents positive difference electron density (contoured at +3.1 ~ 3.3σ, where sigma represents the root mean square electron density of the unit cell) and purple represents negative difference electron density (contoured at -3.1 ~ -3.3σ). The initial-state C1C2 structure was used for the phases in calculating these difference Fourier maps and is shown in blue. Significant density changes were only observed in the protein regions.

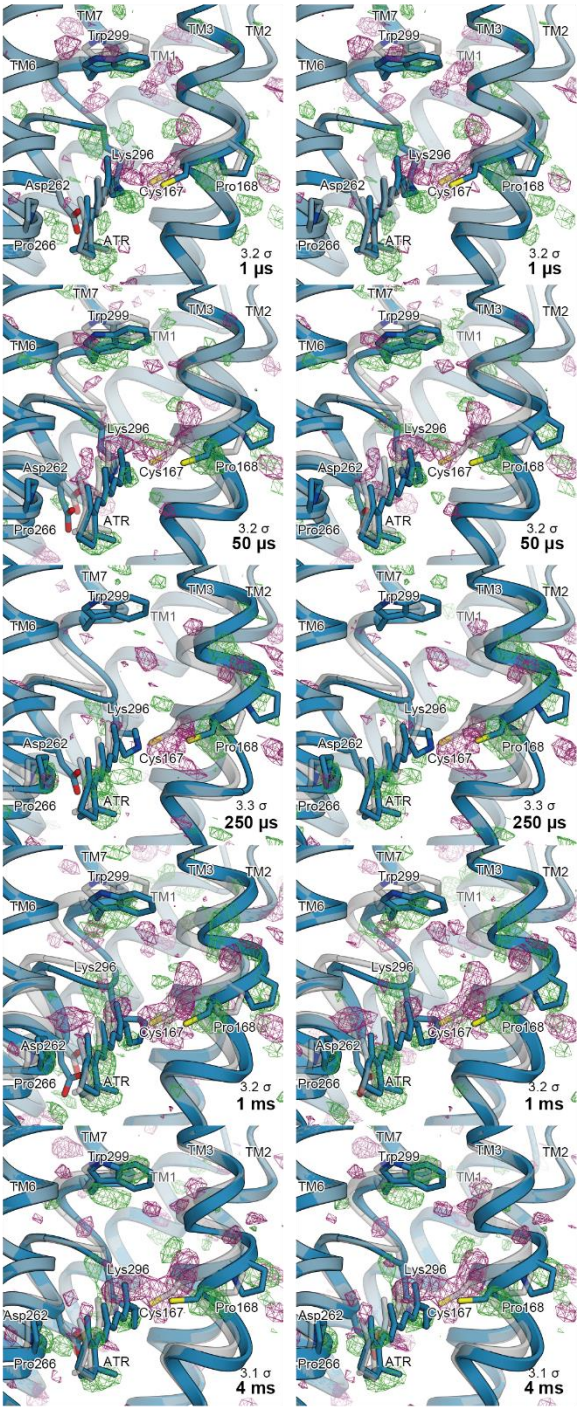

Fig. 3-12 Stereoviews of the difference Fourier electron density maps and structural changes.

Stereoviews of the $|F_{obs}|^{light}$ - $|F_{obs}|^{dark}$ difference Fourier electron density maps and the structural changes of C1C2. Each time point is indicated in the respective maps. Green represents positive difference electron density (contoured at +3.1 ~ 3.3σ, where sigma represents the root mean square electron density of the unit cell) and purple represents

negative difference electron density (contoured at -3.1 ~ -3.3σ). The initial-state C1C2 structure was used for the phases in calculating these difference Fourier maps and is shown in blue.

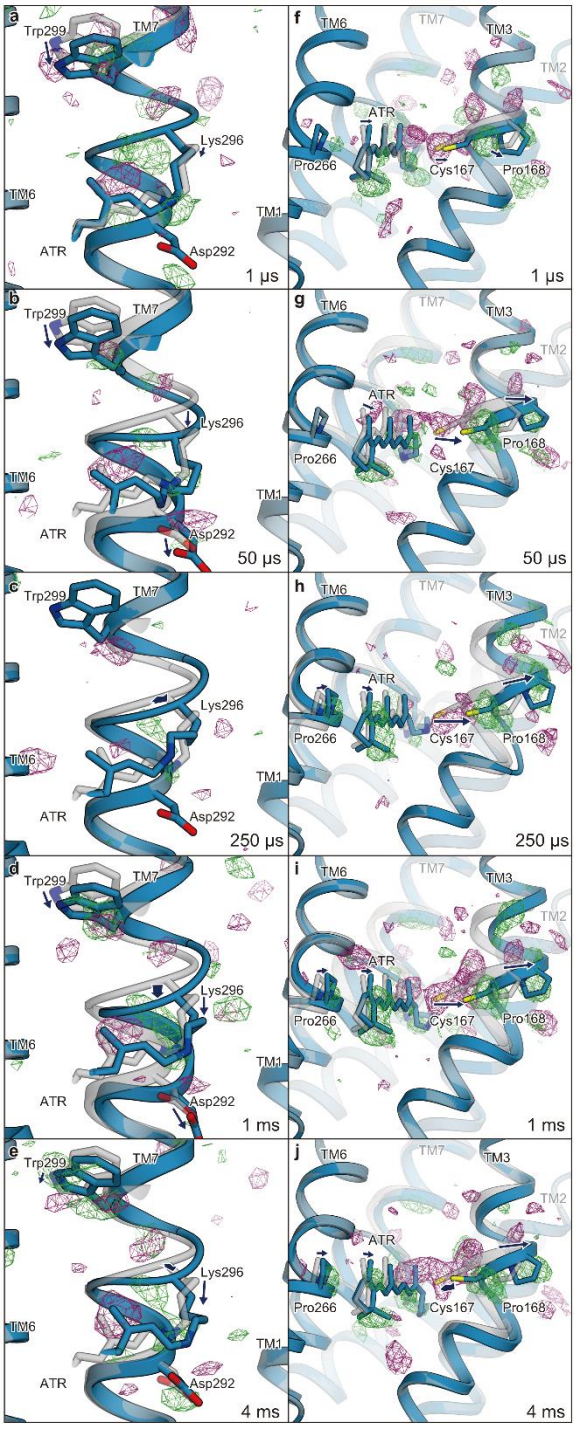

Fig. 3-13 Difference Fourier electron density map and structural changes around

TM7 and TM3.

Views of the $|F_{obs}|^{light}$ - $|F_{obs}|^{dark}$ difference Fourier electron density maps and the structural changes around TM7 (a–e) and TM3 (f–j) for 1 μs (a, f), 50 μs (b, g), 250 μs (c, h), 1 ms (d, i), and 4 ms (e, j). Green and purple meshes indicate positive and negative difference electron densities, respectively (contoured at ±3.1 ~ 3.3σ, see also Sup. Fig. 10). The difference Fourier maps were calculated by using the phases from the coordinates of the dark-adapted C1C2 structure (gray). Paired negative and positive difference electron densities indicate the downward shift of TM7 and the outward shift of TM3. The structural model (blue) derived from the $|F_{obs}|^{light}$ - $|F_{obs}|^{dark}$ positive difference electron density is superimposed upon the dark-adapted C1C2 structure. Movements of the residues and the TM helices are indicated by arrows. Probably due to the variations in the crystal quality (Table 1), the difference density in the 250 μs time-delay seems rather weak.

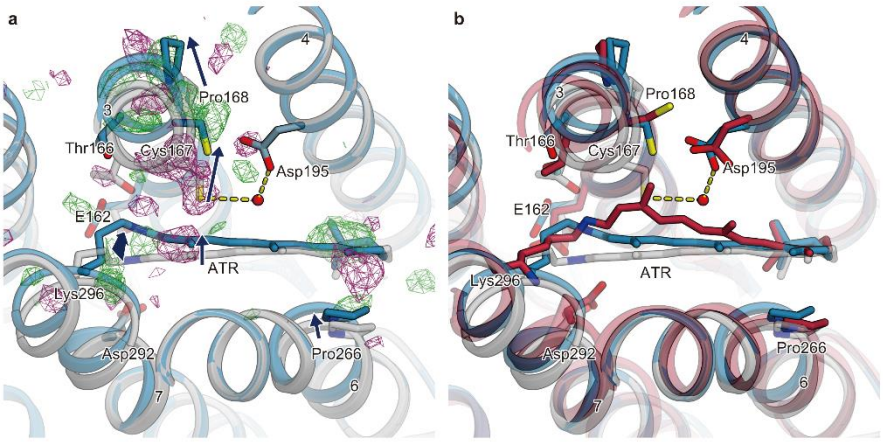

Fig. 3-14 Conformational change of retinal and comparison with QM/MM model.

a, $|F_{obs}|^{light}$ - $|F_{obs}|^{dark}$ difference Fourier electron density map and the structural changes around the retinal. Green and purple meshes indicate positive and negative difference electron densities, respectively. The structural model (blue) derived from the 1 ms $|F_{obs}|^{light}$ - $|F_{obs}|^{dark}$ positive difference electron density is superimposed upon the initial-state C1C2 model. Movements of residues or TM helices are indicated by arrows. **b**, The retinal pocket of dark-adapted C1C2 (gray), the model at the 1 ms delayed-time point (blue), and the model at 400 ns of the QM/MM simulation[132] (red) are superimposed together.

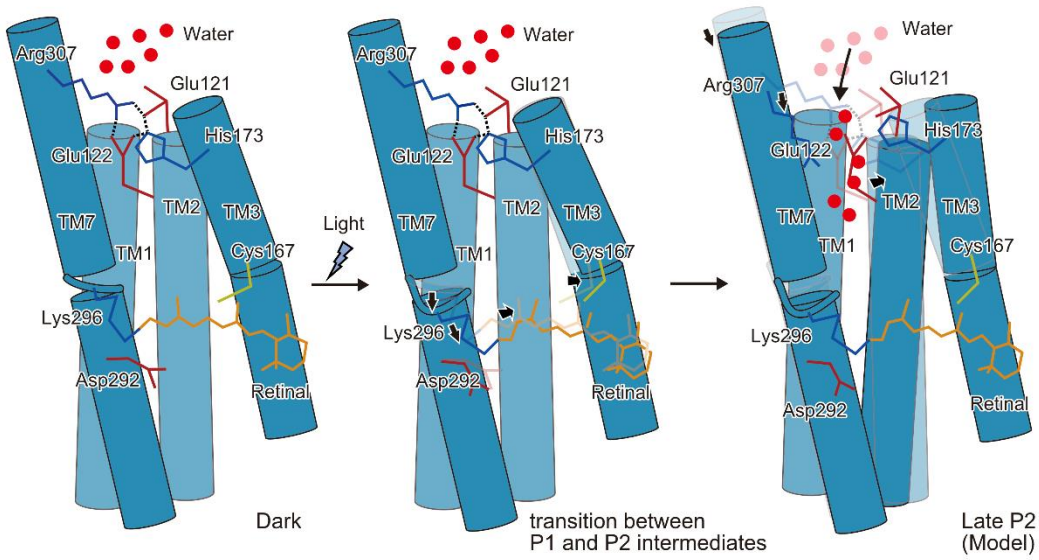

Fig. 3-15 Schematic model of the C1C2 channel opening.

The inner gate formed by E121, E122, H173, and R307 prevents water influx in the initial dark-adapted state. After the retinal isomerization reaction, the retinal twists and shifts toward C167 and induce an outward shift of TM3, originating at the kink introduced by P168. Isomerization of the retinal also induces a downward shift of the middle portion of TM7, especially at the retinal-attached residue, K296 (Transition between the P1 and P2 intermediates). These movements are likely to induce water influx, by destabilizing the intracellular constriction and further induces rearrangement of the surrounding helices (Open model).

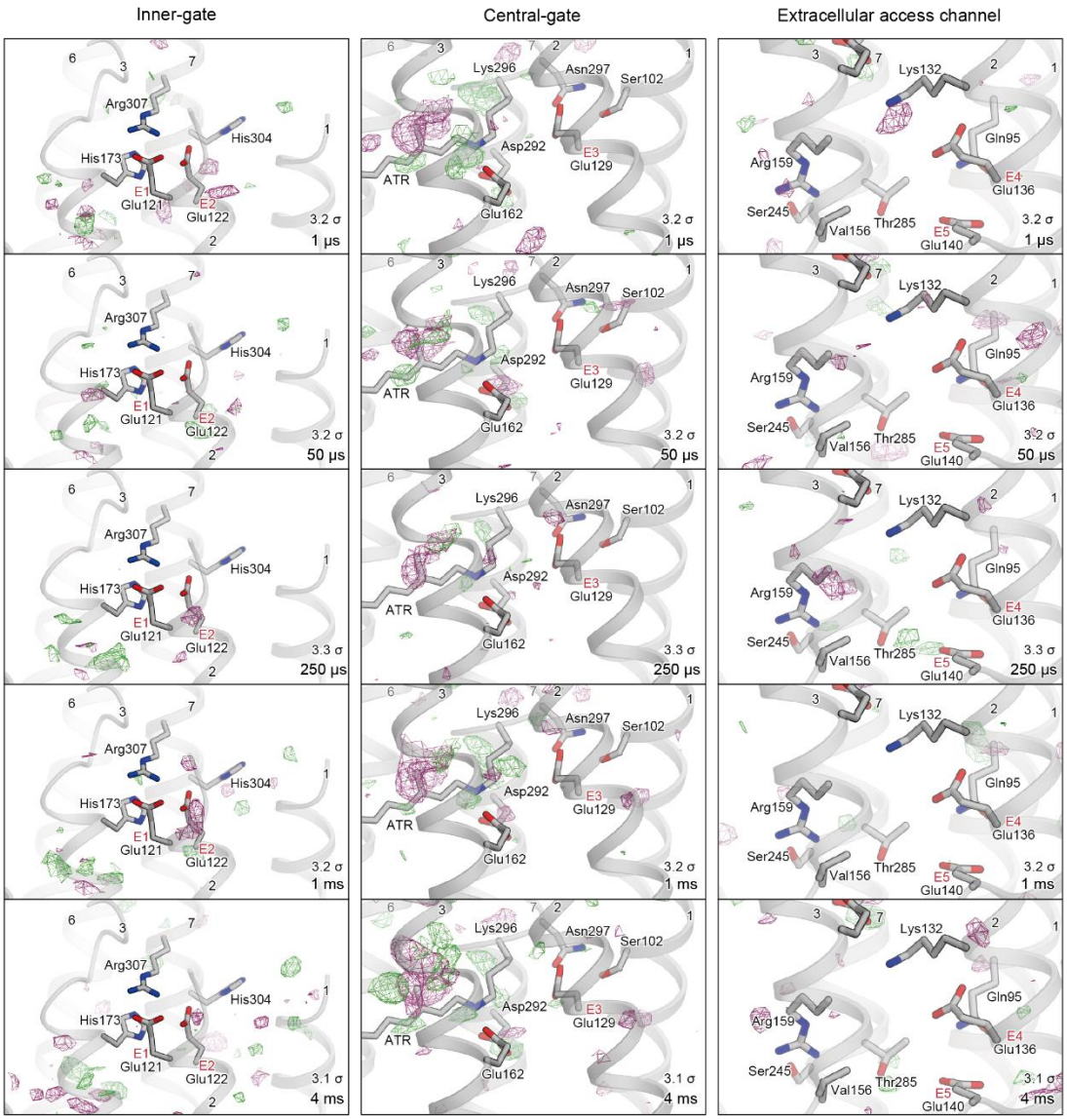

Fig. 3-16 Difference Fourier maps along the putative ion pore.

Difference maps of different time delays are shown for the inner-gate (left), central-gate (middle), and extracellular water access channel (right). Each time point and contour level is indicated in the respective maps.

Table 1. Crystallographic data and refinement statistics.

	Dark	Dark2 (10 Hz)	1 us	50 us	250 us	1 ms	4 ms
Data collection							
Wavelength (Å)				1.77			
No. of collected images	660157	37513	148290	131721	104777	151127	189568
No. of hit images	68058	5727	18005	22999	21516	23512	28997
No. of indexed images	62218	5356	16924	21129	16442	22156	24015
Space group				$C222_1$			
Cell dimensions							
a, *b*, *c* (Å)				61.8, 142.2, 94.7			
a, b, g (°)				90, 90, 90			
Resolution (Å)	15-2.3 (2.34-2.30)	15-2.5 (2.54-2.50)	15-2.5 (2.54-2.50)	15-2.5 (2.54-2.50)	15-2.5 (2.54-2.50)	15-2.5 (2.54-2.50)	15-2.5 (2.54-2.50)
*R*split	0.061 (0.60)	0.21 (0.90)	0.11 (0.58)	0.095 (0.66)	0.13 (0.89)	0.096 (0.51)	0.095 (0.64)
I / s*I*	9.62 (1.55)	3.68 (1.24)	6.42 (1.66)	7.16 (1.63)	5.38 (1.16)	7.42 (2.00)	6.94 (1.56)
Completeness (%)	100 (100)	100 (100)	100 (100)	100 (100)	100 (100)	100 (100)	100 (100)
Redundancy	553 (139)	43.3 (20.7)	140 (60.2)	155 (66.7)	119 (39.2)	180 (83.8)	172 (63.4)
CC1/2	1.00 (0.84)	0.94 (0.52)	0.98 (0.80)	0.99 (0.78)	0.98 (0.64)	0.99 (0.82)	0.99 (0.79)
Refinement							
Resolution (Å)	47.350 - 2.300 (2.382 - 2.300)						
R_{work} / R_{free}	0.1967 / 0.2277 (0.2897) / (0.3419)						
No. atoms							
Protein	2337						
Ligand/ion	154						
Water	38						
B-factors							
Protein	74.4						
Ligand/ion	101.6						
Water	69.3						
R.m.s. deviations							
Bond lengths (Å)	0.0031						
Bond angles (°)	0.69						
Ramachandran plot							
Favored	97.91						
allowed	2.09						
outlier	0.00						

Chapter4: General discussion

4-1 Overview of this thesis

In this thesis, the crystal structure of dark state Chrimson and the structural changes of C1C2 captured by TR-SFX are reported. The Chrimson structure revealed the molecular mechanisms of ChR absorption peak shift and the structural information contributed to design a more red-shifted ChR variant, ChrimsonSA. The observed structural changes of C1C2 highlighted the functional coupling of the DC-pair and the TM3 shift and revealed a part of molecular mechanisms of ChR channel gating.

4-2 Future perspective

ChR will be continually studied as a main tool of optogenetics and various functional ChRs will be required. Especially, red-shifted ChR is quite important for optogenetics development as longer-wavelength light allows deeper tissue penetration and further study of ChR are needed to elucidate the detailed molecular mechanism of ChR absorption peak shift. Recently, some alternative approaches have been applied to design more red-shifted microbial rhodopsin[133–136] For example, a machine-learning-based data-driven approach was applied[133]. In this study, about 700 rhodopsin proteins were used as the training dataset and the authors succeeded in identifying some amino acid residues associating with the absorption peak shift of rhodopsin protein. These amino acid residues are located around the retinal and these results are consistent with this thesis results. Another example is that synthetic retinal analogs were combined with rhodopsins and this strategy successfully shifted the rhodopsin absorption peak shift[135]. Combining the findings of this thesis and these new approaches could be helpful for further development of red-shifted ChR.

In addition to red-shift variants, channel kinetics variants are also required as an optogenetics tool. The results of TR-SFX experiments revealed a part of molecular mechanisms about channel kinetics and further mutation analysis was performed to identify the key residues that play an important role in channel kinetics. From the results of TR-SFX experiments, it was suggested that the TM3 are kinked to the dimer interface. Based on this result, hydrophobic residues located on the dimer interface of TM3 are considered to interact with each other at the channel opening (Fig. 4-1). Therefore it was suggested that the mutation of these residues could affect the channel kinetics. Mutation

analysis of these residues was performed and the mutations of I172 altered the channel kinetics (Fig. 4-2). It is under consideration whether this mutation could be used as an optogenetic tool.

As mentioned above, the TR-SFX experiment of C1C2 revealed the conformational changes of the initial open state and the result of TR-SFX was contributed to design some channel kinetics mutants. However, the author could not observe the fully open state structure of C1C2. The results of the difference absorbance spectrum of C1C2 crystals (Fig. 3-3 d) suggested that the transition from the initial open state to a fully open state is hindered in the crystals. This result was caused by the effect of crystal packing and a similar result was observed in the TR-SFX experiment of bacteriorhodopsin[102]. As a result, it is suggested that capturing the fully open state structure of C1C2 by TR-SFX experiment is difficult. To capture the fully open state structure, it is required to obtain high-resolution structural changes of C1C2 in the solution.

Recently, many high-resolution protein structures have been reported by using cryo-EM single particle analysis[137,138]. In this strategy, unstable or large complex proteins in solution are used for structural analysis. The results of the difference absorbance spectrum of C1C2 in solution (Fig. 3-3 a) suggested that C1C2 in solution could transient from the dark state to the fully open state. Therefore the C1C2 full open structure would be captured by cryo-EM single particle analysis.

In addition, recent advances in cryo-electron microscopy (cryo-EM) have made it possible to solve not only large macromolecular complexes but also small proteins (~ 50 kDa)[139]. The author reported a middle-resolution cryo-EM structure of amino acid transporter complex[140]. In this paper, the protein complex is unstable and a consensus mutagenesis strategy was applied to improve the complex stability. Through the experiments of this paper, it is suggested that the small structural changes or unstabilized regions of protein could be detected by cryo-EM single particle analysis. In cryo-EM single particle analysis, a target protein is measured in solution. Therefore, the author could observe the structural changes without the effect of crystal packing. In addition to the development of hardware, the sample preparation technique has also developed and the nanodisc is one of the most used lipid bilayer environment-based tool[139]. It consists of a membrane lipid bilayer wrapped by membrane scaffold proteins, resulting in mimicking the physiological environment. In the future, it is maybe possible to capture the high-resolution protein structural changes in the physiological environment by combining these techniques.

4-3 Figures and table associated with Chapter 3

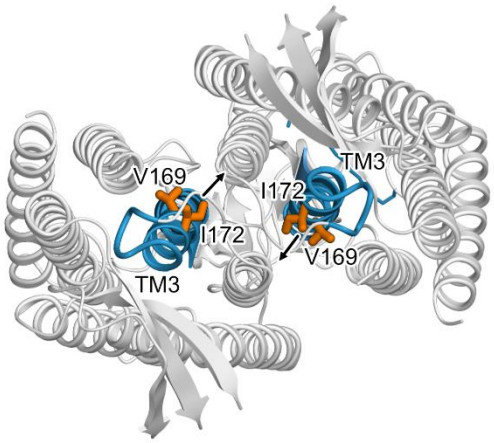

Fig. 4-1 Conformational change of TM3

Intracellular view of the C1C2 structure. The black allow indicates the conformatinal change of TM3. The residues in figure represents that they were used for mutant assay.

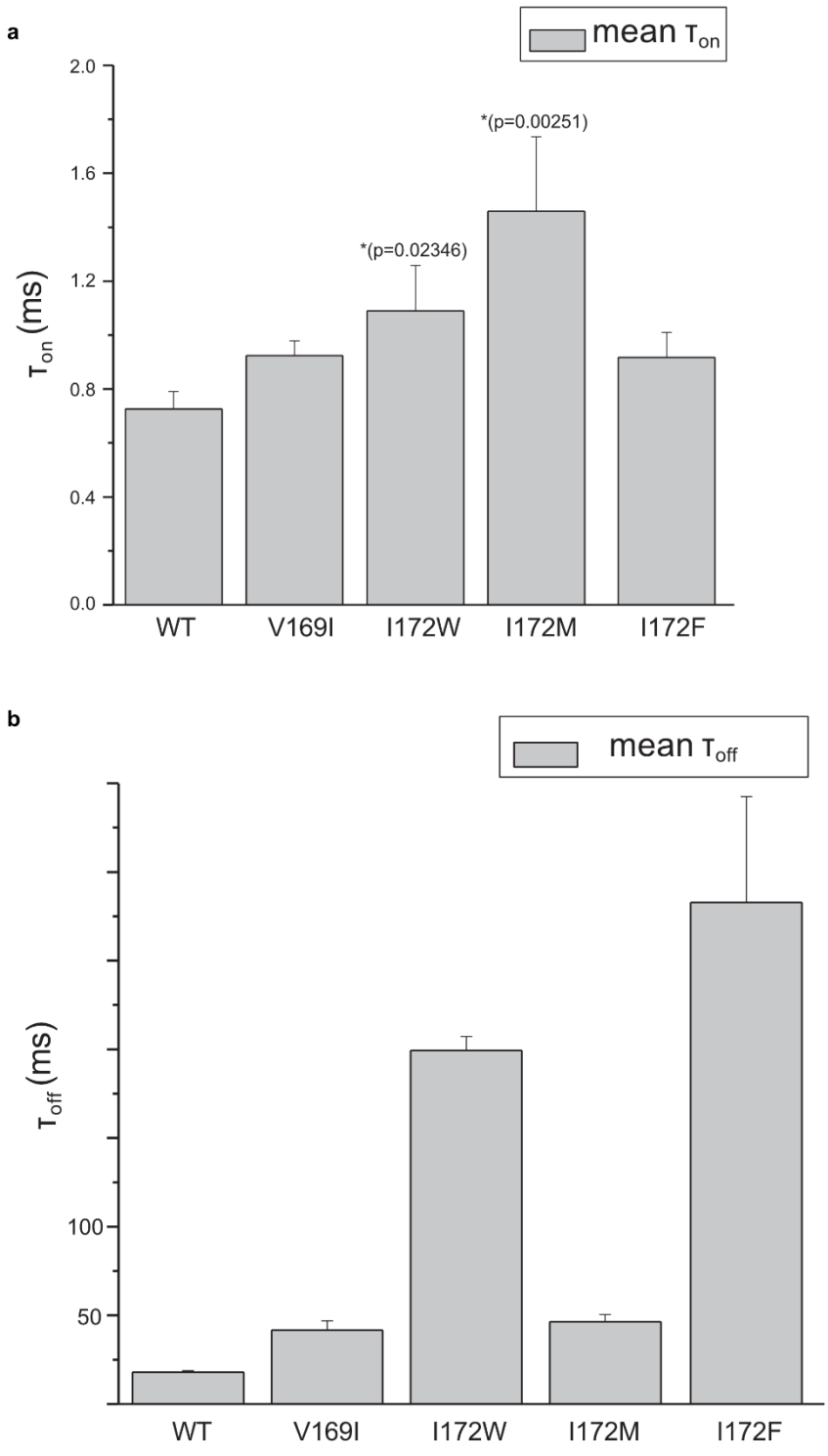

Fig. 4-2 Photocurrent kinetics of C1C2 wild-type and its mutants

a, Opening rates (T_{on}) and **b,** closing rate (T_{off}) of C1C2 wild-type and mutants. These experiments were performed by Andrès D Matsurana.

Original papers related to this thesis

1. Kazumasa Oda, Johannes Vierock, Satomi Oishi, Silvia Rodriguez-Rozada, Reiya Taniguchi, Keitaro Yamashita, J. Simon Wiegert, Tomohiro Nishizawa, Peter Hegemann and Osamu Nureki. Crystal structure of the red light-activated channelrhodopsin Chrimson. *Nature Communications* Journal Vol. 9, Pages 3949, 2018

2. Kazumasa Oda, Takashi Nomura, Takanori Nakane, Keiichi Inoue, Shota Ito, Johannes Vierock, Kunio Hirata, Keitaro Yamashita, Andrés D. Maturana, Kota Katayama, Tatsuya Ikuta, Itsuki Ishigami, Tamaki Izume, Rie Umeda, Ryuun Eguma, Satomi Oishi, Go Kasuya, Takafumi Kato, Tsukasa Kusakizako, Wataru Shihoya, Hiroto Shimada, Tomoyuki Takatsuji, Mizuki Takemoto, Reiya Taniguchi, Atsuhiro Tomita, Ryouki Nakamura, Masahiro Fukuda, Hirotake Miyauchi, Yongchan Lee, Eriko Nango, Rie Tanaka, Tomoyuki Tanaka, Michihiro Sugawara, Tetsunari Kimura, Tatsuro Shimamura, Takaaki Fujiwara, Yasuaki Yamanaka, Shigeki Owada, Yasumasa Joti, Kensuke Tono, Ryuichiro Ishitani, Shigehiko Hayashi, Hideki Kandori, Peter Hegemann, So Iwata, Minoru Kubo, Tomohiro Nishizawa and Osamu Nureki. Time-resolved serial femtosecond crystallography reveals early structural changes in channelrhodopsin. Submitted to *elife.*

Supplemental papers related to this thesis

1. Kazumasa Oda, Yongchan Lee, Pattama Wiriyasermkul, Yoko Tanaka, Mizuki Takemoto, Keitaro Yamashita, Shushi Nagamori, Tomohiro Nishizawa and Osamu. Consensus mutagenesis approach improves the thermal stability of system xc- transporter, xCT, and enables cryo-EM analyses. *Protein Science* Journal Vol. 29, Issue 12, Pages 2398-2407, 2020

2. Eriko Nango, Antoine Royant, Minoru Kubo, Takanori Nakane, Cecilia Wickstrand, Tetsunari Kimura, Tomoyuki Tanaka, Kensuke Tono, Changyong Song, Rie Tanaka, Toshi Arima, Ayumi Yamashita, Jun Kobayashi, Toshiaki Hosaka, Eiichi Mizohata, Przemyslaw Nogly, Michihiro Sugahara, Daewoong Nam, Takashi Nomura, Tatsuro Shimamura, Dohyun Im, Takaaki Fujiwara, Yasuaki Yamanaka, Byeonghyun Jeon, Tomohiro Nishizawa, Kazumasa Oda, Masahiro Fukuda, Rebecka Andersson, Petra

Båth, Robert Dods, Jan Davidsson, Shigeru Matsuoka, Satoshi Kawatake, Michio Murata, Osamu Nureki, Shigeki Owada, Takashi Kameshima, Takaki Hatsui, Yasumasa Joti, Gebhard Schertler, Makina Yabashi, Ana-Nicoleta Bondar, Jörg Standfuss, Richard Neutze and So Iwata. A three-dimensional movie of structural changes in bacteriorhodopsin. *Science* Journal Vol. 354, Issue 6319., Pages 1552-1557, 2016

Reference

1. Ernst, O. P. *et al.* Microbial and Animal Rhodopsins: Structures, Functions, and Molecular Mechanisms. *Chem. Rev.* **114**, 126–163 (2014).
2. Kurihara, M. & Sudo, Y. Microbial rhodopsins: wide distribution, rich diversity and great potential. *Biophys. Physicobiology* **12**, 121–129 (2015).
3. NAKANISHI, K. Why 11-cis-Retinal?1. *Am. Zool.* **31**, 479–489 (1991).
4. Bravaya, K., Bochenkova, A., Granovsky, A. & Nemukhin, A. An Opsin Shift in Rhodopsin: Retinal S0−S1 Excitation in Protein, in Solution, and in the Gas Phase. *J. Am. Chem. Soc.* **129**, 13035–13042 (2007).
5. Govorunova, E. G., Sineshchekov, O. A., Li, H. & Spudich, J. L. Microbial Rhodopsins: Diversity, Mechanisms, and Optogenetic Applications. *Annu. Rev. Biochem.* **86**, 845–872 (2017).
6. Kaneko, A., Inoue, K., Kojima, K., Kandori, H. & Sudo, Y. Conversion of microbial rhodopsins: insights into functionally essential elements and rational protein engineering. *Biophys. Rev.* **9**, 861–876 (2017).
7. Spudich, J. L., Yang, C.-S., Jung, K.-H. & Spudich, E. N. Retinylidene Proteins: Structures and Functions from Archaea to Humans. *Annu. Rev. Cell Dev. Biol.* **16**, 365–392 (2000).
8. Brown, L. S. Eubacterial rhodopsins — Unique photosensors and diverse ion pumps. *Biochim. Biophys. Acta BBA - Bioenerg.* **1837**, 553–561 (2014).
9. Kandori, H. Ion-pumping microbial rhodopsins. *Front. Mol. Biosci.* **2**, (2015).
10. Kitajima-Ihara, T. *et al.* Salinibacter Sensory Rhodopsin SENSORY RHODOPSIN I-LIKE PROTEIN FROM A EUBACTERIUM. *J. Biol. Chem.* **283**, 23533–23541 (2008).
11. Palczewski, K. G Protein–Coupled Receptor Rhodopsin. *Annu. Rev. Biochem.* **75**, 743–767 (2006).
12. Pushkarev, A. *et al.* A distinct abundant group of microbial rhodopsins discovered using functional metagenomics. *Nature* **558**, 595–599 (2018).
13. Shibukawa, A. *et al.* Photochemical Characterization of a New Heliorhodopsin from the Gram-Negative Eubacterium Bellilinea caldifistulae (BcHeR) and Comparison with Heliorhodopsin-48C12. *Biochemistry* **58**, 2934–2943 (2019).
14. Oesterhelt, D. & Stoeckenius, W. Rhodopsin-like Protein from the Purple Membrane of Halobacterium halobium. *Nature. New Biol.* **233**, 149–152 (1971).
15. Schobert, B. & Lanyi, J. K. Halorhodopsin is a light-driven chloride pump. *J. Biol. Chem.* **257**, 10306–10313 (1982).
16. Inoue, K. *et al.* A light-driven sodium ion pump in marine bacteria. *Nat. Commun.* **4**, 1678 (2013).
17. Nagel, G. *et al.* Channelrhodopsin-1: A Light-Gated Proton Channel in Green Algae. *Science* **296**, 2395–2398 (2002).
18. Sineshchekov, O. A., Jung, K.-H. & Spudich, J. L. Two rhodopsins mediate phototaxis to low- and

high-intensity light in Chlamydomonas reinhardtii. *Proc. Natl. Acad. Sci.* **99**, 8689–8694 (2002).

19. Govorunova, E. G., Sineshchekov, O. A., Janz, R., Liu, X. & Spudich, J. L. Natural light-gated anion channels: A family of microbial rhodopsins for advanced optogenetics. *Science* **349**, 647–650 (2015).
20. Henderson, R. & Unwin, P. N. T. Three-dimensional model of purple membrane obtained by electron microscopy. *Nature* **257**, 28–32 (1975).
21. Luecke, H., Schobert, B., Richter, H.-T., Cartailler, J.-P. & Lanyi, J. K. Structure of bacteriorhodopsin at 1.55 Å resolution 11Edited by D. C. Rees. *J. Mol. Biol.* **291**, 899–911 (1999).
22. Kolbe, M., Besir, H., Essen, L.-O. & Oesterhelt, D. Structure of the Light-Driven Chloride Pump Halorhodopsin at 1.8 Å Resolution. *Science* **288**, 1390–1396 (2000).
23. Royant, A. *et al.* X-ray structure of sensory rhodopsin II at 2.1-Å resolution. *Proc. Natl. Acad. Sci.* **98**, 10131–10136 (2001).
24. Morizumi, T. *et al.* X-ray Crystallographic Structure and Oligomerization of Gloeobacter Rhodopsin. *Sci. Rep.* **9**, 11283 (2019).
25. Vogeley, L. *et al.* Anabaena Sensory Rhodopsin: A Photochromic Color Sensor at 2.0 Å. *Science* **306**, 1390–1393 (2004).
26. Kato, H. E. *et al.* Structural basis for Na + transport mechanism by a light-driven Na + pump. *Nature* **521**, 48–53 (2015).
27. Kim, Y. S. *et al.* Crystal structure of the natural anion-conducting channelrhodopsin Gt ACR1. *Nature* **561**, 343–348 (2018).
28. Spudich, J. L. & Jung, K.-H. Microbial Rhodopsins: Phylogenetic and Functional Diversity. in *Handbook of Photosensory Receptors* 1–23 (John Wiley & Sons, Ltd, 2005). doi:10.1002/352760510X.ch1.
29. Marti, T., Rösselet, S. J., Otto, H., Heyn, M. P. & Khorana, H. G. The retinylidene Schiff base counterion in bacteriorhodopsin. *J. Biol. Chem.* **266**, 18674–18683 (1991).
30. Balashov, S. P. & Ebrey, T. G. Trapping and Spectroscopic Identification of the Photointermediates of Bacteriorhodopsin at Low Temperatures¶. *Photochem. Photobiol.* **73**, 453–462 (2001).
31. Luecke, H., Richter, H.-T. & Lanyi, J. K. Proton Transfer Pathways in Bacteriorhodopsin at 2.3 Angstrom Resolution. *Science* **280**, 1934–1937 (1998).
32. Trippens, J. *et al.* Phototropin Influence on Eyespot Development and Regulation of Phototactic Behavior in Chlamydomonas reinhardtii. *Plant Cell* **24**, 4687–4702 (2012).
33. Schneider, F., Grimm, C. & Hegemann, P. Biophysics of Channelrhodopsin. *Annu. Rev. Biophys.* **44**, 167–186 (2015).
34. Boyden, E. S., Zhang, F., Bamberg, E., Nagel, G. & Deisseroth, K. Millisecond-timescale, genetically targeted optical control of neural activity. *Nat. Neurosci.* **8**, 1263–1268 (2005).
35. Li, X. *et al.* Fast noninvasive activation and inhibition of neural and network activity by vertebrate rhodopsin and green algae channelrhodopsin. *Proc. Natl. Acad. Sci.* **102**, 17816–17821 (2005).

36. Zhang, F., Wang, L.-P., Boyden, E. S. & Deisseroth, K. Channelrhodopsin-2 and optical control of excitable cells. *Nat. Methods* **3**, 785–792 (2006).
37. Deisseroth, K. *et al.* Next-Generation Optical Technologies for Illuminating Genetically Targeted Brain Circuits. *J. Neurosci.* **26**, 10380–10386 (2006).
38. Deisseroth, K. Optogenetics. *Nat. Methods* **8**, 26–29 (2011).
39. Duan, X., Nagel, G. & Gao, S. Mutated Channelrhodopsins with Increased Sodium and Calcium Permeability. *Appl. Sci.* **9**, 664 (2019).
40. Nagel, G. *et al.* Light Activation of Channelrhodopsin-2 in Excitable Cells of Caenorhabditis elegans Triggers Rapid Behavioral Responses. *Curr. Biol.* **15**, 2279–2284 (2005).
41. Monesson-Olson, B. D., Browning-Kamins, J., Aziz-Bose, R., Kreines, F. & Trapani, J. G. Optical Stimulation of Zebrafish Hair Cells Expressing Channelrhodopsin-2. *PLOS ONE* **9**, e96641 (2014).
42. Aravanis, A. M. *et al.* An optical neural interface:in vivocontrol of rodent motor cortex with integrated fiberoptic and optogenetic technology. *J. Neural Eng.* **4**, S143–S156 (2007).
43. Adamantidis, A. R., Zhang, F., Aravanis, A. M., Deisseroth, K. & de Lecea, L. Neural substrates of awakening probed with optogenetic control of hypocretin neurons. *Nature* **450**, 420–424 (2007).
44. Ritter, E., Stehfest, K., Berndt, A., Hegemann, P. & Bartl, F. J. Monitoring Light-induced Structural Changes of Channelrhodopsin-2 by UV-visible and Fourier Transform Infrared Spectroscopy. *J. Biol. Chem.* **283**, 35033–35041 (2008).
45. Bamann, C., Kirsch, T., Nagel, G. & Bamberg, E. Spectral Characteristics of the Photocycle of Channelrhodopsin-2 and Its Implication for Channel Function. *J. Mol. Biol.* **375**, 686–694 (2008).
46. Lórenz-Fonfría, V. A. *et al.* Temporal evolution of helix hydration in a light-gated ion channel correlates with ion conductance. *Proc. Natl. Acad. Sci.* **112**, E5796–E5804 (2015).
47. Kuhne, J. *et al.* Unifying photocycle model for light adaptation and temporal evolution of cation conductance in channelrhodopsin-2. *Proc. Natl. Acad. Sci.* **116**, 9380–9389 (2019).
48. Backmark, A. E. *et al.* Fluorescent probe for high-throughput screening of membrane protein expression. *Protein Sci. Publ. Protein Soc.* **22**, 1124–1132 (2013).
49. Hattori, M., Hibbs, R. E. & Gouaux, E. A Fluorescence-Detection Size-Exclusion Chromatography-Based Thermostability Assay for Membrane Protein Precrystallization Screening. *Structure* **20**, 1293–1299 (2012).
50. Pardon, E. *et al.* A general protocol for the generation of Nanobodies for structural biology. *Nat. Protoc.* **9**, 674–693 (2014).
51. Kato, H. E. *et al.* Crystal structure of the channelrhodopsin light-gated cation channel. *Nature* **482**, 369–374 (2012).
52. Volkov, O. *et al.* Structural insights into ion conduction by channelrhodopsin 2. *Science* **358**, (2017).
53. Yizhar, O., Fenno, L. E., Davidson, T. J., Mogri, M. & Deisseroth, K. Optogenetics in Neural Systems. *Neuron* **71**, 9–34 (2011).

54. Kloppmann, E., Becker, T. & Ullmann, G. M. Electrostatic potential at the retinal of three archaeal rhodopsins: implications for their different absorption spectra. *Proteins* **61**, 953–965 (2005).
55. Rajamani, R., Lin, Y.-L. & Gao, J. The opsin shift and mechanism of spectral tuning in rhodopsin. *J. Comput. Chem.* **32**, 854–865 (2011).
56. Schenkl, S., Mourik, F. van, Zwan, G. van der, Haacke, S. & Chergui, M. Probing the Ultrafast Charge Translocation of Photoexcited Retinal in Bacteriorhodopsin. *Science* **309**, 917–920 (2005).
57. Kato, H. E. *et al.* Atomistic design of microbial opsin-based blue-shifted optogenetics tools. *Nat. Commun.* **6**, 7177 (2015).
58. Kianianmomeni, A., Stehfest, K., Nematollahi, G., Hegemann, P. & Hallmann, A. Channelrhodopsins of Volvox carteri Are Photochromic Proteins That Are Specifically Expressed in Somatic Cells under Control of Light, Temperature, and the Sex Inducer. *Plant Physiol.* **151**, 347–366 (2009).
59. Klapoetke, N. C. *et al.* Independent optical excitation of distinct neural populations. *Nat. Methods* **11**, 338–346 (2014).
60. Lin, J. Y., Knutsen, P. M., Muller, A., Kleinfeld, D. & Tsien, R. Y. ReaChR: a red-shifted variant of channelrhodopsin enables deep transcranial optogenetic excitation. *Nat. Neurosci.* **16**, 1499–1508 (2013).
61. Zhang, F. *et al.* Red-shifted optogenetic excitation: a tool for fast neural control derived from Volvox carteri. *Nat. Neurosci.* **11**, 631–633 (2008).
62. Prigge, M. *et al.* Color-tuned Channelrhodopsins for Multiwavelength Optogenetics. *J. Biol. Chem.* **287**, 31804–31812 (2012).
63. Yizhar, O. *et al.* Neocortical excitation/inhibition balance in information processing and social dysfunction. *Nature* **477**, 171–178 (2011).
64. Yamashita, K., Hirata, K. & Yamamoto, M. KAMO: towards automated data processing for microcrystals. *Acta Crystallogr. Sect. Struct. Biol.* **74**, 441–449 (2018).
65. Kabsch, W. XDS. *Acta Crystallogr. D Biol. Crystallogr.* **66**, 125–132 (2010).
66. Adams, P. D. *et al.* PHENIX: a comprehensive Python-based system for macromolecular structure solution. *Acta Crystallogr. D Biol. Crystallogr.* **66**, 213–221 (2010).
67. Emsley, P., Lohkamp, B., Scott, W. G. & Cowtan, K. Features and development of Coot. *Acta Crystallogr. D Biol. Crystallogr.* **66**, 486–501 (2010).
68. Vagin, A. A. *et al.* REFMAC5 dictionary: organization of prior chemical knowledge and guidelines for its use. *Acta Crystallogr. D Biol. Crystallogr.* **60**, 2184–2195 (2004).
69. Ho, B. K. & Gruswitz, F. HOLLOW: Generating Accurate Representations of Channel and Interior Surfaces in Molecular Structures. *BMC Struct. Biol.* **8**, 49 (2008).
70. Vierock, J., Grimm, C., Nitzan, N. & Hegemann, P. Molecular determinants of proton selectivity and gating in the red-light activated channelrhodopsin Chrimson. *Sci. Rep.* **7**, 9928 (2017).
71. Whole-cell Patch-clamp Recordings for Electrophysiological Determination of Ion Selectivity in

Channelrhodopsins | Protocol. https://www.jove.com/t/55497/whole-cell-patch-clamp-recordings-for-electrophysiological.

72. Gee, C. E., Ohmert, I., Wiegert, J. S. & Oertner, T. G. Preparation of Slice Cultures from Rodent Hippocampus. *Cold Spring Harb. Protoc.* **2017**, pdb.prot094888 (2017).
73. Wiegert, J. S., Gee, C. E. & Oertner, T. G. Single-Cell Electroporation of Neurons. *Cold Spring Harb. Protoc.* **2017**, pdb.prot094904 (2017).
74. Müller, M., Bamann, C., Bamberg, E. & Kühlbrandt, W. Light-Induced Helix Movements in Channelrhodopsin-2. *J. Mol. Biol.* **427**, 341–349 (2015).
75. Volkov, O. *et al.* Structural insights into ion conduction by channelrhodopsin 2. *Science* **358**, (2017).
76. Sugiyama, Y. *et al.* Photocurrent attenuation by a single polar-to-nonpolar point mutation of channelrhodopsin-2. *Photochem. Photobiol. Sci.* **8**, 328–336 (2009).
77. Hou, S.-Y. *et al.* Diversity of Chlamydomonas channelrhodopsins. *Photochem. Photobiol.* **88**, 119–128 (2012).
78. Urmann, D. *et al.* Photochemical Properties of the Red-shifted Channelrhodopsin Chrimson. *Photochem. Photobiol.* **93**, 782–795 (2017).
79. Li, H., Govorunova, E. G., Sineshchekov, O. A. & Spudich, J. L. Role of a Helix B Lysine Residue in the Photoactive Site in Channelrhodopsins. *Biophys. J.* **106**, 1607–1617 (2014).
80. Gerwert, K., Freier, E. & Wolf, S. The role of protein-bound water molecules in microbial rhodopsins. *Biochim. Biophys. Acta BBA - Bioenerg.* **1837**, 606–613 (2014).
81. Plazzo, A. P. *et al.* Bioinformatic and Mutational Analysis of Channelrhodopsin-2 Protein Cation-conducting Pathway. *J. Biol. Chem.* **287**, 4818–4825 (2012).
82. Greenhalgh, D. A., Farrens, D. L., Subramaniam, S. & Khorana, H. G. Hydrophobic amino acids in the retinal-binding pocket of bacteriorhodopsin. *J. Biol. Chem.* **268**, 20305–20311 (1993).
83. Ihara, K., Amemiya, T., Miyashita, Y. & Mukohata, Y. Met-145 is a key residue in the dark adaptation of bacteriorhodopsin homologs. *Biophys. J.* **67**, 1187–1191 (1994).
84. Berndt, A., Yizhar, O., Gunaydin, L. A., Hegemann, P. & Deisseroth, K. Bi-stable neural state switches. *Nat. Neurosci.* **12**, 229–234 (2009).
85. Bamann, C., Gueta, R., Kleinlogel, S., Nagel, G. & Bamberg, E. Structural Guidance of the Photocycle of Channelrhodopsin-2 by an Interhelical Hydrogen Bond. *Biochemistry* **49**, 267–278 (2010).
86. Hososhima, S., Sakai, S., Ishizuka, T. & Yawo, H. Kinetic Evaluation of Photosensitivity in Bi-Stable Variants of Chimeric Channelrhodopsins. *PLOS ONE* **10**, e0119558 (2015).
87. Lórenz-Fonfría, V. A. & Heberle, J. Channelrhodopsin unchained: Structure and mechanism of a light-gated cation channel. *Biochim. Biophys. Acta BBA - Bioenerg.* **1837**, 626–642 (2014).
88. Joh, N. H. *et al.* Modest stabilization by most hydrogen-bonded side-chain interactions in membrane proteins. *Nature* **453**, 1266–1270 (2008).
89. Mager, T. *et al.* High frequency neural spiking and auditory signaling by ultrafast red-shifted

optogenetics. *Nat. Commun.* **9**, 1750 (2018).

90. Ruiz-González, M. X. & Marín, I. New Insights into the Evolutionary History of Type 1 Rhodopsins. *J. Mol. Evol.* **58**, 348–358 (2004).
91. Lin, J. Y., Lin, M. Z., Steinbach, P. & Tsien, R. Y. Characterization of Engineered Channelrhodopsin Variants with Improved Properties and Kinetics. *Biophys. J.* **96**, 1803–1814 (2009).
92. Gunaydin, L. A. *et al.* Ultrafast optogenetic control. *Nat. Neurosci.* **13**, 387–392 (2010).
93. Berndt, A. *et al.* High-efficiency channelrhodopsins for fast neuronal stimulation at low light levels. *Proc. Natl. Acad. Sci.* **108**, 7595–7600 (2011).
94. Wanko, M., Hoffmann, M., Frähmcke, J., Frauenheim, T. & Elstner, M. Effect of Polarization on the Opsin Shift in Rhodopsins. 2. Empirical Polarization Models for Proteins. *J. Phys. Chem. B* **112**, 11468–11478 (2008).
95. Nack, M. *et al.* The DC gate in Channelrhodopsin-2: crucial hydrogen bonding interaction between C128 and D156. *Photochem. Photobiol. Sci.* **9**, 194–198 (2010).
96. Lórenz-Fonfría, V. A. *et al.* Transient protonation changes in channelrhodopsin-2 and their relevance to channel gating. *Proc. Natl. Acad. Sci.* **110**, E1273–E1281 (2013).
97. Ito, S. *et al.* Water-Containing Hydrogen-Bonding Network in the Active Center of Channelrhodopsin. *J. Am. Chem. Soc.* **136**, 3475–3482 (2014).
98. Kuhne, J. *et al.* Unifying photocycle model for light adaptation and temporal evolution of cation conductance in channelrhodopsin-2. *Proc. Natl. Acad. Sci.* **116**, 9380–9389 (2019).
99. Müller, M., Bamann, C., Bamberg, E. & Kühlbrandt, W. Projection Structure of Channelrhodopsin-2 at 6 Å Resolution by Electron Crystallography. *J. Mol. Biol.* **414**, 86–95 (2011).
100. Müller, M., Bamann, C., Bamberg, E. & Kühlbrandt, W. Light-Induced Helix Movements in Channelrhodopsin-2. *J. Mol. Biol.* **427**, 341–349 (2015).
101. Tosha, T. *et al.* Capturing an initial intermediate during the P450nor enzymatic reaction using time-resolved XFEL crystallography and caged-substrate. *Nat. Commun.* **8**, 1585 (2017).
102. Nango, E. *et al.* A three-dimensional movie of structural changes in bacteriorhodopsin. *Science* **354**, 1552–1557 (2016).
103. Suga, M. *et al.* Light-induced structural changes and the site of O=O bond formation in PSII caught by XFEL. *Nature* **543**, 131–135 (2017).
104. Shimada, A. *et al.* A nanosecond time-resolved XFEL analysis of structural changes associated with CO release from cytochrome c oxidase. *Sci. Adv.* **3**, e1603042 (2017).
105. Pandey, S. *et al.* Time-resolved serial femtosecond crystallography at the European XFEL. *Nat. Methods* **17**, 73–78 (2020).
106. Kubo, M. *et al.* Nanosecond pump–probe device for time-resolved serial femtosecond crystallography developed at SACLA. *J. Synchrotron Radiat.* **24**, 1086–1091 (2017).
107. Inaguma, A. *et al.* Chimeras of Channelrhodopsin-1 and -2 from Chlamydomonas reinhardtii Exhibit

Distinctive Light-induced Structural Changes from Channelrhodopsin-2. *J. Biol. Chem.* **290**, 11623–11634 (2015).

108. Hontani, Y. *et al.* Reaction dynamics of the chimeric channelrhodopsin C1C2. *Sci. Rep.* **7**, 7217 (2017).
109. Inoue, K. *et al.* A light-driven sodium ion pump in marine bacteria. *Nat. Commun.* **4**, 1678 (2013).
110. Inoue, K. *et al.* A natural light-driven inward proton pump. *Nat. Commun.* **7**, 13415 (2016).
111. Shrager, R. I. & W. Hendler, R. Some pitfalls in curve-fitting and how to avoid them: A case in point. *J. Biochem. Biophys. Methods* **36**, 157–173 (1998).
112. Kameshima, T. *et al.* Development of an X-ray pixel detector with multi-port charge-coupled device for X-ray free-electron laser experiments. *Rev. Sci. Instrum.* **85**, 033110 (2014).
113. Nakane, T. *et al.* Data processing pipeline for serial femtosecond crystallography at SACLA. *J. Appl. Crystallogr.* **49**, 1035–1041 (2016).
114. Barty, A. *et al.* Cheetah: software for high-throughput reduction and analysis of serial femtosecond X-ray diffraction data. *J. Appl. Crystallogr.* **47**, 1118–1131 (2014).
115. White, T. A. *et al.* CrystFEL: a software suite for snapshot serial crystallography. *J. Appl. Crystallogr.* **45**, 335–341 (2012).
116. Zaefferer, S. New developments of computer-aided crystallographic analysis in transmission electron microscopy. *J. Appl. Crystallogr.* **33**, 10–25 (2000).
117. Duisenberg, A. J. M. Indexing in single-crystal diffractometry with an obstinate list of reflections. *J. Appl. Crystallogr.* **25**, 92–96 (1992).
118. Ten Eyck, L. F. Crystallographic fast Fourier transforms. *Acta Crystallogr. A* **29**, 183–191 (1973).
119. Winn, M. D. *et al.* Overview of the CCP4 suite and current developments. *Acta Crystallogr. D Biol. Crystallogr.* **67**, 235–242 (2011).
120. Nogly, P. *et al.* Retinal isomerization in bacteriorhodopsin captured by a femtosecond x-ray laser. *Science* **361**, (2018).
121. Ritter, E., Stehfest, K., Berndt, A., Hegemann, P. & Bartl, F. J. Monitoring Light-induced Structural Changes of Channelrhodopsin-2 by UV-visible and Fourier Transform Infrared Spectroscopy. *J. Biol. Chem.* **283**, 35033–35041 (2008).
122. Kuhne, J. *et al.* Early Formation of the Ion-Conducting Pore in Channelrhodopsin-2. *Angew. Chem. Int. Ed.* **54**, 4953–4957 (2015).
123. Neumann-Verhoefen, M.-K. *et al.* Ultrafast Infrared Spectroscopy on Channelrhodopsin-2 Reveals Efficient Energy Transfer from the Retinal Chromophore to the Protein. *J. Am. Chem. Soc.* **135**, 6968–6976 (2013).
124. Bühl, E. *et al.* Ultrafast Protein Response in Channelrhodopsin-2 Studied by Time-Resolved Infrared Spectroscopy. *J. Phys. Chem. Lett.* **9**, 7180–7184 (2018).
125. Neutze, R. *et al.* Bacteriorhodopsin: a high-resolution structural view of vectorial proton transport. *Biochim. Biophys. Acta BBA - Biomembr.* **1565**, 144–167 (2002).

126. Cheng, C. *et al.* An Atomistic Model of a Precursor State of Light-Induced Channel Opening of Channelrhodopsin. *Biophys. J.* **115**, 1281–1291 (2018).
127. Lórenz-Fonfría, V. A. *et al.* Temporal evolution of helix hydration in a light-gated ion channel correlates with ion conductance. *Proc. Natl. Acad. Sci.* **112**, E5796–E5804 (2015).
128. Krause, B. S. *et al.* Tracking Pore Hydration in Channelrhodopsin by Site-Directed Infrared-Active Azido Probes. *Biochemistry* **58**, 1275–1286 (2019).
129. Watanabe, H. C. *et al.* Structural Model of Channelrhodopsin. *J. Biol. Chem.* **287**, 7456–7466 (2012).
130. Oda, K. *et al.* Crystal structure of the red light-activated channelrhodopsin Chrimson. *Nat. Commun.* **9**, 3949 (2018).
131. Tsunoda S. Ion Transport Mechanism of the Microbial Rhodopsins Revealed by Electrophysiological Studies. *Seibutsu Butsuri* **57**, 179–185 (2017).
132. Cheng, C. *et al.* An Atomistic Model of a Precursor State of Light-Induced Channel Opening of Channelrhodopsin. *Biophys. J.* **115**, 1281–1291 (2018).
133. Karasuyama, M., Inoue, K., Nakamura, R., Kandori, H. & Takeuchi, I. Understanding Colour Tuning Rules and Predicting Absorption Wavelengths of Microbial Rhodopsins by Data-Driven Machine-Learning Approach. *Sci. Rep.* **8**, 15580 (2018).
134. Inoue, K. *et al.* Red-shifting mutation of light-driven sodium-pump rhodopsin. *Nat. Commun.* **10**, 1993 (2019).
135. AzimiHashemi, N. *et al.* Synthetic retinal analogues modify the spectral and kinetic characteristics of microbial rhodopsin optogenetic tools. *Nat. Commun.* **5**, 5810 (2014).
136. Ganapathy, S. *et al.* Redshifted and Near-infrared Active Analog Pigments Based upon Archaerhodopsin-3. *Photochem. Photobiol.* **95**, 959–968 (2019).
137. Kasuya, G. *et al.* Cryo-EM structures of the human volume-regulated anion channel LRRC8. *Nat. Struct. Mol. Biol.* **25**, 797–804 (2018).
138. Lee, Y. *et al.* Cryo-EM structure of the human L-type amino acid transporter 1 in complex with glycoprotein CD98hc. *Nat. Struct. Mol. Biol.* **26**, 510–517 (2019).
139. Sgro, G. G. & Costa, T. R. D. Cryo-EM Grid Preparation of Membrane Protein Samples for Single Particle Analysis. *Front. Mol. Biosci.* **5**, (2018).
140. Oda, K. *et al.* Consensus mutagenesis approach improves the thermal stability of system xc− transporter, xCT, and enables cryo-EM analyses. *Protein Sci.* **29**, 2398–2407 (2020).

Data availability

Data supporting the findings of this manuscript are available from the corresponding authors upon reasonable request. Coordinates and structure factors are deposited in the Protein Data Bank with accession codes PDB 5ZIH. Raw diffraction images are also deposited to Zenodo data repository (https://doi.org/10.5281/zenodo.1319974).

Coordinate and structure factor for the dark TR-SFX structure have been deposited in the PDB with the accession code 7C86. Raw diffraction images have been deposited in the Coherent X-ray Imaging Data Bank (accession ID 150).

Acknowledgment

The author thanks Professor Osamu Nureki for the supervision during the bachelor’s, master's and Ph.D. courses. The author appreciates specially-appointed Professor Ryuichiro Ishitani, associated Professor Tomohiro Nishizawa for supporting my study. The author also thanks to all Nureki lab’s members, especially my supervisor Satomi Oishi, my colleague Tatsuya Ikuta and Tamaki Izume.

Finally, I would like to appreciate my family for continuous support.